Some studies of multi-wire proportional chambers

G. C. Smith

SOME STUDIES OF

MULTI-WIRE PROPORTIONAL CHAMBERS

by

G. C. SMITH, B.Sc.

A thesis submitted to the University of Durham

for the Degree of Doctor of Philosophy.

Being an account of work carried out in the University

of Durham during the period October 1970 to September 1973.

March 1974

ABSTRACT

A study has been made of the displacement of sense wires in large multiwire proportional chambers, and methods are investigated to counteract this. A sense wire support which creates the minimum of dead-space while keeping the wires absolutely stationary is found to be a thin melinex strip stretched tightly across the wires.

A brief review of some of the characteristics of transition radiation is then made; the application of the multiwire proportional chamber to detection of this radiation is described in the context of a pulse shape discrimination process developed for this purpose. Experiments with an X-ray and beta-particle source show that the technique should be capable of discriminating between an X-ray and a charged particle from an X-ray pulse superimposed upon a particle pulse.

The discrimination process is used with 1.5 GeV electrons and pions traversing a 250 layer melinex stack and a block of plastic foam, the detector being an argon/methane filled proportional chamber. A maximum electron detection efficiency of 12.8% is achieved, together with a maximum rejection ratio for non-radiating pions of 2.8.

A further experiment with horizontal cosmic ray muons traversing a polyurethane foam radiator, and using a large 60cm x 30cm active area proportional chamber, yields a transition radiation photon flux of 0.023 per particle which is in good agreement with that calculated from the known horizontal muon spectrum and transition radiation theory.

CONTENTS

CHAPTER 1

INTRODUCTION

1.1 Particle Detectors

The particle detector, whether solid-state, liquid or gaseous, constitutes the basic tool of cosmic ray and elementary particle research. Any particular detector can normally be categorised as either a 'counter' type, such as the proportional counter, Geiger-Müller counter and scintillator, or 'track delineating' type, such as the spark chamber and streamer chamber. Operation of the latter type depends upon the initial detection of the particle by a counter detector, usually the scintillator.

A relatively new type of detector, the multi-wire proportional counter (MWPC), which is a development of the proportional counter, possesses the basic properties of both of the above detector categories. Indeed, a few years ago the combination of the scintillator and spark chamber formed one of the commonest particle and track locating devices but the MWPC is now being used in many instances where hitherto this combination would have been chosen. The present work involves both a study of the new detector itself and its application to an important problem in high energy particle physics.

A brief account of the proportional counter would perhaps be the best way of introducing the multi-wire chamber. It consists of two electrodes, a fine central wire as anode which is enclosed by a hollow cylindrical cathode. Particles traversing the counter leave a path of ion pairs in the enclosed gas and the voltage applied between the two electrodes is high enough so that the electric field close to the anode enables the electrons to make

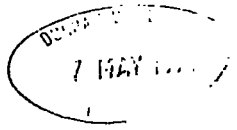

ionizing collisions with the gas molecules within a few wire diameters of the anode wire. The electron avalanche does not reach saturation however and the pulse height is proportional to the ionization deposited. If the amplification factor (the number of electrons produced from one initial electron) is known the ionization can be determined.

1.2 Evolution of the multi-wire proportional chamber

The cylindrical cathode of the proportional counter was altered to become two flat planes about a couple of centimetres apart, in between which were not one but a set of fine anode wires, equally spaced and equidistant from each cathode plane. Quite logically this became known as the multiwire proportional chamber (MWPC) and was first conceived and designed by Charpak (1), though a form of multiwire counter had been constructed and operated successfully in the 1940's by a group at the Los Alamos Laboratories (2). That this was never followed up at the time is very surprising but according to Charpak (3) there is one main reason why it was generally thought multi-wire chambers would not be successful and hence why their major development only took place so recently. While there was clearly no problem in detecting an avalanche around the one wire in a proportional counter it was thought that when several wires were brought close together the capacitive coupling between them would prevent localisation of the avalanche on one single wire because an induced pulse would be created on adjacent wires. In fact, tests made with a pulse generator show that when a fast pulse is applied to a wire, adjacent ones pick up a pulse of the same polarity as the applied pulse, though naturally attenuated. Attempts were made to overcome this drawback by

interposing shielding wires between the sense wires (4) but this, apart from making construction of the chamber more difficult, reduced the spatial resolution.

However it was later discovered that when a negative pulse is created on a wire by an electron avalanche there is an induced positive pulse on both adjacent wires due to movement of electrons away from, and positive ions toward, them, the magnitude of which is greater than the capacitively coupled negative pulse. Therefore the net result is a small positive pulse on both adjacent wires, and by using amplifiers which are only sensitive to negative pulses the wires in the multi-wire chamber act as independent proportional counters.

Other favourable properties which helped it achieve its present popularity are:

i) A high detection efficiency with high counting rate capability ($\backsimeq 10^5$ Hz per wire). In addition it has a resolving time of about 30 nsec which, comparing this with the spark chamber memory time of at least a microsecond, means it can be employed in much higher background conditions.

ii) A good spatial resolution (usually about half the sense wire spacing.)

iii) A very low mass per unit area ($\backsimeq$ 20 mg/cm^2).

iv) Energy linearity, or a linear $^{dE}/_{dx}$ response, which allows particle identification in certain cases.

v) It can easily be made with either small or large sensitive areas ($\backsimeq$ cm^2 to m^2) of reasonably arbitrary shapes which allows a wide range of experiments to be performed.

Of these properties the spark chamber possesses (ii), (iii) and (v) but not (i) and (iv) and the scintillator possesses

(i), (iv) and (v) but not (ii) and (iii). Therefore it is not surprising that the MWPC is used in many experiments in favour of the combination of spark chamber and scintillator.

1.3. Some basic properties of the MWPC

A cross-section of the geometry of a MWPC is shown in figure 1.1. The two cathode planes are constructed from wires with a diameter of about 125 μm and spacing 1 mm. The diameter of the sense wires is much smaller to achieve the high fields necessary for electron avalanching and is usually 25 μm; generally the sense wires are wound orthogonal to the H.T. wires. In certain cases the cathode planes are made from aluminium foil.

Conventionally the sense wire spacing is designated as 's', and is usually 2 mm. The cathode plane - sense wire plane spacing, L, generally takes on values between 0.5 and 1 cm.

Unlike proportional counters, which have an earthed cathode and positive potential applied to the anode wire, proportional chambers generally have a negative potential applied to the cathode plane (which therefore becomes known as the H.T. plane) with the sense wires earthed via a small resistance. A particle passing through the chamber ionizes the gas along its path and electron multiplication takes place around the nearest sense wire, the subsequent pulse being monitored across the resistance.

1.3.1 Field variation in the chamber

It has been shown by Erskine (5) that the potential in the active volume of a proportional chamber with an applied H.T. of V_o is given by:

$$V = q\left[\frac{2\pi L}{s} - \ln\left(4\sin^2\frac{\pi x}{s} + 4\sinh^2\frac{\pi y}{s}\right)\right] \qquad 1.1$$

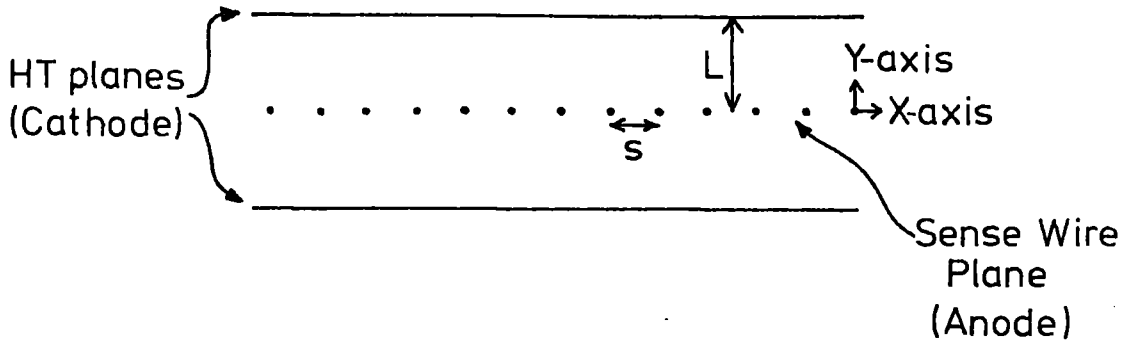

FIGURE 1.1 CROSS-SECTION OF A MULTIWIRE PROPORTIONAL CHAMBER

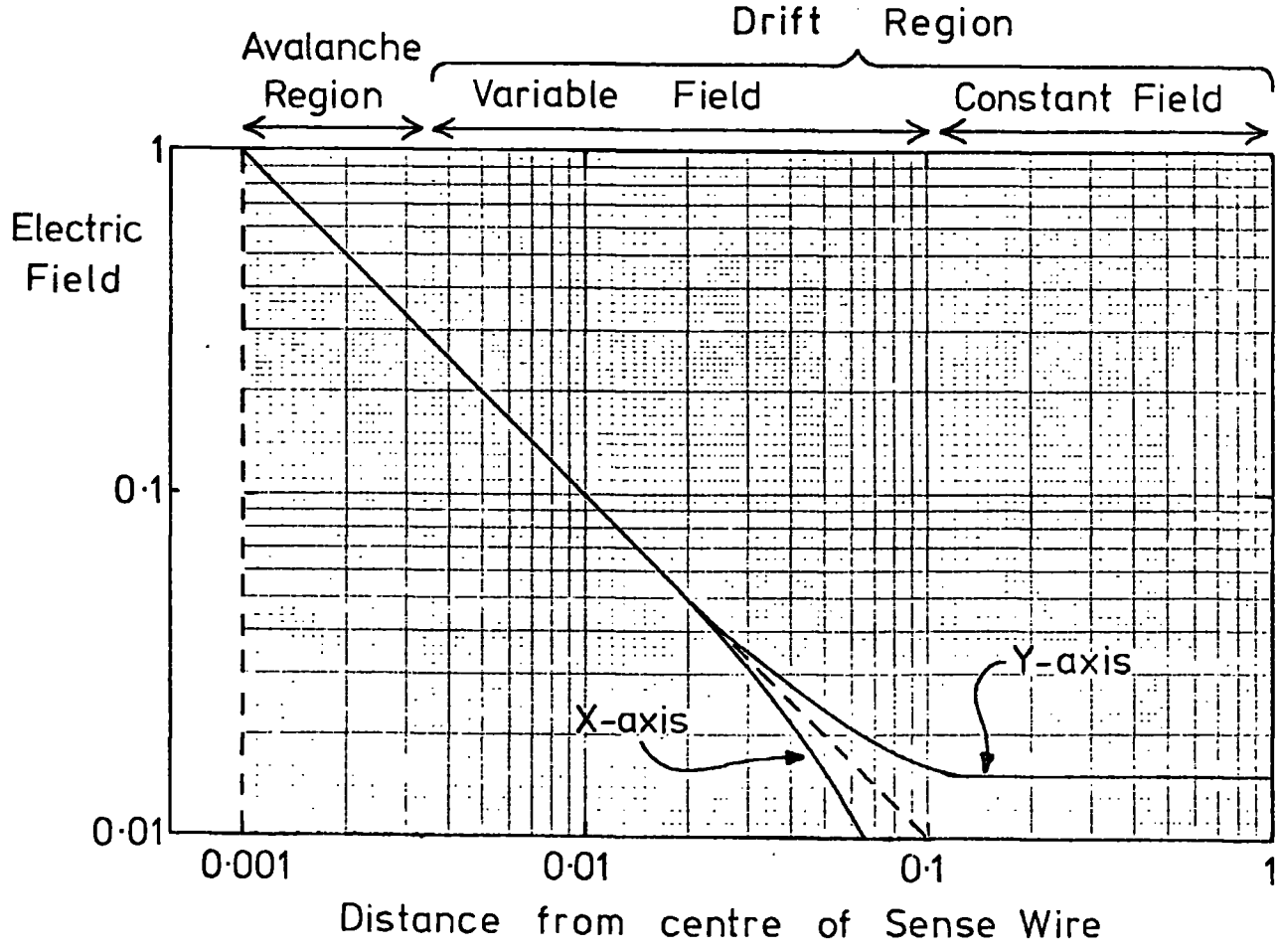

FIGURE 1.2 VARIATION OF ELECTRIC FIELD STRENGTH ALONG 'X' AND 'Y' AXES OF A PROPORTIONAL CHAMBER

where $q = V_o\left[\frac{2\pi L}{s} - 2\ln\left(\frac{\pi d}{s}\right)\right]^{-1}$ is

the charge per unit length on a sense wire, and x, y are distances along the axis in the sense wire plane (but perpendicular to the wire direction) and the axis perpendicular to the sense wire plane respectively.

Differentiation of equation 1.1 with respect to 'x' and 'y' gives the electric field along the corresponding axes, e.g. with an applied potential of 4 kV, a wire spacing of s = 2 mm and L = 1 cm, and sense wire diameter of 25 μm the field at the wire is $2.1 \cdot 10^5$ V/cm. Figure 1.2 illustrates the field variation along the 'x' and 'y' axes, normalised to a field at the wire surface of 1. Whereas in the proportional counter the lines of equipotential are never linearly spaced but gradually get closer together, on moving from the cathode to anode there is a large region in the proportional chamber (for narrow anode wire spacing) which has a linear field and only very near the wire do the equipotentials begin to get closer together, where a very large field increase takes place; electron avalanching only begins a few wire diameters from the wire itself.

The electric field in the linear region is given by $^{2q\pi}/_{s}$; if s = 2 mm, L = 6 mm, d = 25 μm, and V_o = 3.4 kV, then E = 7 kV/cm. This corresponds to an electron drift velocity of about 4 cm/ μsec in a typical chamber gas of argon with a small quantity of methane or carbon dioxide.

The very high field which occurs at sense wire surfaces makes it necessary to increase the diameter of the outer wire or couple of wires in a chamber to avoid breakdown around these particular wires in normal operation. The increased diameter reduces the

field because, close to the wire, this field is proportional to $^1/_d$, where d is the distance to the centre of the wire.

1.3.2 Wire Spacing, Wire Diameter, and Amplification

The gain, or amplification factor, A, of a chamber is the number of electrons created by the avalanching of one primary electron.

Since the electric field depends upon $^1/_d$ it is possible to produce an increased field at the surface of the wire for the same applied voltage by using sense wires of a smaller diameter, so it is possible to obtain a gain equal to that from a larger diameter wire by using a smaller H.T. Therefore it is best to use wire of the smallest diameter possible, but ensuring that it is not so small that there is a danger of wire breakage.

Electric field (and hence gas gain) is also dependent upon wire spacing; Table 1.1 shows the capacitance of sense wires with respect to the H.T. plane for L = 7 mm and various wire diameters and spacings (6).

TABLE 1.1 CAPACITANCE OF SENSE WIRES TO H.T. PLANE

L (mm)	Wire Diameter (μm)	Capacitance(pF/metre)		
		s = 3 mm	s = 2 mm	s = 1 mm
7	20	4.97	3.85	2.25
7	50	5.41	4.11	2.34
3	20	7.94	6.81	4.56

As the wire spacing is decreased the capacitance also decreases. Since Q = CV then to keep the same charge on the wires (i.e. the same amplification) the H.T. has to be increased, e.g. for 20 μm wires it should be increased in the ratio 1 : 1.3 : 2.2 for the above wire spacings. Obviously one will eventually run into breakdown problems as the spacing is reduced further and this is the limitation on the best spatial resolution which can be obtained from MWPC's (spatial resolution clearly being dependent upon wire spacing). For this reason s = 2 mm is commonly used as a compromise between good resolution and comparative safety against breakdown. However, working chambers with spacing down to 0.5 mm have been built (7).

Also shown in Table 1.1 are the corresponding capacitance values for 20 μm diameter wires with L = 3 mm. The same increase in voltage ratio this time is 1 : 1.17 : 1.74, i.e. it is possible to operate at lower over-all voltages but with the same gain. However there are two main drawbacks to reducing L.

i) The ionization deposited in the chamber is reduced, which could in certain cases mean a higher gain to obtain the required pulse height, and this would ruin the advantage of using a reduced H.T. since it would then have to be increased.

ii) Mechanical tolerances have to become smaller as L is reduced.

Chamber gain is also altered if one of the sense wires moves, since the charge carried by it, and adjacent wires, is then changed. From Erskine's calculations (5), in a chamber with L = 8 mm, s = 2 mm, d = 20 μm and a 75%/25% filling of argon and carbon dioxide, a displacement of 0.1 mm by a wire in the sense wire plane causes the two adjacent wires to give a 15% difference in amplification. Although not leading to such a large difference,

displacement of a wire perpendicular to the sense wire plane also alters amplification.

1.3.3 Time resolution

In a chamber with 2 mm sense wire spacing a particle passing perpendicular to the wire plane could be anywhere from 0 to 1 mm from the nearest wire. The number of electrons which need to be collected from the particle ionization to produce a detectable pulse will depend upon the threshold of the amplifier attached to the wire, but because of the variable distance of the ionization from a wire there will be a distribution of times between the passage of a particle and appearance of its pulse. Figure 1.3 shows such a distribution for pulses from a chamber with L = 4 mm, s = 2 mm, HT = 3.2 kV and an argon-isobutane gas filling (from 3). Assuming only a few electrons need be collected to exceed the amplifier threshold then a drift velocity of 4 cm/ μsec means the maximum time for them to arrive in the amplifying region around the wire is about 25 nsec, which is in good agreement with the width of the above distribution, 27 nsec. It is the jitter in the arrival time of the electrons at the wire which determines the time resolution, so in this case it is 27 nsec, but in general varies about 8 nsec above and below this time, depending upon wire spacing and gas mixture.

It is possible to apply a gating pulse to the chamber, which starts from detection of the particle by an external scintillator and ends after a pre-determined time. Only pulses which arrive within the duration of the gate pulse are accepted. This allows an alternative definition of time resolution as that gate width at which efficiency reaches 100%: figure 1.4 shows a typical curve (8).

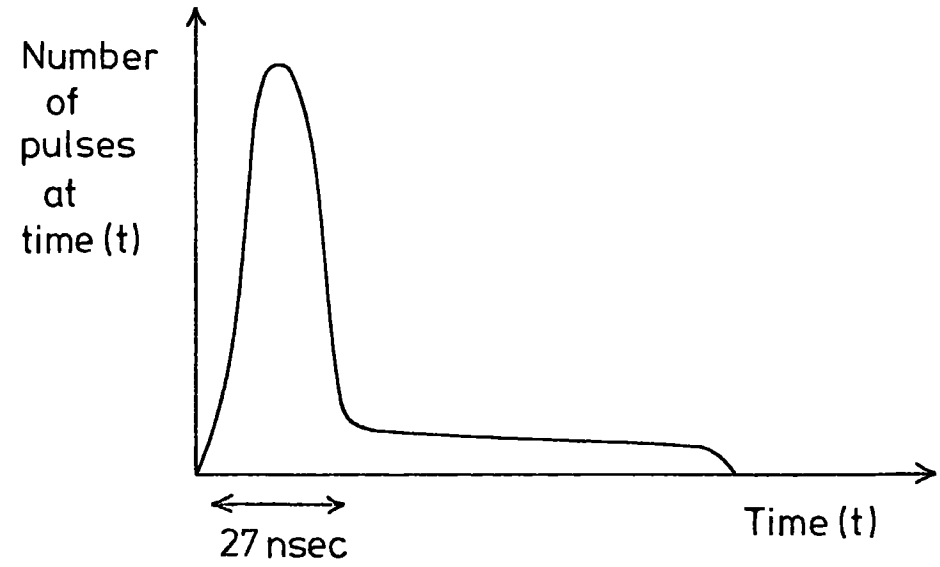

FIGURE 1.3 TIME DISTRIBUTION OF PULSES FROM ONE SENSE (ANODE) WIRE

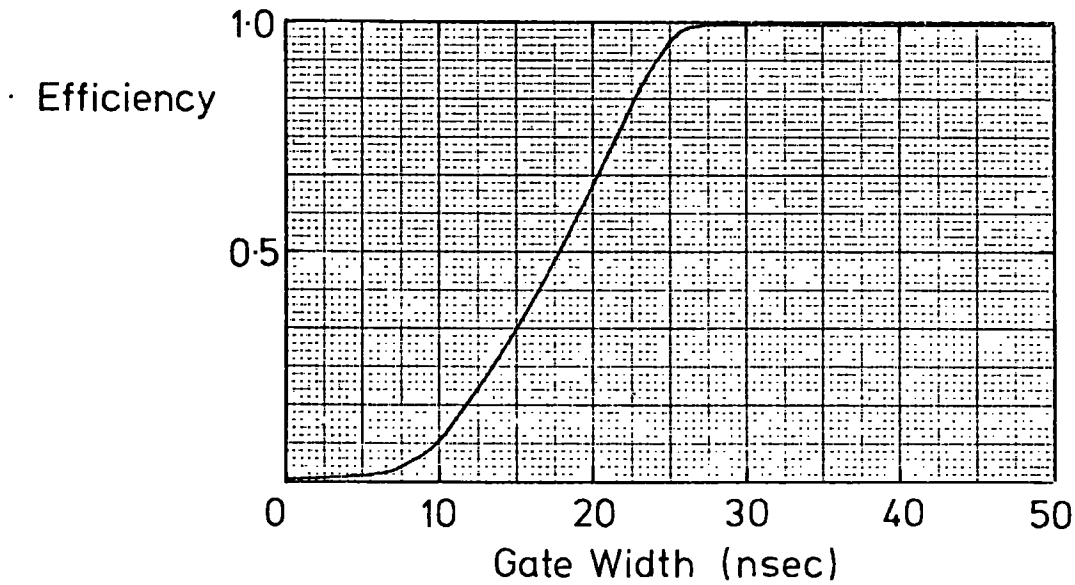

FIGURE 1.4 EFFICIENCY OF PROPORTIONAL CHAMBER AGAINST WIDTH OF GATING PULSE

1.4 Some major developments of the MWPC

Since its introduction in 1968 the basic geometry of the MWPC has remained unchanged but its mode of operation, gas filling and methods of data acquisition have undergone substantial development. Normally the MWPC is operated in the proportional mode but unless a particular experimental application requires proportionality of pulse height to ionization it is usual to increase the gain of the chamber to as high a value as possible and this can be achieved in one of two ways:

1) Increasing the H.T. until the chamber reaches the semi-proportional region, where pulse heights begin to reach saturation. With conventional gas fillings this causes the chamber to become unstable but Charpak et al. (8) discovered a suitable gas mixture for this purpose which they called 'magic gas'. It consists of argon, isobutane and freon 13 B1, roughly in the ratio 66.5 : 34 : 0.46 and its use permits chamber gains of up to 10^8 without entering into the Geiger region.

2) By raising the H.T. so that the chamber does enter the Geiger region one runs into a situation very different from a single wire chamber since in order to achieve localisation in MWPC's it is necessary that the mean free path of u.v. photons responsible for the spread of the Geiger discharge is very short so that the discharge does not propagate from one wire to another. Following the work of Grundberg et al. (9) who used a mixture of argon and ethyl bromide to limit the efficient region in MWPC's to narrow cylinders around the wires, Charpak et al. (10) found they were in fact able to localise a discharge on one wire in conventional MWPC's by operating them in the Geiger mode with this gas. Pulses of 1 volt on a 1000 Ω load were obtained over a wide range of voltage, thus greatly simplifying the type of electronics required.

Conventional sense wire spacing is 2 mm. Thus the number of wires in a chamber soon becomes quite large, and the cost also becomes large if an amplifier per wire is required. Although this is the best way of exploiting the properties of the chambers to the fullest, several methods have been proposed to try and reduce the number of amplifiers required. Two similar methods which have had limited success (11) are:

1) The plane of sense wires is built as a lumped delay line, the position of the active wire being given by the difference in the arrival time of the pulse at the two ends of the line.

2) The wires are connected to a resistive attenuator network, the ratio of the pulse heights arriving at the two ends locating the active wire.

However, both of these methods degrade the spatial resolution of the chamber, but Grove et al. (12) were able to achieve a spatial accuracy of 1 mm on a 2 mm spaced chamber by using a ceramic core (non-magnetic) type delay line.

While the spatial resolution of the MWPC is in general good (1 to 2 mm) the spark chamber is undoubtedly better (about 0.3 mm) and a Karlsruhe group have reported a novel detector (13, 14) which makes use of the better time resolution of the proportional chamber and better spatial resolution of the spark chamber. Their 'hybrid' chamber consists of a proportional chamber and a spark chamber with a drift gap between them. Information from the wires of the proportional chamber gives the logic time to decide whether to record the event, a high voltage pulse being applied to the spark chamber if the event is required. The minimum time resolution of the chamber is $\lesssim$ 100 nsec.

The latest development of the MWPC is the drift-chamber, originally investigated by Charpak in 1970(6), who built a drift space outside one of the H.T. planes of a conventional MWPC and detected the ionization of particles which traversed this space parallel to the H.T. plane. However, the most recent and successful type of drift chamber involves taking an ordinary MWPC and increasing the sense wire spacing to about 2.5 cm. The time between the particles detection by scintillators (or MWPC's) and the arrival of a pulse at a sense wire is then measured; the use of special gas mixtures which have constant drift velocities with field allows locational accuracy to 0.1 cm.

1.5 Present work

Having outlined the development and operating characteristics of the MWPC this thesis first studies a major problem concerned with large chambers, i.e. sense wire displacement.

An investigation is then made of the application of MWPC's to the detection of transition radiation, a phenomenon which is becoming increasingly important in the detection of ultra-relativistic particles (15). At the moment it seems that unless a completely new technique is developed for energy and mass determination of very high energy particles transition radiation will play a major part in the detection of particles from the new breed of accelerators, such as the Cern 300 GeV SPS. Particular emphasis is placed on transition radiation from cosmic rays, since cosmic ray research forms the major part of the work of the Durham Physics Department.

CHAPTER 1: References

1. G. Charpak, R. Bouclier, T.Bressani, J.Favier and C.Zupancic, Nuc. Inst. & Meth. 62, 262 (1968)

2. Ionization Chambers and Counters. Rossi and Staub (McGraw Hill 1949) 97

3. G.Charpak. Ann. Rev. Nuc. Sci. 20, 195 (1970)

4. B.Eiben, H.Faissner, M.Holder, J.Konig, K.Krisor and H.Umbach. Nuc. Inst. & Meth. 73, 83 (1969)

5. G.A.Erskine. Nuc. Inst. & Meth. 105, 565 (1972)

6. G.Charpak, D.Rahm and H.Steiner. Nuc. Inst. & Meth. 80, 13 (1970)

7. P.A.Souder, J.Sandweiss & A.A.Disco. Nuc. Inst. & Meth. 109, 237 (1973)

8. R.Bouclier, G.Charpak, Z.Dimcovski, G.Fischer, F.Sauli, G.Coignet, G.Flugge. Nuc. Inst. & Meth. 88, 149 (1970)

9. G.Grunberg, L.Cohen and L.Mathieu. Nuc. Inst. & Meth. 78, 102 (1970)

10. G.Charpak and F.Sauli. Nuc. Inst. & Meth 96, 363 (1971)

11. G.Charpak, R.Bouclier, T.Bressani, J.Favier and C.Zupancic. Nuc. Inst. & Meth. 65, 217 (1968)

12. R.Grove, K.Lee, V.Perez-Mendez and J.Sperinde. Nuc. Inst. & Meth. 89, 257 (1970)

13. Cern Courier, Aug. 1971, 231

14. V.Bohmer. Nuc. Inst. & Meth. 107, 157 (1973)

15. L.C.L.Yuan, C.L.Wang and S.Prunster. Phys. Rev. Lett. 23, No. 9 (1969), 496

CHAPTER 2

AN INVESTIGATION OF SENSE WIRE SUPPORT SYSTEMS FOR MULTIWIRE PROPORTIONAL CHAMBERS

2.1 Introduction

It was indicated in the first chapter that, because of induced pulses on adjacent sense wires, it was originally thought there would be no possibility of localising a discharge in a MWPC on one particular wire. Fortunately this was found not to be true but, as chambers increased in size and sense wires became longer, a further phenomenon emerged which threatened the use of large MWPC's as particle detectors. In chambers with sense wires longer than about 50 cm it was found that when the operating voltage was reached, adjacent sense wires began to displace toward opposite H.T. planes, as shown in figure 2.1. Longer wires began displacement at lower values of H.T.

Apart from impairing the spatial resolution of a chamber the above phenomenon could place the sense wires in a position of unstable equilibrium and increased the likelihood of sparking taking place between the H.T. plane and the sense wire plane, so clearly it was necessary to devise a means of overcoming the displacement.

2.2 Electrostatic Considerations

When a negative potential is applied to the H.T. electrodes like, positive charges are induced on the sense wires, the density of the charges increasing as the potential is raised. This creates a force between each sense wire proportional to the square of the charge density on the wires. In a perfectly constructed chamber

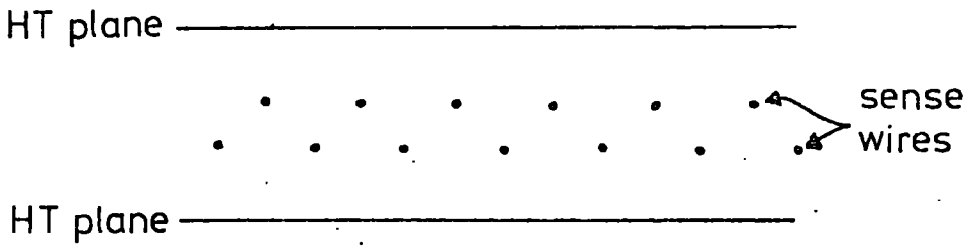

FIGURE 2.1 NATURE OF SENSE WIRE DISPLACEMENT

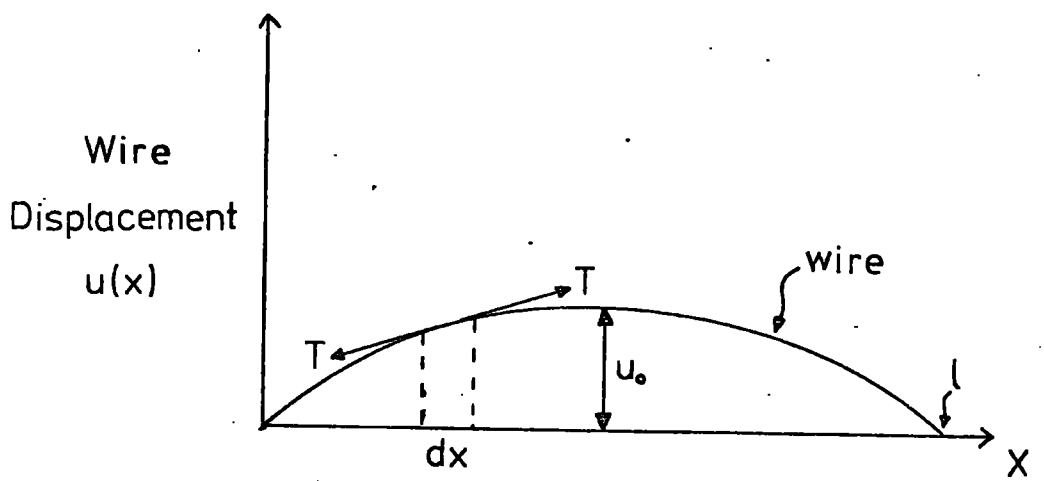

FIGURE 2.2 SECTION ALONG A DISPLACED SENSE WIRE

all these forces would lie in a straight line in the sense wire plane and each wire would feel a net force, in any direction, of zero. However, in practice, some wires will always be out of line with others (if only by a few microns), and consequently there is generally a small component of this repulsive force perpendicular to the sense wire plane.

At low voltages this particular force is counteracted by the tension of the wire but at some critical voltage this tension can no longer withstand the repulsive force and the wires displace. The theoretical analysis of the forces involved here has been studied by Trippe (1) and the next section is a brief outline of his treatise.

2.3 Theoretical Analysis

When the sense wires are displaced as in figure 2.1 the field at a distance 'd' from a wire is:

$$E = {}^{2q}/_{d} \qquad 2.1$$

where q = charge per unit length on the sense wire.
Therefore the force this wire exerts on another wire a distance 'd' away is:

$$F_1 = {}^{2q^2}/_{d} \qquad 2.2$$

When alternate wires are displaced up and down a distance 'u', where $u \ll s$, it can be shown (Appendix I) that the total force on unit length of one wire, from the vector sum of forces from all the other wires, is:

$$F_2 = \frac{\pi^2 q^2}{s^2} u \qquad 2.3$$

In addition to the repulsive force on each wire there is also an attractive force exerted by charges on the H.T. plane and the magnitude of this, calculated by the method of images (Appendix I) is given by:

$$F_3 = \frac{\pi^2 q^2}{4a^2} u \qquad 2.4$$

where a = separation of H.T. plane and sense wire plane.

Thus when 'a' is large compared to the wire spacing 's', a condition which is normally fulfilled in MWPC's, F_3 can be neglected in comparison to F_2. In fact, only when the H.T. plane-sense wire separation is half the sense wire spacing do both forces have the same magnitude.

Figure 2.2 shows a section along a displaced wire; if the wire is under tension T then it can be shown that the restoring force, R, per unit length at a point where the displacement is u(x) is given by:

$$R = T \frac{d^2u}{dx^2} \qquad 2.5$$

It is easily shown from Hooke's Law that when $u \ll l$, where l is the sense wire length, the increase in wire tension due to the lateral displacement 'u' is negligible compared with the original tension T.

When the displaced wires reach a position where their restoring force equals the repulsive electrostatic force, then equating equations 2.3 and 2.5:

$$T \frac{d^2u}{dx^2} = - \frac{\pi^2 q^2}{s^2} u \qquad 2.6$$

This simple differential equation has a solution:

$$u(x) = u_o \sin \left| \frac{\pi q}{s\sqrt{T}} x \right| \qquad 2.7$$

where u_o is the displacement at the mid-point of the wire. Boundary condition requirements are that $u(x) = 0$ at $x = 0$ and $x = l$; thus:

$$\frac{\pi q}{s\sqrt{T}} = \frac{\pi}{l} \qquad 2.8$$

$$\text{i.e.} \qquad T = \frac{q^2 l^2}{s^2} \qquad 2.9$$

Therefore to prevent the wires displacing we require:

$$T > \frac{q^2 l^2}{s^2} \qquad 2.10$$

If C = capacitance per unit length of a wire and V = H.T. applied to chamber, then $q = CV$ and, by considering the H.T. and sense wire planes as parallel plates, one can show that:

$$C = \frac{s}{2\pi a} \qquad 2.11$$

Substituting for q and then C in inequality 2.10:

$$T > \frac{V^2 l^2}{4\pi^2 a^2} \qquad 2.12$$

Because the MWPC is not an exact analogue of the parallel plate arrangement the value of capacitance used in the above treatment is higher than in reality so inequality 2.12 is an overestimate. However when s = 2mm and a = 0.8 cm, for example, the discrepancy is calculable as less than 20%.

2.4 Test of Theory

In order to determine the validity of inequality 2.12 tests were performed on a chamber consisting of two large identical frames, X and Y, with dimensions as shown in figure 2.3.

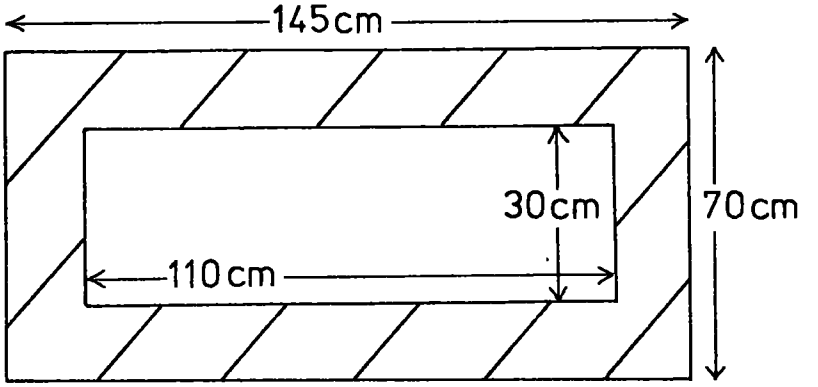

FIGURE 2.3 DIMENSIONS OF THE PROPORTIONAL CHAMBER FRAMES, X AND Y

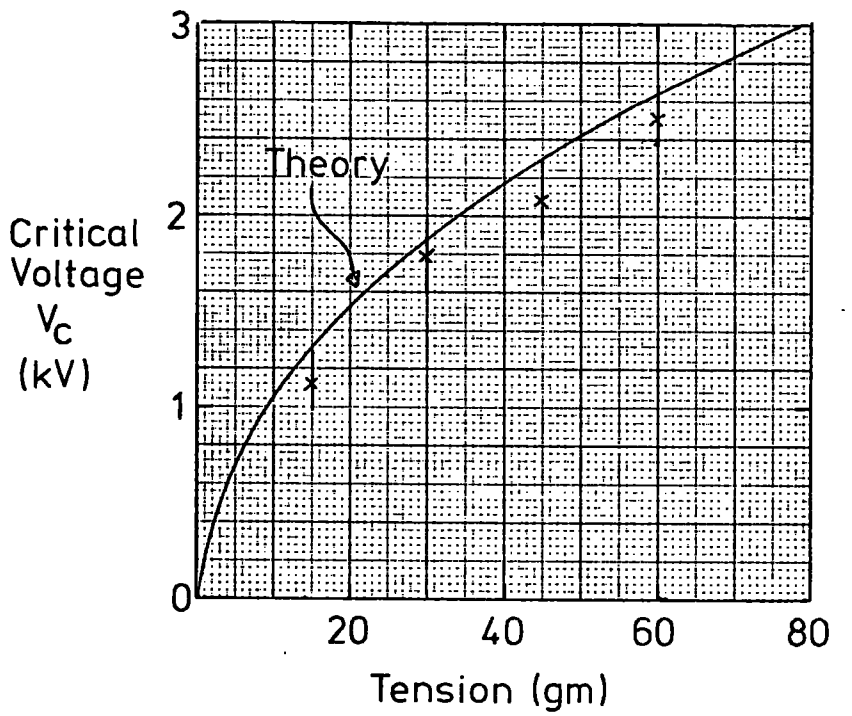

FIGURE 2.4 CRITICAL VOLTAGE, V_c, AGAINST SENSE WIRE TENSION (EXPERIMENT AND THEORY)

The sense wires, 25 μm diameter gold plated tungsten, were wound in the long direction on top of frame X and soldered to copper strips at each end of this frame in sets consisting of 20 wires with a 2 mm spacing between wires, each set having a different tension and being earthed by 10 kΩ .

One H.T. plane was wound with 125 μm diameter wire (98% copper, 2% beryllium) on top of frame Y such that the wire direction was perpendicular to the sense wires, and the wire spacing 2 mm. Frame Y was placed on top of frame X and an aluminium sheet on the underside of frame X acted as the second H.T. plane. The complete chamber was clamped to a $\frac{3}{4}$" thick piece of blockboard to enable it to be placed in a vertical position without distortion.

As the potential on the H.T. planes was raised each set of sense wires began to displace, in turn, in the manner shown in figure 2.1. The critical voltage, V_c , is defined as that voltage at which sense wire displacement begins; its theoretical value from inequality 2.12 is:

$$V_c^2 = \frac{4\pi^2 a^2 T}{l^2} \qquad 2.13$$

Figure 2.4 shows a plot of this formula for the particular values of 'l' and 'a' pertaining to the test chamber. The experimental points agree very well with the theory, thus proving the validity of equation 2.13. It would appear that the overestimation of the capacitance is not too serious as there is no indication that the theoretical relation in this figure is too high.

It should perhaps be pointed out that the voltage at which a particular set of wires displaces is very marked; they are almost stationary until the voltage reaches V_c , when they begin to displace very rapidly for small increases in voltage. Figure

2.5 shows a graph of wire displacement against voltage from a test carried out on another special chamber, where the sense wires, which were 80 cm long, could be observed through a travelling microscope, and for which V_c = 1,3 kV, from equation 2.13.

2.5 Consequence

Although some of the earlier MWPC's used stainless steel sense wires (e.g. 2) by far the most common sense wire material is now gold plated tungsten, with a diameter of either 25 μm or 12.5 μm, the breaking strain of which is about 70 gm and 20 gm respectively. The major reason for the use of tungsten is its high tensile strength, but because it is extremely difficult to solder tungsten the latter is coated with a thin film of gold.

In chambers with 25 μm diameter sense wires the latter are usually wound with 50 gm tension, to provide an adequate safety margin against the wires breaking. Figure 2.6 shows the relationship between critical voltage and wire length for a constant tension of 50 gm (derived from equation 2.13) and when the sense wire length is greater than about 70 cm the critical voltage is below the H.T. voltage generally required to produce adequate gas gains (10^3 upwards) with conventional gas fillings and wire spacing, i.e. about 4 kV. It should be noted that the working voltage for a constant H.T. plane-sense wire separation does depend upon sense wire separation, a parameter on which wire displacement is independent.

Thus the wire displacement to which large chambers are prone must be prevented by a suitable form of wire support.

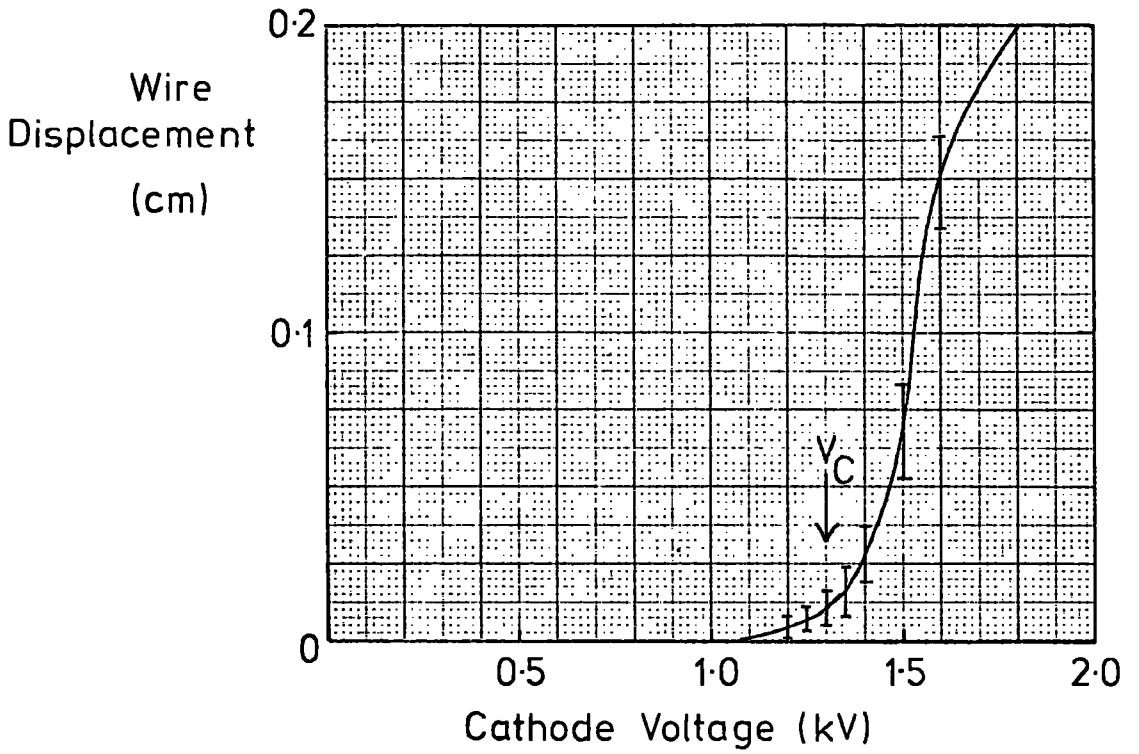

FIGURE 2.5 MID-WIRE DISPLACEMENT AGAINST CATHODE VOLTAGE FOR $l = 80$ cm (EXPERIMENT)

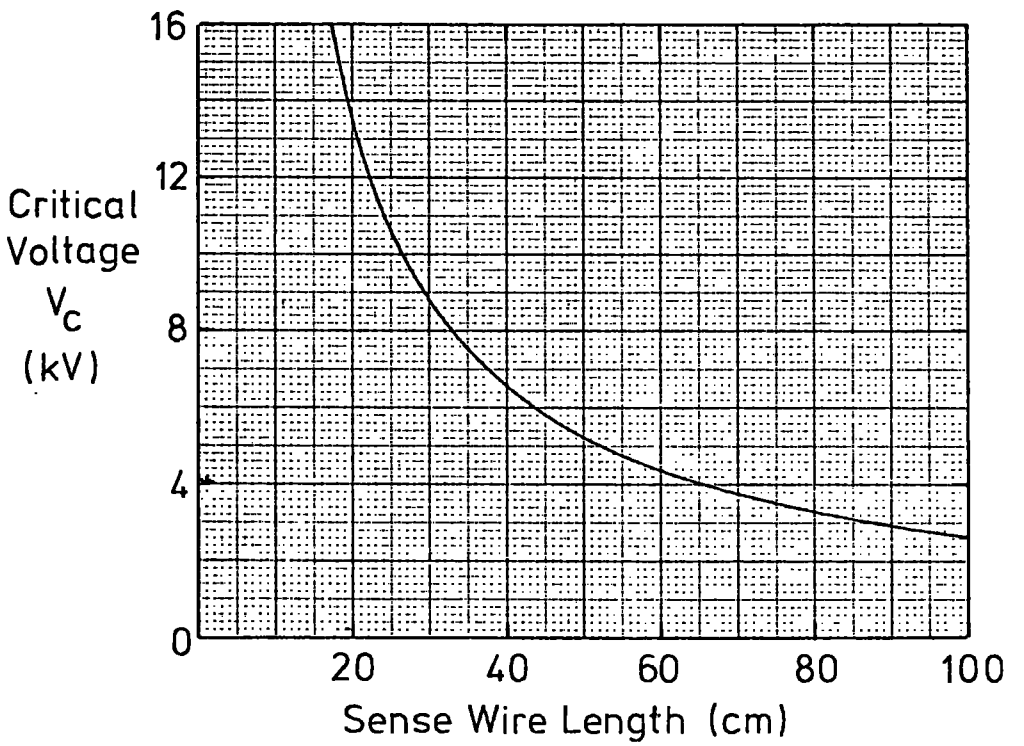

FIGURE 2.6 CRITICAL VOLTAGE AGAINST SENSE WIRE LENGTH FOR T = 50 gm (THEORY)

2.6 Review of Recent Methods

Considering the importance of MWPC's and the time and money spent in their development very little effort has been put into the problem of counteracting sense wire displacement. Of the work that has been done there seem to emerge two distinct types of support:

i) A support line (e.g. nylon, insulated wire) stretched across the chamber perpendicularto, and touching, the sense wires (3,4,5,6).

Original methods with nylon lines involved spanning them across and glueing them to the sense wires. However, it was found that the nylon became slack after a time (6) resulting in an undesired movement of the sense wires.

Later attempts consisted in stretching the nylon on both sides of the wire plane, either woven through the wires in opposite sense at regularly spaced intervals along the chamber, or with both lines stretched across the wires at the same point and bound together every few centimetres.

A further alternative has been the use of a taut PVC insulated copper wire which is connected to a high voltage supply to raise the potential of the copper as required.

ii) Various kinds of solid spacer which hold the sense wires relative to the H.T. wires (3). This type of support can be, for example, a rectangular strip of styrofoam, about 2 mm wide, placed on alternate sides of the wires at equally spaced intervals along the chamber.

2.7 Required Properties of Support

When developing a support line for sense wires two important points need to be taken into account:

i) The dead-space created by the support should be kept as small as possible (the term dead-space has two different definitions which will be given in § 2.11, but for the present can be taken as the extent of the inefficient region of the chamber created by, and perpendicular to, the support). The main reason for this is the large cost of high energy physics experiments; chambers are usually made as large as the environment of the particular experiment will allow and anything which effectively reduces the active area of the chamber is undesirable.

ii) The support should be mechanically strong and rigid as the force it has to withstand from the sense wires when they are trying to displace is quite considerable. In addition it should be designed to enable easy replacement of a broken wire, because of which methods that involve glueing the sense wires to the support line are avoided where possible.

The support lines of method (i) in § 2.6 generally exhibit small dead-spaces, approximately 5 to 10 mm, but suffer from the drawback of not holding the sense wires rigidly when under pressure, whereas the solid spacer support, generally as rigid as the chamber frame itself in preventing the wires from moving, do create an unacceptably large dead-space, typically around 2 cm. What is required, therefore, is a relatively narrow support capable of remaining rigid when under pressure from the sense wires.

2.8 Types of Support Tested

Bearing in mind the points mentioned in the last section several types of nylon and melinex supports were investigated with the chamber in figure 2.3. From the mechanical and rigidity point of view the following two were found to be the most satisfactory:

i) Two nylon lines stretched above and below the sense wires at the same point and either tied together with thin pieces of nylon or glued with small blobs of araldite at intervals. The nylon line used in these tests had a diameter of 0.3 mm and was strung with a tension of approximately 400 gm.

ii) A thin melinex strip, 3 mm wide and with its plane perpendicular to the sense wire plane. The strip used in this work was 125 μm thick and was stretched as tightly as possible across the chamber and firmly clamped into recesses in the chamber frame.

In addition the chamber in which the dead-space experiments were carried out incorporated two PVC insulated copper wires which were stretched across the wires in exactly the same manner as the two nylon lines.

2.9 Experimental Arrangement

2.9.1 Introduction

Preliminary measurements were carried out in the laboratories at Durham with three small MWPC's to obtain a rough idea of the extent of the melinex and nylon spaces; the main point of these tests was to ascertain that the new support, the melinex strip, did not produce an excessively large dead-space.

More exhaustive measurements were carried out on a large MWPC at Daresbury Nuclear Physics Laboratory. This chamber was a

prototype to a set of seven chambers to be built for use in their forthcoming LAMP experiments and it was for this project that the original sense wire support investigations were begun.

2.9.2 Chamber characteristics

The prototype chamber had an active area of 133 cm x 62 cm and its frame, made from a glass epoxy laminate (G 10) had external dimensions 147 cm x 72 cm. The sense wires, 25 μm gold plated tungsten, were strung with a tension of 50 gm along the length of the chamber with a spacing between each wire of 2 mm. The H.T. planes, 6 mm away from the sense wire plane, consisted of 125 μm diameter copper-beryllium wire wound across the width of the chamber at a tension of 200 gm and spacing of 1 mm. For the measurements reported here the chamber was continuously flushed with a mixture of argon and isobutane (0.9 litres/min and 0.6 litres/min respectively), the former being bubbled through methylal at 0^{o}C.

The three different sense wire supports mentioned in § 2.8 were equally spaced at quarter lengths along the chamber. In addition there were two sets of double nylon cords on each set of H.T. wires as a safeguard against these planes moving from electrostatic repulsion.

Two small proportional chambers were used for particle trajectory definition. Their frames were made from perspex with an active area of 10 cm x 8 cm. The sense wire spacing was 2.5 mm, but in all other respects they were identical to the large chamber. They were flushed with a mixture of argon and carbon dioxide (0.3 litres/min and 0.1 litres/min respectively) and operated from a second H.T. supply.

2.9.3 Chamber arrangement

The two small chambers (A and C) were mounted on a rigid frame, with one chamber above and one below the large chamber (B), such that their sense wires were perpendicular to those of chamber B, i.e. parallel to the wire supports. A side view of the arrangement is shown in figure 2.7.

One wire only in each of chambers A and C was used for particle detection and the chambers were positioned such that these two wires were vertically one above the other. Electrons were produced from a 2mC source of Strontium 90 which was placed in the vertical plane defined by the above two wires; this plane, perpendicular to the sense wire plane of chamber B, thus defined the electron trajectories. The frame in which chambers A and C were mounted could be moved along a scale parallel to the sense wires of chamber B, as shown in figure 2.7.

Coincidences between the single wires of the two chambers A and C corresponded to particles traversing the plane defined by these wires and the output of chamber B could then be strobed to check whether the particle had been detected in it. The following section describes how the above electronic functions were performed.

2.9.4 Electronics

All three chambers were operated from the MECL II series integrated circuitry.

Each wire of chamber B was connected to an amplifier and series of flip-flops; figure 2.8 shows the layout for a single channel. The first half is a three-stage amplifier incorporating a MECL 1035 integrated circuit, cascaded as shown in figure 2.9. It consists of an amplifier of gain six, a discriminator set at 6 mV, i.e. pulses of less than 1 mV donot trigger the circuit, and

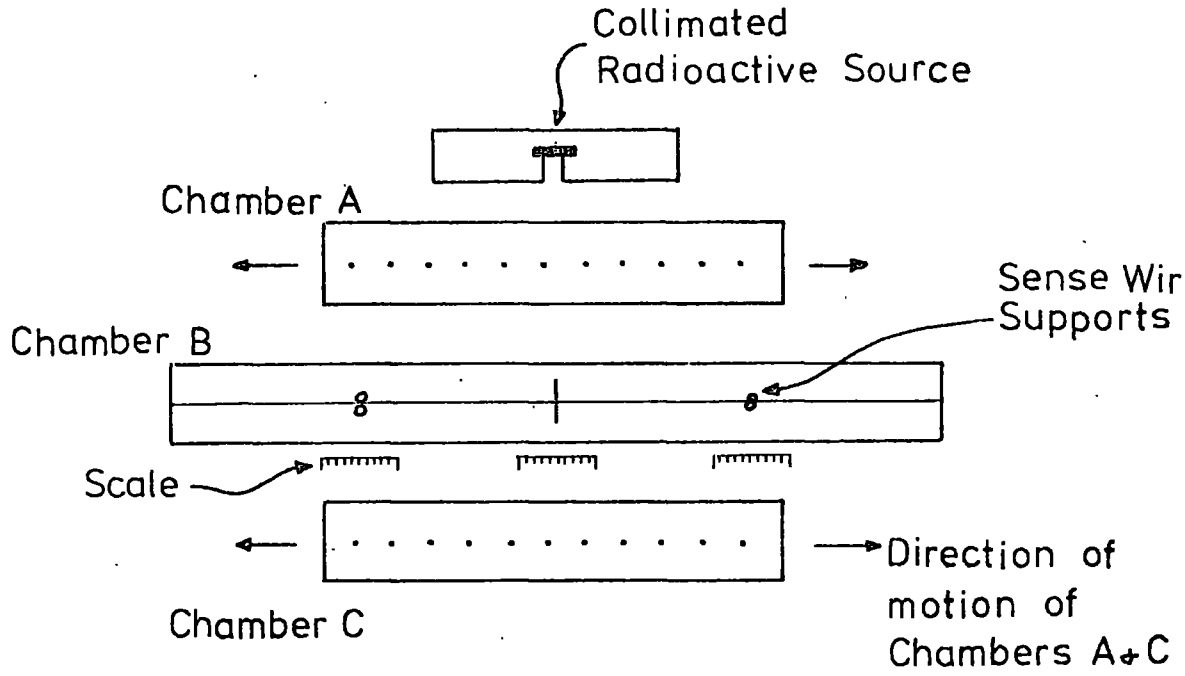

FIGURE 2.7 EXPERIMENTAL ARRANGEMENT FOR DEAD-SPACE MEASUREMENTS

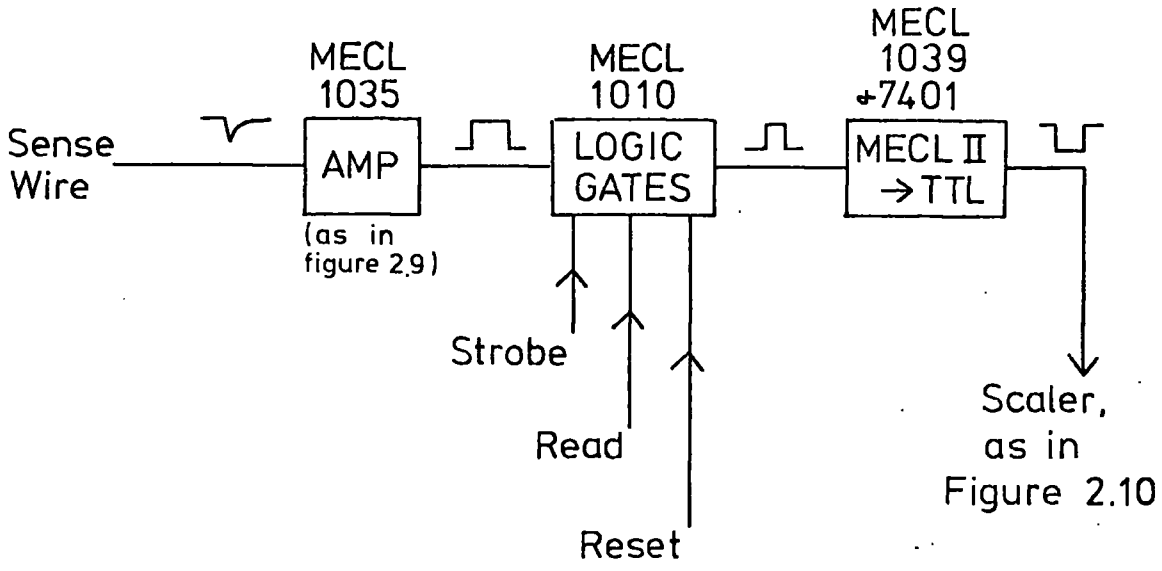

FIGURE 2.8 ELECTRONICS FOR A SINGLE CHANNEL

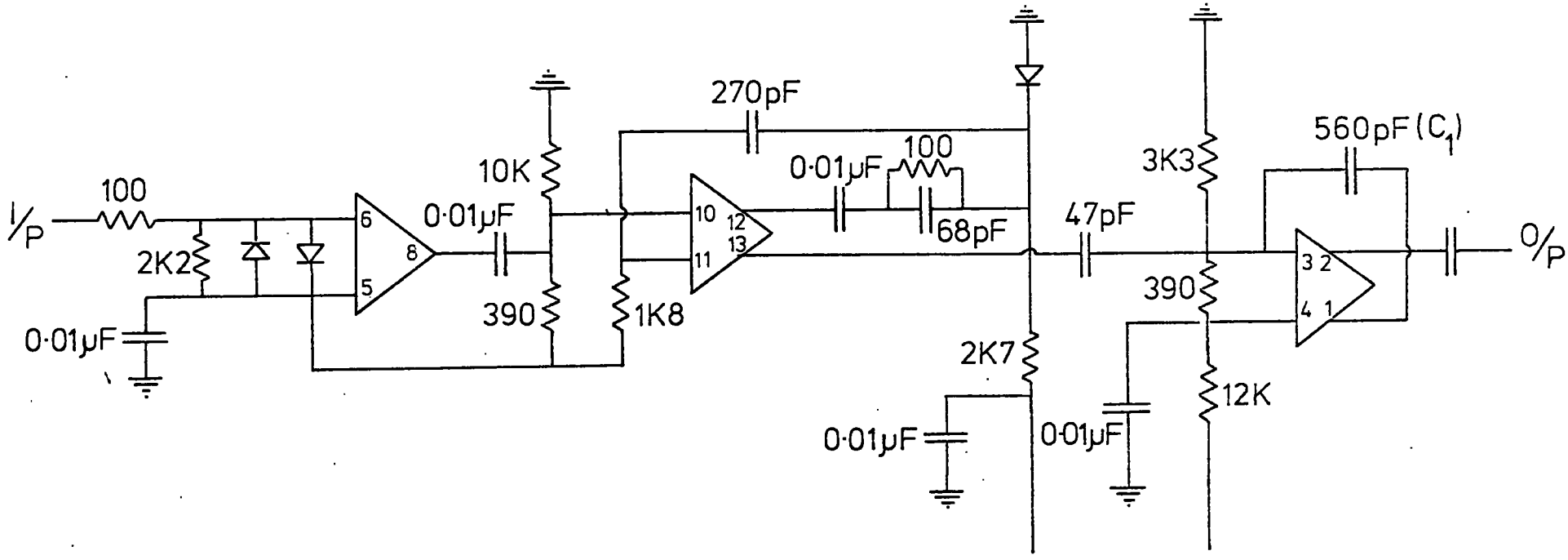

FIGURE 2.9 SINGLE WIRE AMPLIFIER (FROM MECL 1035 INTEGRATED CIRCUIT)

a pulse shaper; the output pulse length is controlled by capacitor C1.

In the second half of the circuit this output pulse (positive) is differentiated, and if the negative spike at the end of the pulse overlaps with a negative MECL II strobe pulse then the first gate in the MECL 1010 gives a positive output. The output of the flip-flop formed by the next two gates is then negative and when a negative read pulse arrives at this gate its output becomes positive. The MECL 1039 and 7401 gates invert this positive pulse and convert it to a negative TTL signal. Thus the detection of a particle by a wire causes a negative TTL output from the circuit, provided the correct strobe, read and reset pulses are generated.

For the purposes of the present dead-space measurements sixteen adjacent sense wires in the centre of chamber B were used and, as it was unnecessary to know from which wire a pulse had come, the outputs of all sixteen wires were summed.

Each wire of the two smaller chambers A and C was connected to an amplifier of the type shown in figure 2.9. After inversion the outputs of these were fed into a coincidence unit which formed part of the fast decision making logic shown in the electronic arrangement of the whole experiment in figure 2.10. The coincident pulse was fanned out to a scaler and gate generator, which gated the coincidence circuit for the cycling time of the electronics, and to three discriminators which in turn provided the strobe, read and reset pulses. As described earlier, the strobe pulse determined whether the particle was registered and this was indicated by scaler (1). The reset pulse was fed back to the gate generator to end the gating cycle. The delay after the fan-out

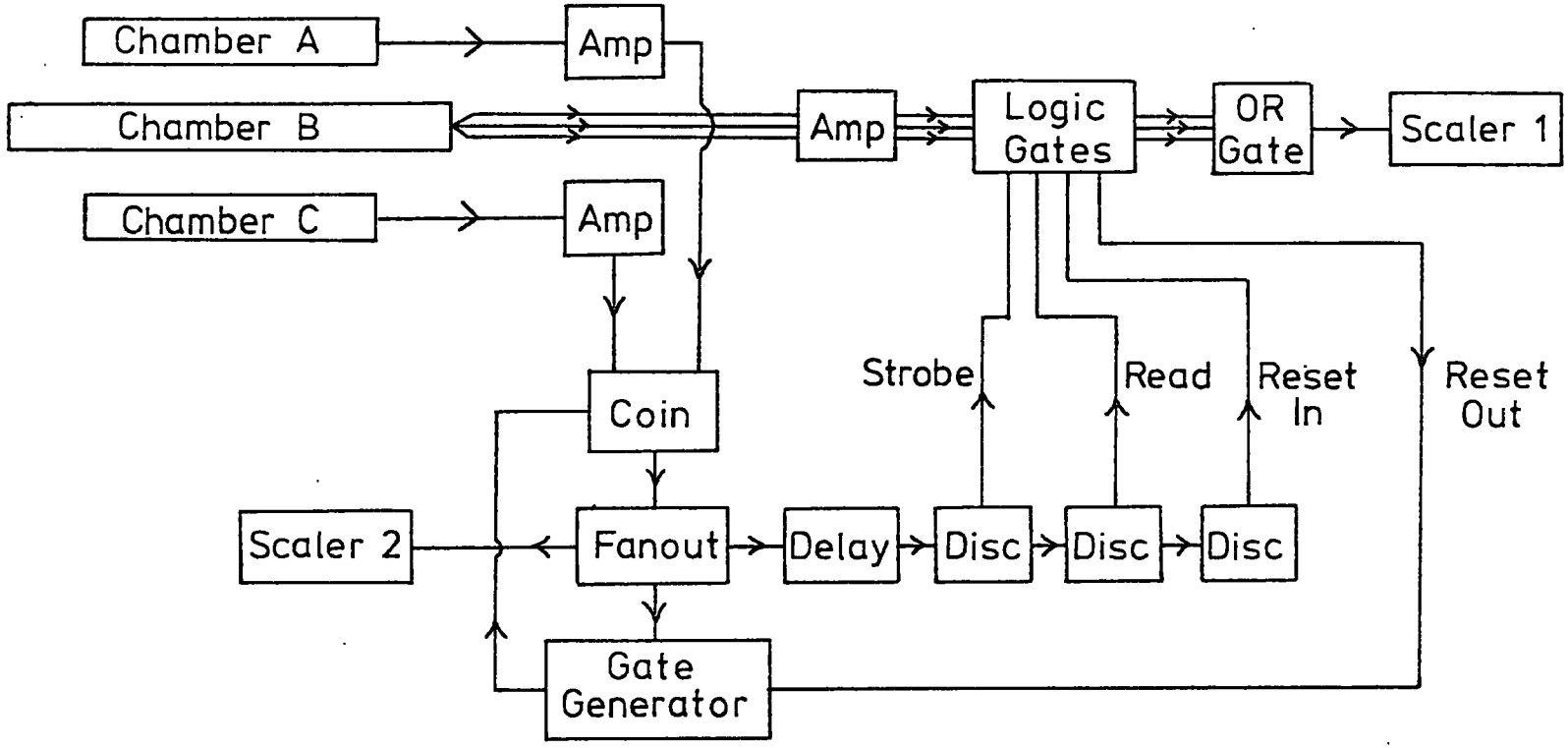

FIGURE 2.10 ELECTRONIC ARRANGEMENT FOR DEAD-SPACE MEASUREMENTS

was adjusted such that the front edge of the earliest pulse from the chamber was coincident with the front edge of the strobe pulse. The width of the latter then determined the gating time applied to the chamber.

Scaler (2) indicated the number of coincidences between A and C and hence the ratio of the two scaler readings determined the efficiency of chamber B.

The coincident logic shown in figure 2.10 used in this particular experiment was NIM standard so the strobe, read and reset pulses generated by it necessarily had to be converted to MECL logic before being fed into the 1010 gates, and conversely the TTL output of these gates had to be converted to NIM before being OR'd. These conversions were achieved by using Daresbury built 'block-boxes' which are not shown in figure 2.10.

2.10 Experimental Procedure

Before performing the dead-space measurements it was necessary to ensure that chamber B was operating at 100% efficiency away from the wire supports, this being determined by the ratio of scaler (1) counts to those of scaler (2). Figure 2.11 shows efficiency versus H.T. curves for strobe widths of 400, 100 and 40 nsec. The working range for the first two strobe widths is 5.0 - 5.3 kV; above 5.3 kV the chamber became very unstable with sense wires beginning to vibrate and an excessive dark current ($> 2\,\mu A$) being drawn. Below 5.0 kV every particle pulse was not able to exceed the discrimination level in the 1035 amplifier. For a 40 nsec strobe the chamber only reached maximum efficiency at 5.3 kV so consequently it was not useful to make measurements at smaller gating times.

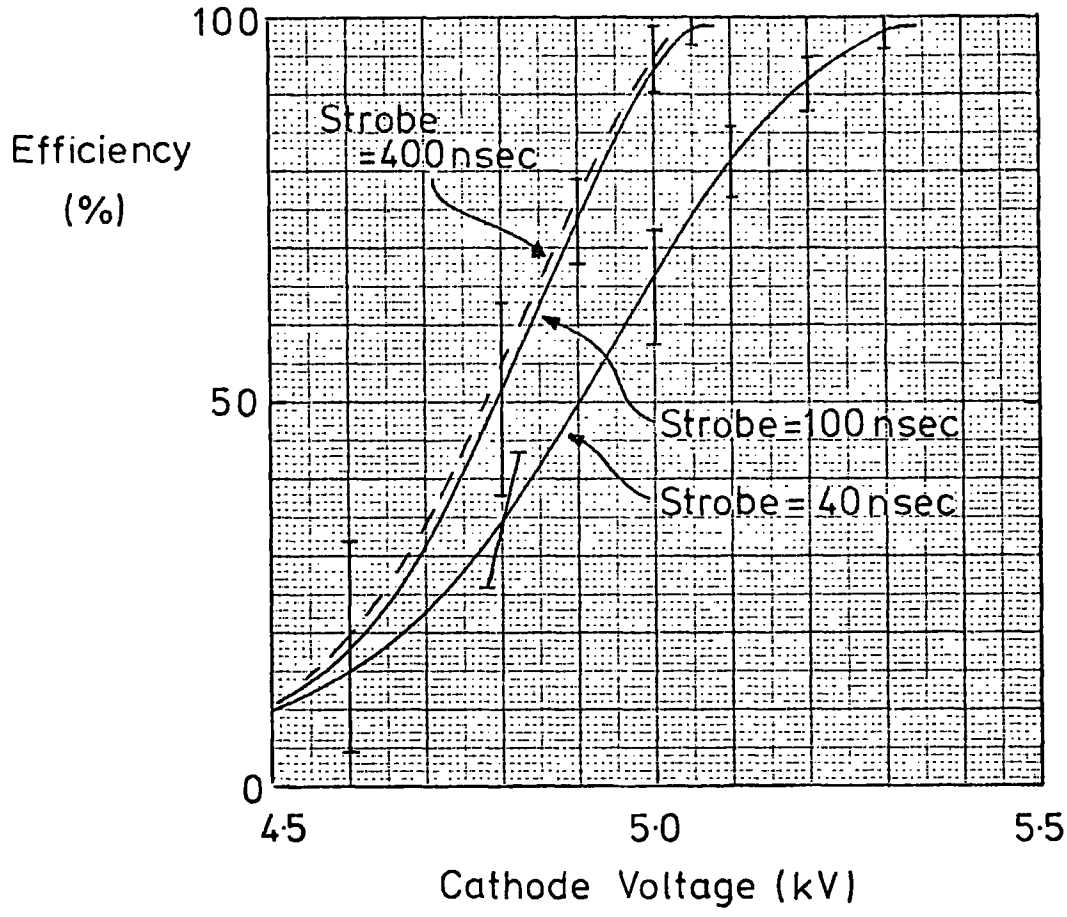

FIGURE 2.11 EFFICIENCY OF CHAMBER 8 AGAINST HT (CATHODE) VOLTAGE

(In the actual experiment the maximum efficiency never rose above 93% but this was found to be due to the fact that one of the sixteen OR gates was not working. Thus all results have been corrected to allow for this malfunction). In all the tests to be described the chamber was operated at 5.3 kV.

The efficiency of the chamber around each of the sense wire supports was determined by scanning the chamber at that particular point, i.e. the two small chambers were moved over the area around each support strip and efficiency measurements taken every two millimetres for each of the strobe widths.

Because the wire supports were equally spaced along the length of the chamber, i.e. separated by 33 cm, there was no danger of the dead-space created by one support interacting with that of an adjacent one.

2.11 Results

The efficiency of the chamber around the PVC, melinex and nylon supports for strobe widths of 100 and 40 nsec is illustrated in figure 2.12 (a), (b) and (c), which show best fit curves through the experimentally measured data. The data for 400 nsec strobe width (essentially infinite gate width) coincides almost exactly with that for 100 nsec and the respective curve has therefore been omitted from figure 2.12.

For each strobe width the support was 'scanned' three times and the errors quoted are the standard errors of the three measurements at each source position. Because the error at each position is almost independent of strobe width error bars have only been plotted on one curve in each of figures 2.12 (a), (b) and (c) to avoid confusion and overlap.

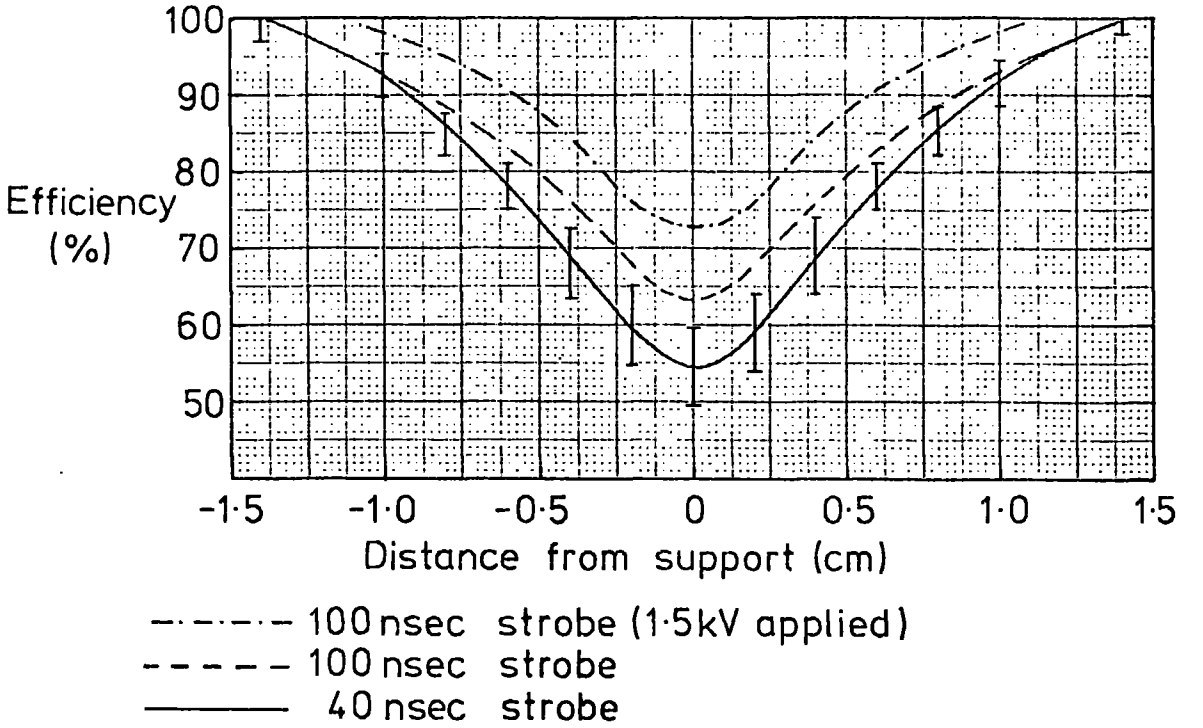

FIGURE 2.12(a) EFFICIENCY OF CHAMBER B AROUND PVC SUPPORT

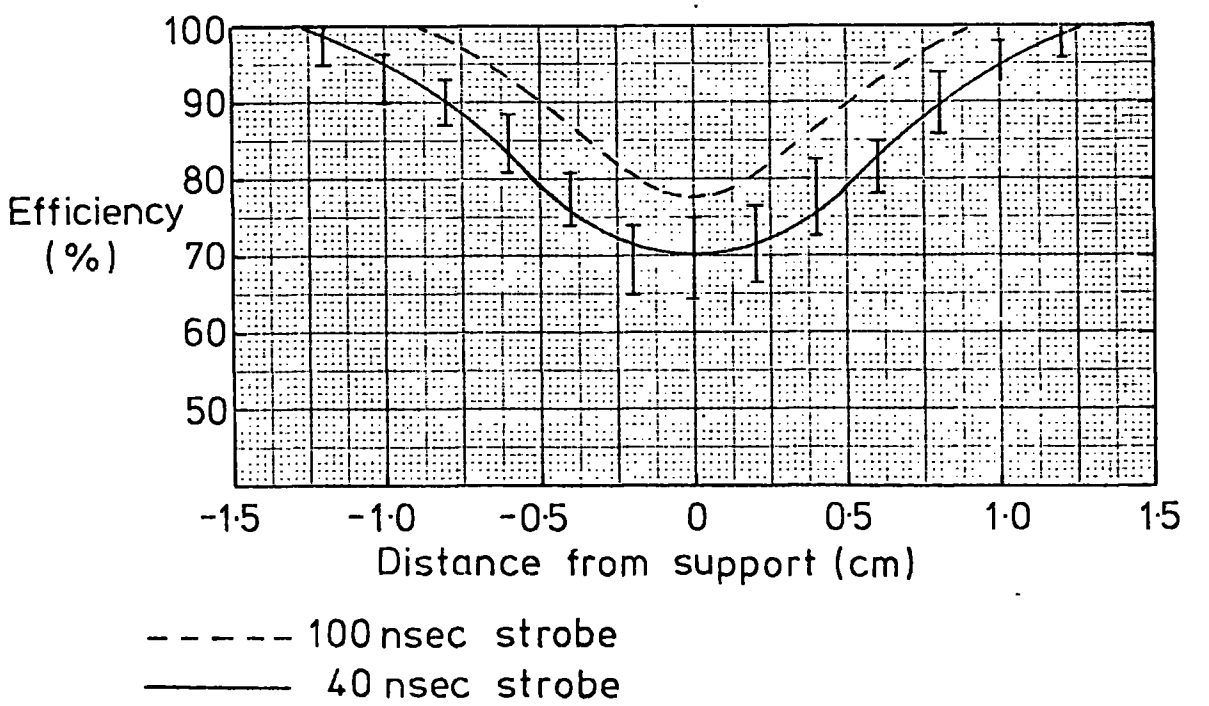

FIGURE 2.12(b) EFFICIENCY OF CHAMBER B AROUND MELINEX SUPPORT

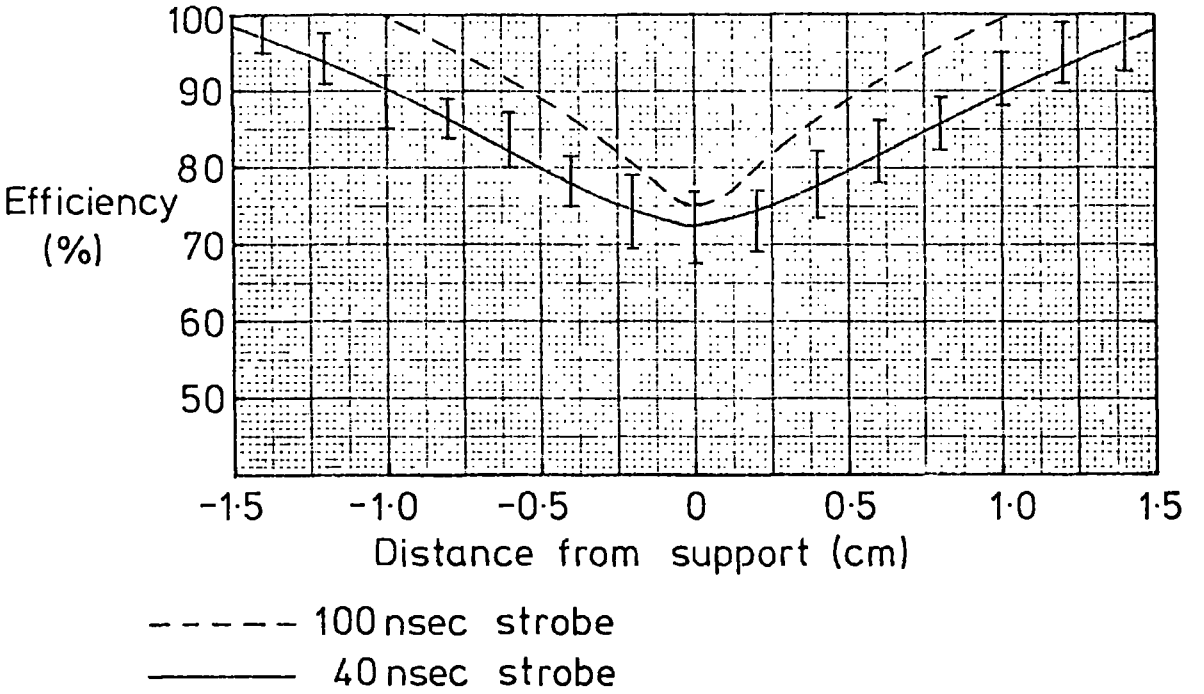

FIGURE 2.12(c) EFFICIENCY OF CHAMBER B AROUND NYLON SUPPORT

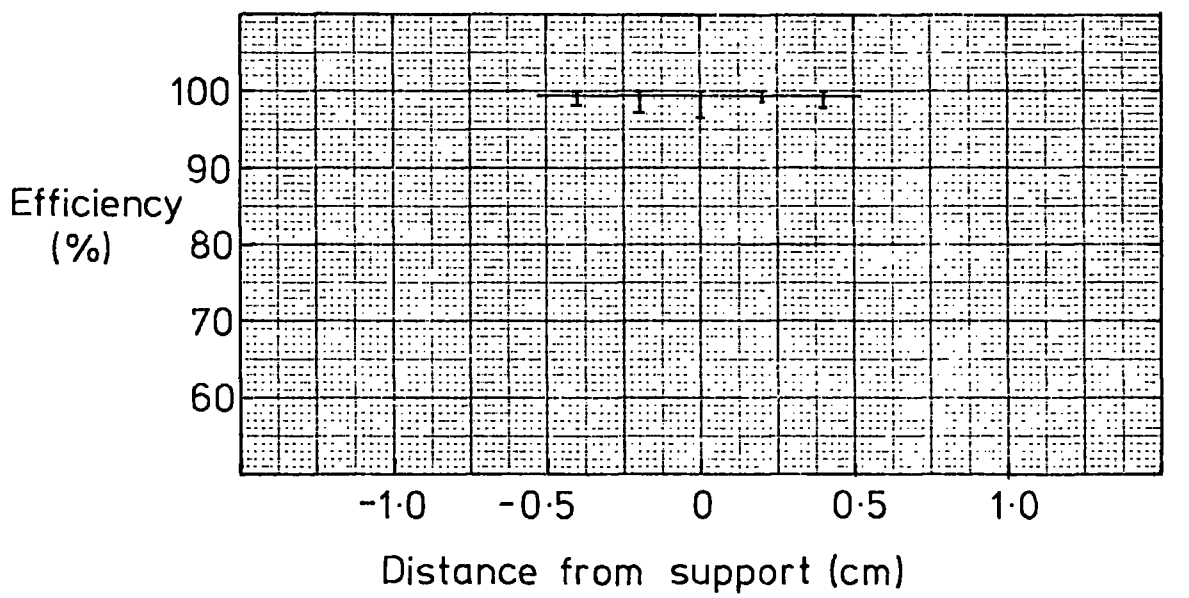

FIGURE 2.13 EFFICIENCY OF CHAMBER B OVER CATHODE SUPPORT LINE

In order to quote a particular dead-space from these curves requires a definition of this term. From previous work on wire supports there appear to be two different definitions:

i) The full-width half-maximum (FWHM) of the curve of efficiency against distance from wire support (S).

ii) Kleinknecht et al. (3) define dead-space as the width of the rectangular region extending from 0 to 100% on such a graph as figure 2.12 and which has the same area as that under the efficiency curve.

The absolute values of dead-space according to the above definitions are given in Table 2.1. The figures for definition (i) are taken directly from the curves of figure 2.12, while those of definition (ii) were evaluated by determining the area under each curve and replotting this as an equivalent area rectangle extending from 0 to 100% efficiency.

TABLE 2.1

Support	Strobe (nsec)	Dead Space	
		Method (i) (mm)	Method (ii) (mm)
PVC 1.5 kV	100	8.4	5.2
PVC 0 kV	100	10	8.4
PVC 0 kV	40	11	14.1
MELINEX	100	10	4.1
	40	13	8.0
NYLON	100	8	4.4
	40	16	8.4

Measurements over the nylon cords on the H.T. plane showed there was no deterioration in the chamber detection efficiency at the points where these were. Figure 2.13 shows the efficiency curve obtained over one of these supports.

2.12 Discussion

Although the shapes of the curves for all three wire supports in figure 2.12 are similar there are certain points worthy of mention.

Depending upon the definition one uses for dead-space there can be a large difference in the value of the figure quoted. In particular a support which creates a very low efficiency at a source position of 0 mm yet which has little effect a few millimetres away will have a relatively small dead-space by definition (i) but a substantial one on definition (ii) - this is partly the case for the PVC support.

On the other hand a support causing only a small relative drop in efficiency, but whose influence extends over a centimetre or so, has a large dead-space on definition (i) and a relatively small one on definition (ii) - this is typical of the case of the melinex and nylon supports.

On the basis of these comments it would appear that the melinex and nylon supports are far better than the PVC one. In addition it is only possible to reduce the dead-space of the PVC support to a value similar to the melinex and nylon by applying a negative potential to the inner copper wire and this can be hazardous on a detector as sensitive as a proportional chamber. Indeed it was found that 1.5 kV was the highest potential which could be attained before random noise pulses began emanating from

the chamber, and these increased in number and magnitude as the potential was raised even higher. The noise was thought to be due to either breakdown between the surface of the PVC and the sense wires or breakdown between the chamber frames through which the PVC passed.

The dead-space measured for any sense wire support should be dependent to some extent on chamber parameters, gas mixture and, in particular, the threshold of the amplifier. With respect to the latter one would expect that when the particle enters the chamber at large angles of incidence, θ, thus leaving a factor $\sec\theta$ more ionization, the dead-space would decrease. Further work has been carried out on this with three 10 x 8 cm^2 active area proportional chambers set up in a similar manner as for the experiment with the large chamber (7, 8), the discriminators of their respective amplifiers being set at a threshold of 6 mV again. Figure 2.14 shows the variation of dead-space with angle of incidence for the melinex support (this particular one was 175 μm thick and 5.5 mm wide), as determined by definition (ii) of § 2.11, for particle trajectories incident obliquely on the sense wire plane at the position of the support. It is clear that the absolute value of dead-space does, indeed, decrease with increasing angle of incidence.

In addition it was found that the maximum value of inefficiency decreased as the angle of incidence increased; this again is attributable to the fact that more ionization is deposited. Figure 2.15 shows the variation of this parameter with angle of incidence.

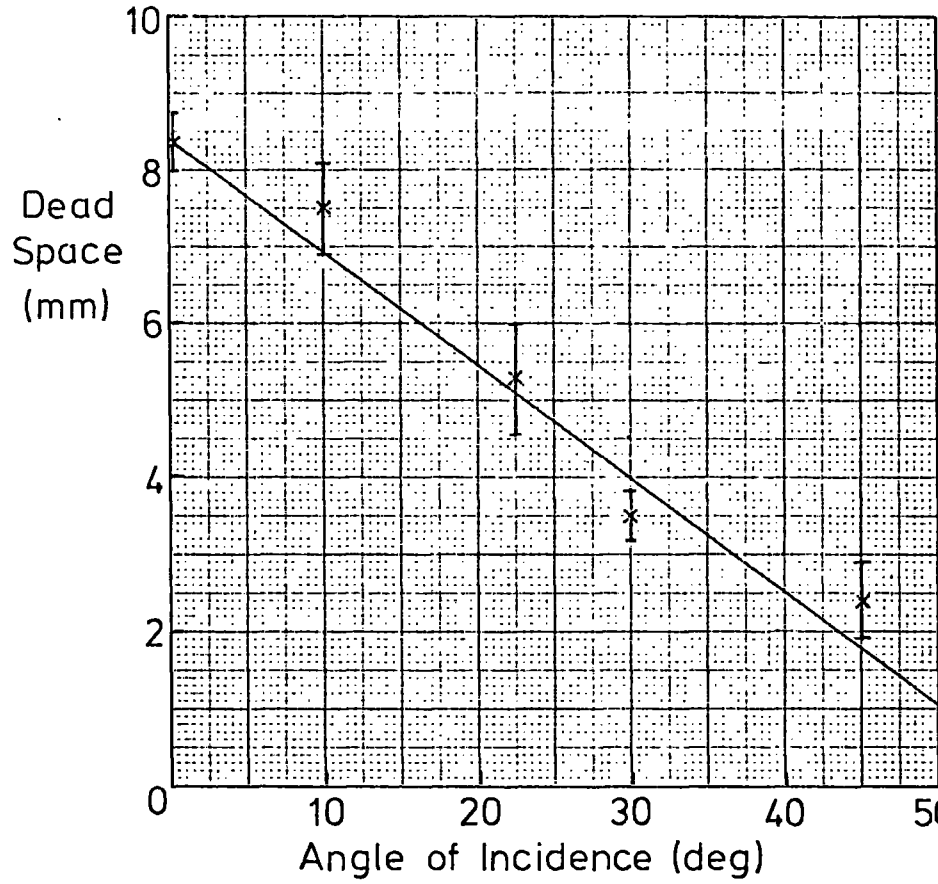

FIGURE 2.14 DEAD-SPACE AGAINST ANGLE OF INCIDENCE OF PARTICLE FOR MELINEX SENSE WIRE SUPPORT

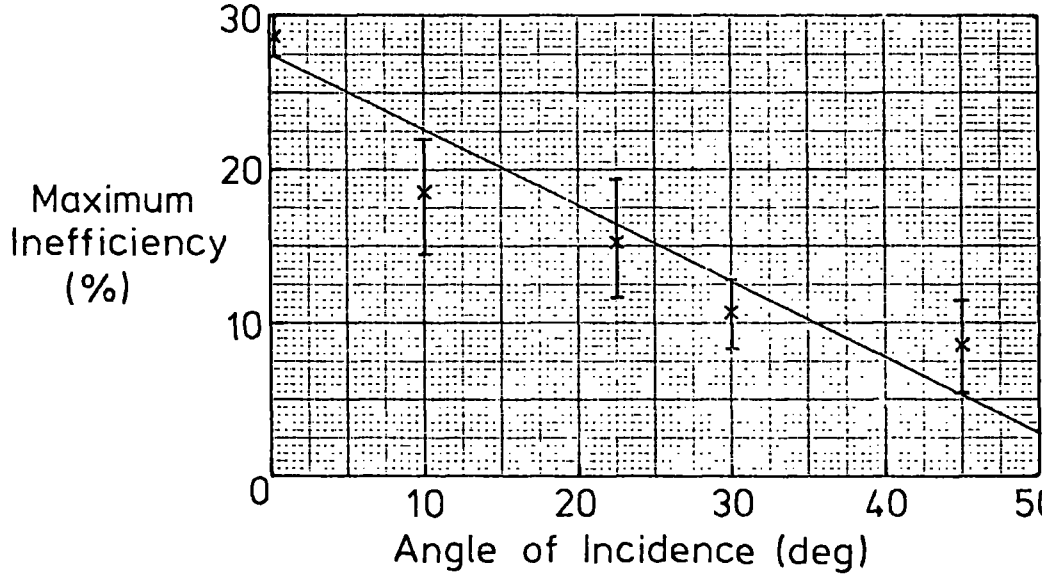

FIGURE 2.15 MAXIMUM INEFFICIENCY AGAINST ANGLE OF INCIDENCE OF PARTICLE FOR MELINEX SENSE WIRE SUPPORT

The results for the melinex and nylon cord in Table 2.1 show that the melinex produces a slightly smaller dead-space than the nylon.

However there is another factor to be taken into account in choosing the optimum support and this concerns its rigidity. While carrying out the measurements of $\oint 2.4$ on the nylon and melinex supports they were both carefully observed through a travelling microscope as the chamber critical voltage was exceeded. It was found that the nylon cord was prone to moving a few tenths of a millimetre under pressure from the sense wire plane as a whole. On the other hand the 125 μm thick strip of melinex was seen to remain absolutely stationary. Although this may seem a trivial point it is very important when large chambers are being used to locate the trajectories of particles as displacement of the wire means an incorrect location of the particle.

2.13 Wire Breakage

While testing the large Daresbury chamber it was found that sparking frequently occurred between the H.T. plane and sense wire plane. This was attributed to either particles of dust on or around the wires, or irregularities on the wires themselves, causing a local increase in field strength.

Unfortunately sparking almost always resulted in a sense wire breaking, and this required a considerable amount of time to replace.

The capacitance between the H.T. plane and sense wire plane was 2500 pF, which was increased to 3800 pF when aluminium frames, which supported the chamber, were earthed. The charging resistor for the whole H.T. plane was 1 MΩ and each sense wire was

effectively earthed through 100Ω by the amplifier. Thus when a potential of 5 kV was applied to the chamber an energy of $\frac{1}{2} CV^2$ = 0.05 joule was thereby stored and in the event of a spark this was discharged completely through one wire with a time constant of RC = 0.38 μsec. Thus considerable heating took place over a small period of time and the shock wave from the spark was presumably sufficient to break the wire.

In an attempt to overcome this the H.T. plane was split into groups of 20 wires each, each group being connected to the 1 MΩ charging resistor via 150 kΩ . This effectively split the large capacitance of the chamber into a set of smaller ones of about 250 pF, each one storing an energy of about 4 millijoules. Now in the event of a spark the 0.004 joule of the group of wires concerned was discharged with a time constant of 0.025 μsec, but the rest discharged in a time RC = 75 μsec. Thus the rate of energy loss from each group of wires was substantially retarded, giving time for the heat generated in the sense wire to be dissipated by the surrounding gas; momentary heating of the wire was therefore greatly reduced.

Following this modification it was indeed found that the frequency of sense wire breakage was greatly decreased.

2.14 Conclusion

The theoretical analysis of sense wire displacement developed by Trippe has been studied and verified experimentally.

A new type of wire support, a 3 mm wide, 125 μm thick strip of melinex has been investigated and found to produce similar size dead-spaces to the conventional method of using nylon cord, while having the added advantage of holding the sense wires far

more rigidly. A third support, PVC insulated copper wire, was found to be much less satisfactory than either of the above two supports, mainly because of the induced noise pulses on the sense wires caused by application of a negative potential to the copper wire.

CHAPTER 2: References

1. T.Trippe, Cern Internal Report, NP 69-18

2. G.Charpak, R.Bouclier, T.Bressani, J.Favier and C.Zupancic, Nucl. Instr. and Meth., 62, 262 (1968)

3. K.Kleinknecht, V.Luth, P.Steffen, F.Vannucci, H.Wahl and G.Zech, Cern Internal Report, NP 70-18

4. P.Schilly, P.Steffen, J.Steinberger, T.Trippe, F.Vannucci and H.Wahl, Nucl. Instr. and Meth. 91, 221 (1971)

5. G.Charpak, G.Fischer, A.Minten, L.Naumann, F.Sauli, G.Flugge, Ch. Gottfried and R.Tirler, Nucl. Instr. and Meth. 97, 377 (1971)

6. J.H.Dieperink, K.Kleinknecht, P.Steffen, J.Steinberger, T.Trippe and F.Vannucci, Cern Internal Report 69-28

7. K.A.Short, Int. Rep. NI-73-1, Physics Dept., Durham University

8. J.M.Breare, K.A.Short, G.C.Smith, R.A.Cunningham, International Conference on Instrumentation for High Energy Physics, Frascati, 296 (1973)

CHAPTER 3

A SHORT REVIEW OF THE MAIN CHARACTERISTICS OF TRANSITION RADIATION

3.1 Introduction

When charged particles of any energy traverse matter their usual process of energy loss is by ionization and bremsstrahlung, the former dominating below the critical energy of the medium through which the particle is passing and the latter above the critical energy. Further losses also occur in varying amounts by pair production, nuclear interactions and inverse Compton scattering.

The determination of the mass (or energy) of a particle, and the separation of one particle from another, are of major importance in many nuclear physics experiments and all forms of energy loss can be used, within certain limitations, to carry them out. However, a problem occurs at high energies because most forms of energy loss saturate, e.g. ionization loss becomes independent of particle energy since the relativistic rise increase in ionization levels off because of the density effect.

Besides energy loss measurements there are two other mass/energy determination techniques which are also difficult at high energies.

Firstly, there is Cerenkov radiation, the electromagnetic radiation emitted when a particle passes through a medium in which its velocity is greater than that of light in the medium. It is well known that the radiation is emitted along the surface of a cone, the apex of which is the instantaneous position of the moving particle and the half angle of which is given by:

$$\theta = \cos^{-1}\left[\frac{1}{\beta n}\right] \qquad 3.1$$

where β = velocity of particle and n = refractive index of the medium. It can be shown that the number of photons emitted per second per unit path length per unit frequency is a function of the square of sin θ . Therefore at relatively low energies two particles with the same energy but differing mass would induce radiation with different angles, θ , and the velocity of each could be determined by measurement of these angles. However, at higher energies where $\beta \rightarrow 1$ for both particles the Cerenkov signal would reach saturation and the process is nullified as either a velocity selector or a particle discriminator.

The other form of energy determination, that of measuring the particle's radius of curvature in a magnetic field, is also difficult at higher energies because deflections become so small that they are impossible to measure.

What is required is a phenomenon in which a relativistic particle loses energy in a quantity which is reasonably easy to detect, its magnitude varying as the energy of the particle. The only known process at present which satisfies this requirement is transition radiation, which is the flux of photons emitted when a uniformly moving charged particle passes through an interface between two media with different dielectric constants. This radiation, theoretically predicted in 1945 by Ginzburg and Frank (1), was probably first observed experimentally in 1919 by Lilienfield (2) who bombarded a metal surface with electrons of a few keV. Unfortunately this work was not immediately followed up and it was only in the late fifties and early sixties, when further experimental work was carried out (3,4), that interest in the phenomenon really began. At about the same time Garibian (5,6) produced two comprehensive theoretical treatments of the subject, the latter

forming the basis of many of the subsequent analyses of the subject.

In 1961 Alikhanyan et al. (7) put forward the first proposal for a possible method of detecting high energy charged particles with transition radiation and since then a considerable amount of work has been done, particularly by American and Russian groups, in studying the properties of this radiation. During this time the importance of transition radiation has been realised and it is now widely believed that it will prove a very useful tool for particle mass and energy determination at relativistic energies, in particular at the energies of particles which will be created in the CERN SPS. The fact to emerge from transition radiation investigations which could make this possible is that the flux of photons emitted (above optical frequencies) is proportional to $\ln \gamma$, where γ is the Lorentz factor of the particle ($\gamma=(1-\beta^2)^{-1/2}$) , and their total energy is proportional to γ . Because the magnitude of the effect is dependent upon gamma it is also useful for the separation of particles of the same energy but different mass.

3.2 Principal Characteristics

When a charged particle moves uniformly across a dielectric interface from a medium of dielectric constant and magnetic permeability ε_1 and μ_1 respectively to one of ε_2 and μ_2 respectively, a changing dipole field due to the particle and its image charge in the other medium is formed and this, according to the theory of Ginzburg and Frank, results in the emission of electromagnetic radiation, known as transition radiation.

The charged particle is assumed to lose negligible energy per unit path length when crossing the interface, and under this condition it has charge fields in each of the media which are solutions of the Maxwell equations for a point charge moving at a constant velocity $\underset{\sim}{v}$. These fields can be resolved into triple Fourier integrals in the first and second media (indices 1 and 2) which, assuming the particle moves along the x-axis from $-\infty$ to $+\infty$ and that the interface between the two media is the plane $z = 0$ through which the particle moves at $t = 0$, are given by:

$$E_{1,2}(\underset{\sim}{r},t) = \int E(\underset{\sim}{k})\, e^{i(\underset{\sim}{k}\underset{\sim}{r} - \omega t)}\, d\underset{\sim}{k} \qquad 3.2$$

where $\underset{\sim}{k}$ = propagation constant

and $\omega = \underset{\sim}{k}.\underset{\sim}{v}$

It can be readily shown that the electric and magnetic fields given by equation 3.2 do not satisfy the continuity requirements at the interface between the two media, which are that no surface charges or currents be present, i.e. the normal components of $\underset{\sim}{B}$ and $\underset{\sim}{D}$ and tangential components of $\underset{\sim}{E}$ and $\underset{\sim}{H}$ are continuous at $z = 0$. To satisfy the latter conditions it is necessary to add to the solutions given above the solutions of the homogeneous Maxwell equations with arbitrary Fourier coefficients and when these coefficients are determined by reapplying the continuity conditions at the interface the added solutions will represent the transition radiation fields. This calculation has been performed by Garibian (6) who, for simplicity, assumed one medium to be a vacuum ($\varepsilon_1 = \mu_1 = 1$). He found the Poynting vector flux of transition radiation emitted from the interface was distributed in polar angle

and frequency according to the formula:

$$\frac{dS}{d\theta\, d\omega} = \frac{2e^2\beta^2}{\pi c} \frac{\sin^3\theta \cos^2\theta}{(1-\beta^2\cos^2\theta)^2}\left[\frac{(\varepsilon-1)(1-\beta^2 \pm \beta(\varepsilon-\sin^2\theta)^{1/2})}{[\varepsilon\cos\theta+(\varepsilon-\sin^2\theta)^{1/2}][1\pm\beta(\varepsilon-\sin^2\theta)^{1/2}]}\right]^2 \qquad 3.3$$

The $\pm$ signs refer, respectively, to radiation emitted in the backward and forward direction, with respect to the particle's direction.

All calculations carried out for the purposes of this thesis to obtain predictions of expected transition radiation flux have been based on this formula. Although further theoretical analyses have appeared[8,9,10] since the publication of reference (6), equation 3.3 still remains the basic formula from which calculations can be made.

3.3 Determination of transition radiationflux

Because of its complexity equation 3.3 has been programmed in the following way. At specific values of beta dS/dw is evaluated from 0^o to 90^o in small angular ranges $d\theta$. An appropriate choice of $d\theta$ allows the function to be numerically integrated over θ, using Simpson's rule, to give the energy spectrum of photons expected from a single vacuum-medium interface. Division of this spectrum by $\hbar\omega$ gives the differential number spectrum of photons from the same interface.

It turns out that radiation emitted in the backward direction peaks mainly in the optical region, while that emitted in the forward direction, because of the small factor $\left[1-\beta\,(\varepsilon-\sin^2\theta)^{1/2}\right]$ in the denominator of equation 3.3, is in the X-ray region. As the particular technique used in this thesis is suitable only for X-rays analysis will be made only

of the X-ray component of the radiation.

The plasma frequency, ω_p , of a material is given by

$$\omega_p = \frac{4\pi\rho Z N_0 e^2}{A m} \qquad 3.4$$

where e, m = electronic charge and mass respectively

Z, A = atomic number and mass of medium respectively

ρ = density of medium

N_o = Avogadro's number

e.g. $\hbar\omega_p$ for melinex and aluminium is 23.7 eV and 32.4 eV respectively. When dealing with X-ray frequencies, ω, which are greater than the plasma frequency of the medium the propagation constant of the electromagnetic wave describing the X-ray is real and the dielectric constant of the medium may be written as:

$$\varepsilon = 1 - \omega_p^2/\omega^2 \qquad 3.5$$

As will be seen the energies of X-rays in the transition radiation flux are in the order of keV's, which is considerably greater than the plasma frequency (multiplied by $\hbar$) of either melinex or aluminium. Therefore, using expression 3.5, the photon number spectrum, dN/dE, emitted in the forward direction, has been computed from equation 3.3 for a singly charged particle traversing a vacuum-melinex and vacuum-aluminium interface for various values of particle energy (given in terms of γ) and these spectra are shown in figure 3.1. Clearly the number spectrum increases as γ increases and also the number of photons for a particle of given γ energy increases exponentially as the photon energy decreases.

It is of interest to note the dependence of the total energy emitted, and the number of photons produced, on γ :

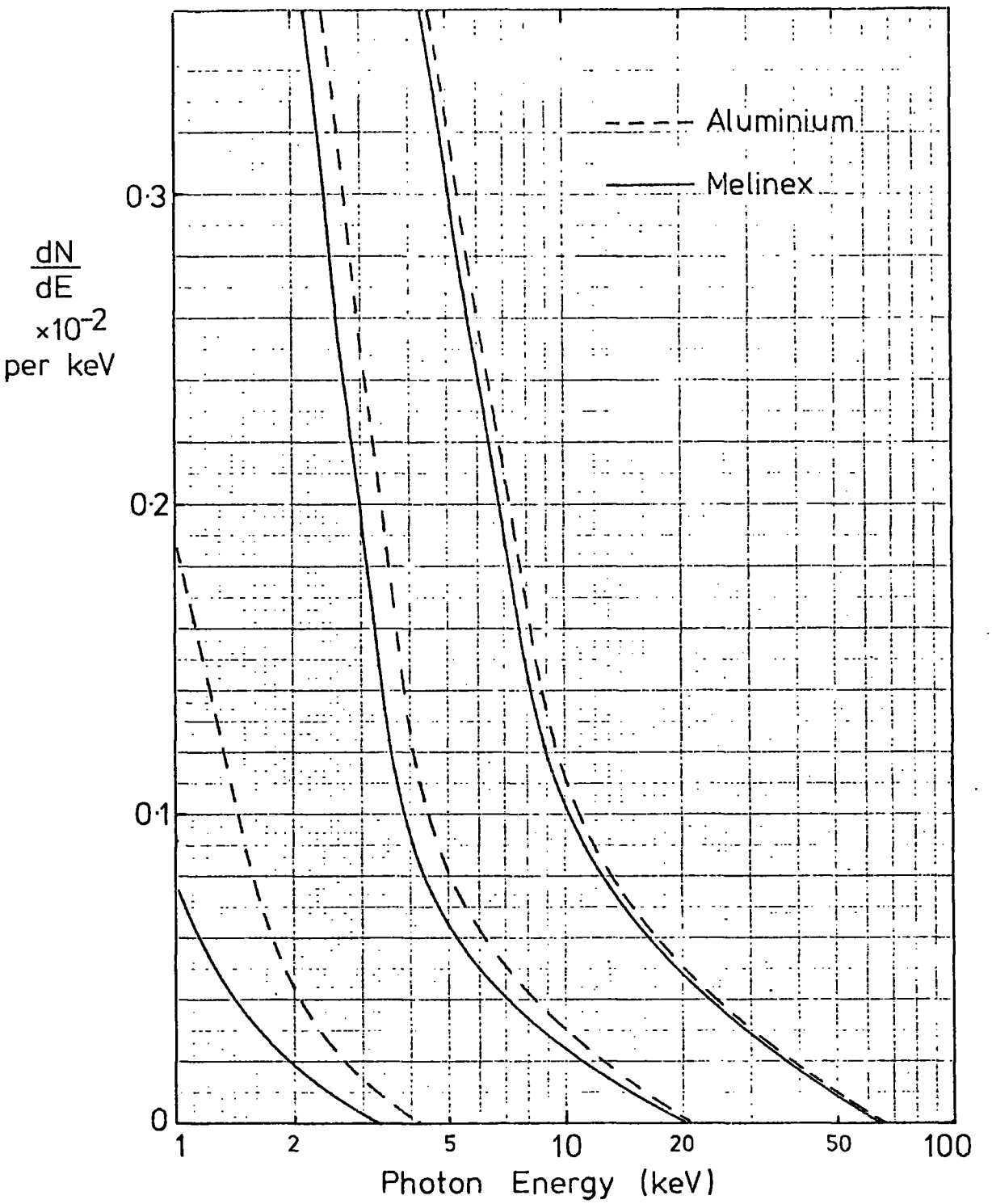

FIGURE 3.1 DIFFERENTIAL PHOTON NUMBER SPECTRA EMITTED IN FORWARD DIRECTION FROM SINGLE VACUUM-MELINEX AND VACUUM ALUMINIUM INTERFACES

a) Integrating equation 3.3 over θ and ω gives the total energy released at one interface (reference 6):

$$S = \frac{e^2 \omega_p \gamma}{3c} \qquad 3.6$$

Because the plasma frequency is proportional to density (equation 3.4) the emitted energy is also proportional to density. This explains why the flux of photons for the vacuum-aluminium interface in figure 3.1 is greater than that for the vacuum-melinex one.

b) When the number spectrum from equation 3.3 is integrated over E the total number of photons emitted is given by (reference 6):

$$N = \frac{1}{137} \frac{2}{\pi} \left[\ln\left(\frac{\gamma}{E'} \left(\frac{\omega_p^2}{2} \right)^{1/2} - \frac{1}{2} \right) \right] \qquad 3.7$$

where E' is the lower energy limit of integration.

Thus the total energy contained in the X-ray transition radiation (XTR) is linearly proportional to γ, and the number of photons proportional to the logarithm of γ. Referring briefly to optical transition radiation it has been shown, both experimentally (11) and theoretically (6), that the intensity of this radiation is proportional to the logarithm of γ, so the intensity of the X-ray component increases at a far greater rate than the optical component as γ gets larger.

All the results quoted above for the XTR created at a vacuum-medium boundary apply equally well to a medium-vacuum interface.

Figure 3.1 indicates that the flux of photons from one interface is very feeble, e.g. the number of photons emitted at

an aluminium interface between 1 and 100 keV for a particle of γ = 1000 is 0.01 and for γ = 10,000 is 0.03. To construct a practical detector of XTR it is clearly necessary to increase the photon flux and this can be achieved in one of two ways:

i) For multiply charged particles the number of emitted photons increases quadratically with the charge of the particle (6). However most particles detected in physics experiments are singly charged, though this property could prove useful for detection and identification of heavy primary cosmic rays outside the atmosphere.

ii) If a singly charged particle passes through a multitude of vacuum-media boundaries then the number of photons increases in proportion to the number of boundaries. We therefore proceed to the idea of amplifying the weak XTR signal with a 'stack' of dielectric foils. This can take the form of either a set of regularly spaced plastic or metal sheets or any form of laminated medium, such as the honeycomb-like structure of polystyrene foam. Before calculating the expected flux of photons from a stack the limitation on XTR production of the formation zone must be mentioned.

3.4 Formation Zone

In the theory developed by Garibian (6) it was shown that there exists a minimum thickness of medium (material or vacuum) through which the particle must pass before the transition radiation can be created. This finite path length is required for the polarisation field associated with XTR production to build up and is known as the formation zone. For relativistic particles it is given by:

$$Z = \frac{c}{\omega}\left[\frac{1}{\gamma^2} + \frac{1}{2}\left(\frac{\omega_p}{\omega}\right)^2\right]^{-1} \qquad 3.8$$

The importance of the formation zone lies in the fact that when a particle traverses a thickness of medium smaller than the formation zone of that medium for a particular X-ray energy then the XTR spectrum will be severely attenuated above that energy, as has been shown experimentally (12). If the X-ray energy at which this takes place is well above the peak of the expected distribution then this is not a serious loss.

Figure 3.2 shows plots of formation zone, derived from equation 3.8, as a function of X-ray energy and particle energy (γ) for melinex, aluminium and beryllium. At low photon energies the formation zone increases with photon energy. Because of the term in the denominator of equation 3.8 the formation zone then starts decreasing at around 20 keV for particles of low γ , but continues increasing up to 100 keV and more for higher γ . Thus higher energy particles require greater medium thicknesses in order to produce the full XTR signal.

The formation zone of aluminium at particular energies is less than that of melinex and beryllium because it has a higher plasma frequency, the term for which appears in the denominator of equation 3.8. For the same reason the formation zone of air is considerably larger than any of the above three elements, as shown in figure 3.2 for $\gamma = 3000$ for example, reference to which will be made later. The equivalent curve for melinex at $\gamma = 3000$ will also be used later.

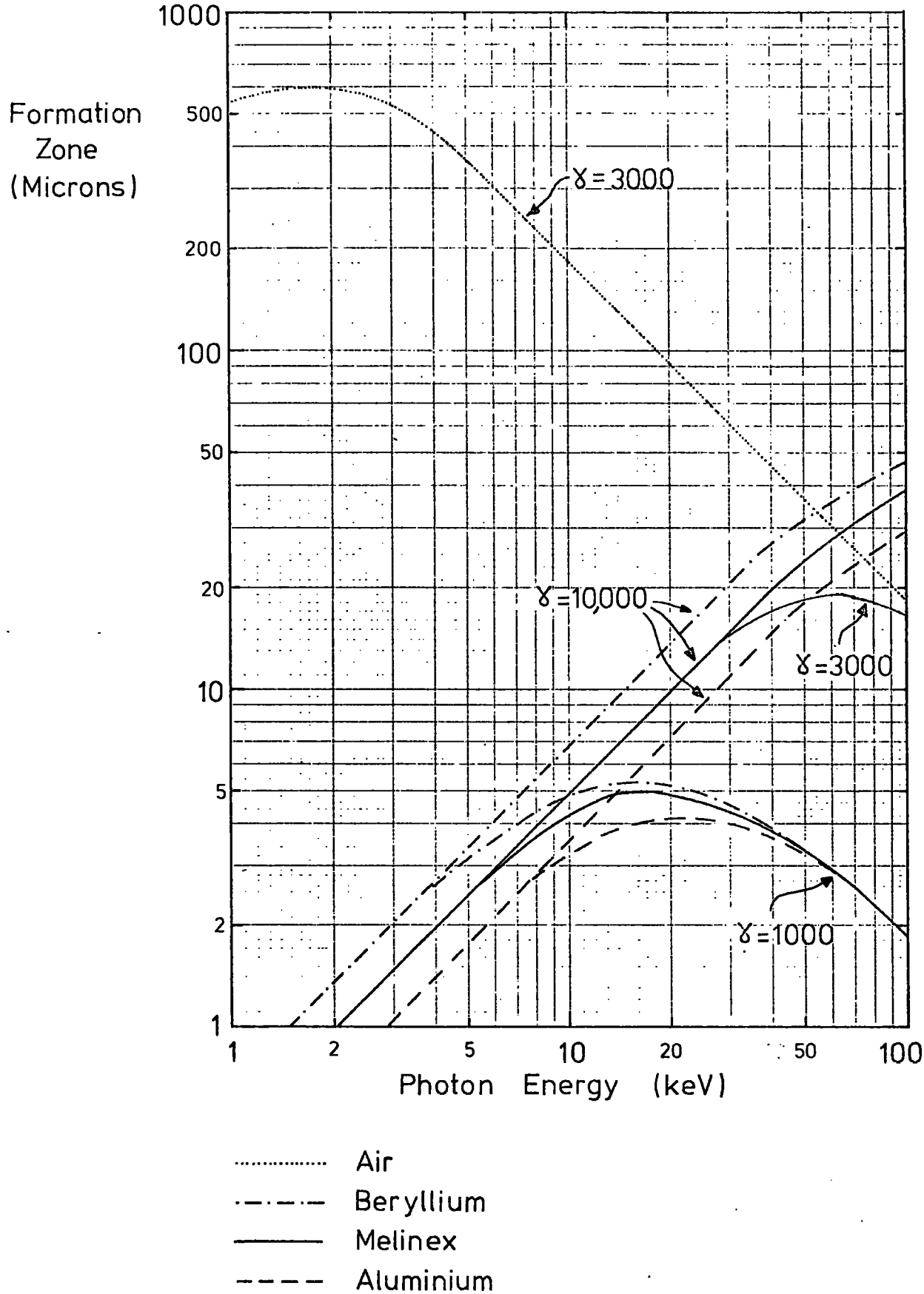

FIGURE 3.2 FORMATION ZONES OF AIR, BERYLLIUM, MELINEX AND ALUMINIUM AGAINST PHOTON ENERGY

3.5 Angular Distribution

Evaluation of equation 3.3 at discrete values of θ for photon emission in the forward direction gives the distribution of transition radiation with respect to polar angle and figure 3.3 (a,b,c) shows plots of this distribution for three different values of γ at a photon energy of 10 keV. The same distributions for lower and higher energy photons peak at slightly higher and lower angles respectively and are also a little broader and narrower respectively, but these effects are very minimal.

It is clear that the radiation is highly collimated in the direction of the particle; in fact a useful approximation is that the peak of the radiation occurs at an angle of $1/\gamma$ to the particle direction, and this is indicated on the diagrams.

Thus the radiation from a 5 GeV electron, say, (γ = 10,000) peaks at $1.5\ 10^{-4}$ radians, so over a distance of 10 metres from its point of production it will have spread out to cover an area of about 0.7 cm^2. Hence the radiation is very localised with respect to the particle's trajectory and unless it is possible to deflect the particle away from its initial direction the XTR must be detected in the presence of the particle ionization. This, coupled with the extremely low flux of radiation, represents the major problem in XTR detection and puts severe limitations on the methods by which it can be carried out.

3.6 Amplification of an XTR stack

A charged particle of given Lorentz factor, γ , traversing an XTR stack composed of 'n' regularly spaced dielectric foils each of thickness 't', will produce a spectrum

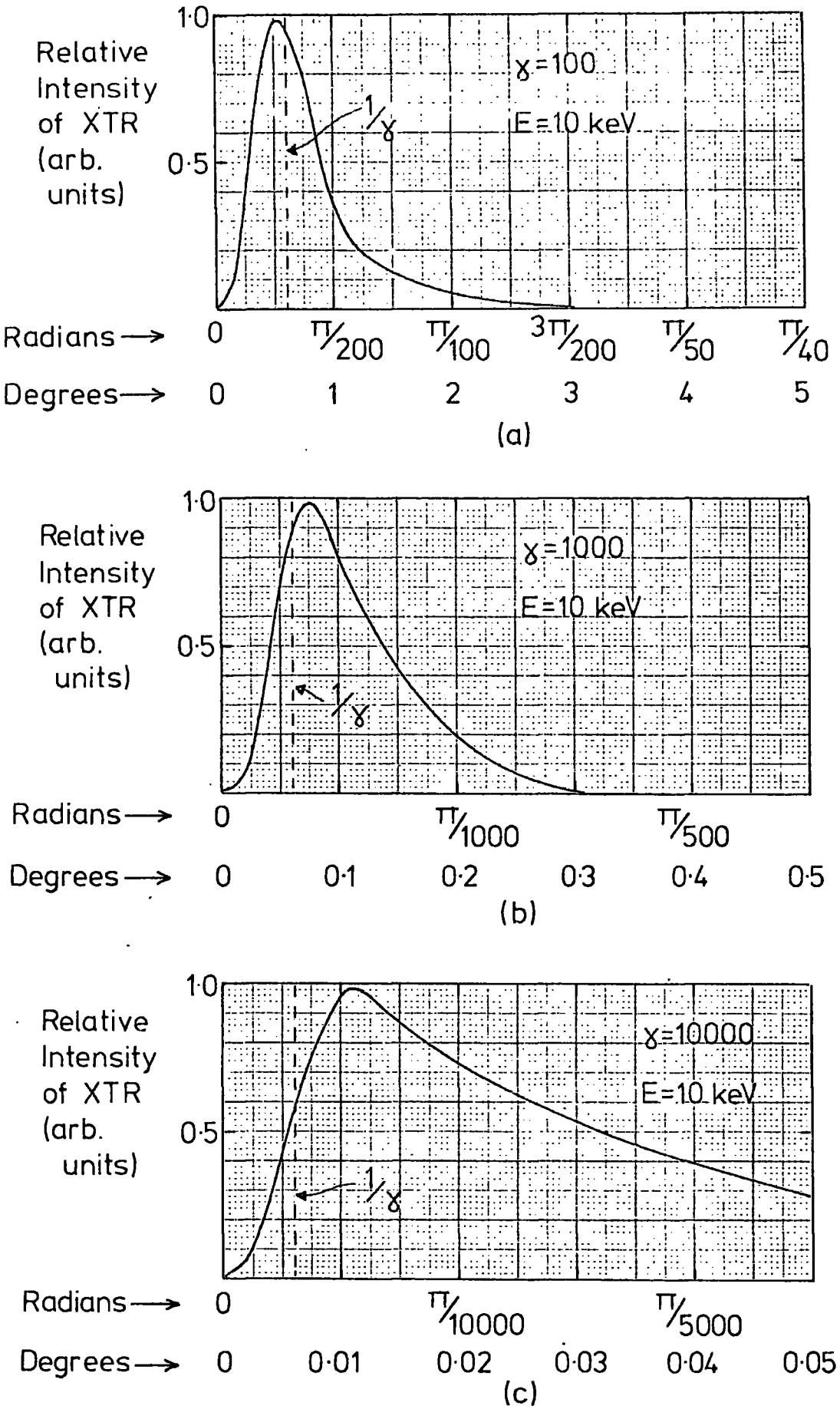

FIGURE 3.3 INTENSITY OF X-RAY TRANSITION RADIATION AGAINST POLAR ANGLE

of photons, $^{dN}/_{dE}$, at every interface. However, because of absorption in each foil the flux emanating from the last foil of the stack will not be '2n' times $^{dN}/_{dE}$, but only a certain fraction of this. By taking into account the progressive X-ray absorption as the particle penetrates the stack it can be shown (Appendix II) that the differential number spectrum of photons emerging from the stack is:

$$\frac{dN_n}{dE} = \frac{dN}{dE}\,\frac{2}{\mu t}\,(1 - e^{-n\mu t}) \qquad 3.9$$

where $\frac{dN}{dE}$, the XTR flux from one interface, is obtained from equation 3.3 in the manner described in § 3.3 and μ is the linear absorption coefficient of foil dielectric. Because the absorption of X-rays depends upon the mass of the absorber this coefficient is usually written as $\mu_m = \mu/\rho$, the mass absorption coefficient, so that equation 3.9 becomes

$$\frac{dN_n}{dE} = \frac{dN}{dE}\,\frac{2}{\mu_m \rho t}\,(1 - e^{-\mu_m \rho n t}) \qquad 3.10$$

Not surprisingly the largest signal is obtained when 'n' tends to infinity; this is the case of the assymptotic stack (13), which has a gain of $^{2}/_{\mu_m \rho t}$ times the flux from a single interface.

The main point to note from equation 3.10 is the absorption coefficient, μ_m $(= \mu_m(E))$, in the denominator Since μ_m decreases rapidly with increasing energy (figure 3.4 shows $\mu_m(E)$ for the three elements mentioned previously: beryllium, melinex and aluminium) the output spectrum from a

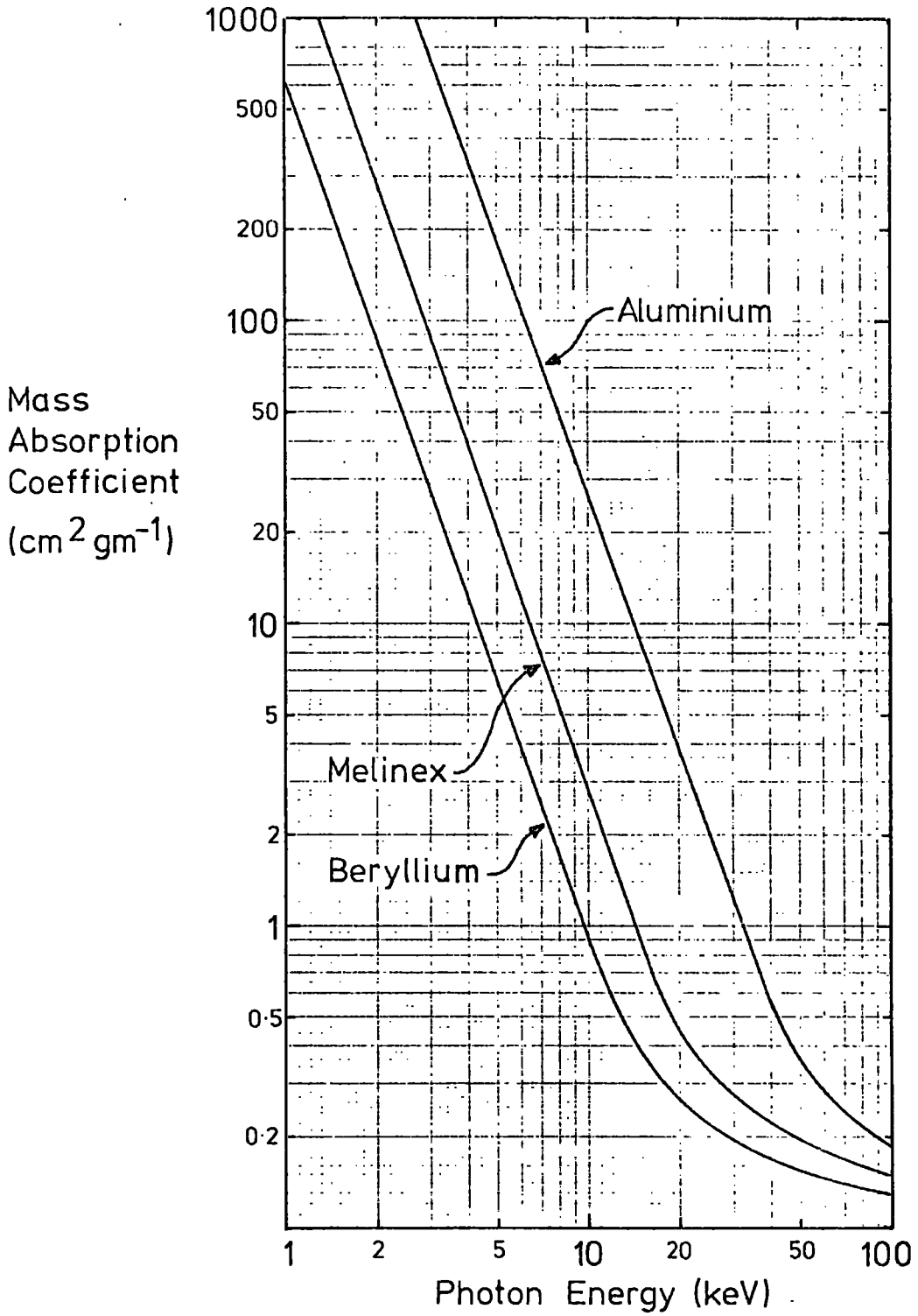

FIGURE 3.4 MASS ABSORPTION COEFFICIENTS OF BERYLLIUM, MELINEX AND ALUMINIUM

stack should show a marked cut-off of low energy photons. In addition $\mu_m(E)$ is proportional to Z^4, where Z is the atomic number of the material, so this would suggest that loss of photon flux by absorption will become much less severe the lower the Z the element of the stack. Although equation 3.6 predicts a greater release of energy for a more dense material the magnitude of the XTR flux from a stack is completely dominated by the quartic dependence of $\mu_m(E)$ on Z.

3.7 XTR output from a periodic stack

Equation 3.10 can now be used to ascertain the shape and size of the expected XTR spectrum from a stack of regularly spaced foils, bearing in mind that this equation does not take into account the formation zone.

The two most common foil materials used by previous workers are melinex and aluminium, primarily because they are very cheap and easy to obtain in thin sheet form. However, as will be seen later in this section, low Z materials are far better XTR producers than high Z and a recent proposal by Harris et al (14) to carry out further work on transition radiation at the NAL in America will, if accepted, lead to tests with beryllium foils. Thus for comparison purposes we will consider monoenergetic particles passing through a stack of 1000 beryllium, melinex and aluminium foils, the thickness of the foils being that of the formation zone of the respective material given in figure 3.2.

Consider first a particle with $\gamma = 1000$. The respective maximum formation zones of beryllium, melinex and aluminium are 5, 5 and 4 μm . The differential number spectrum of photons (from equation 3.10) for these particular thicknesses is shown in figure 3.5. Three important points emerge from these curves:

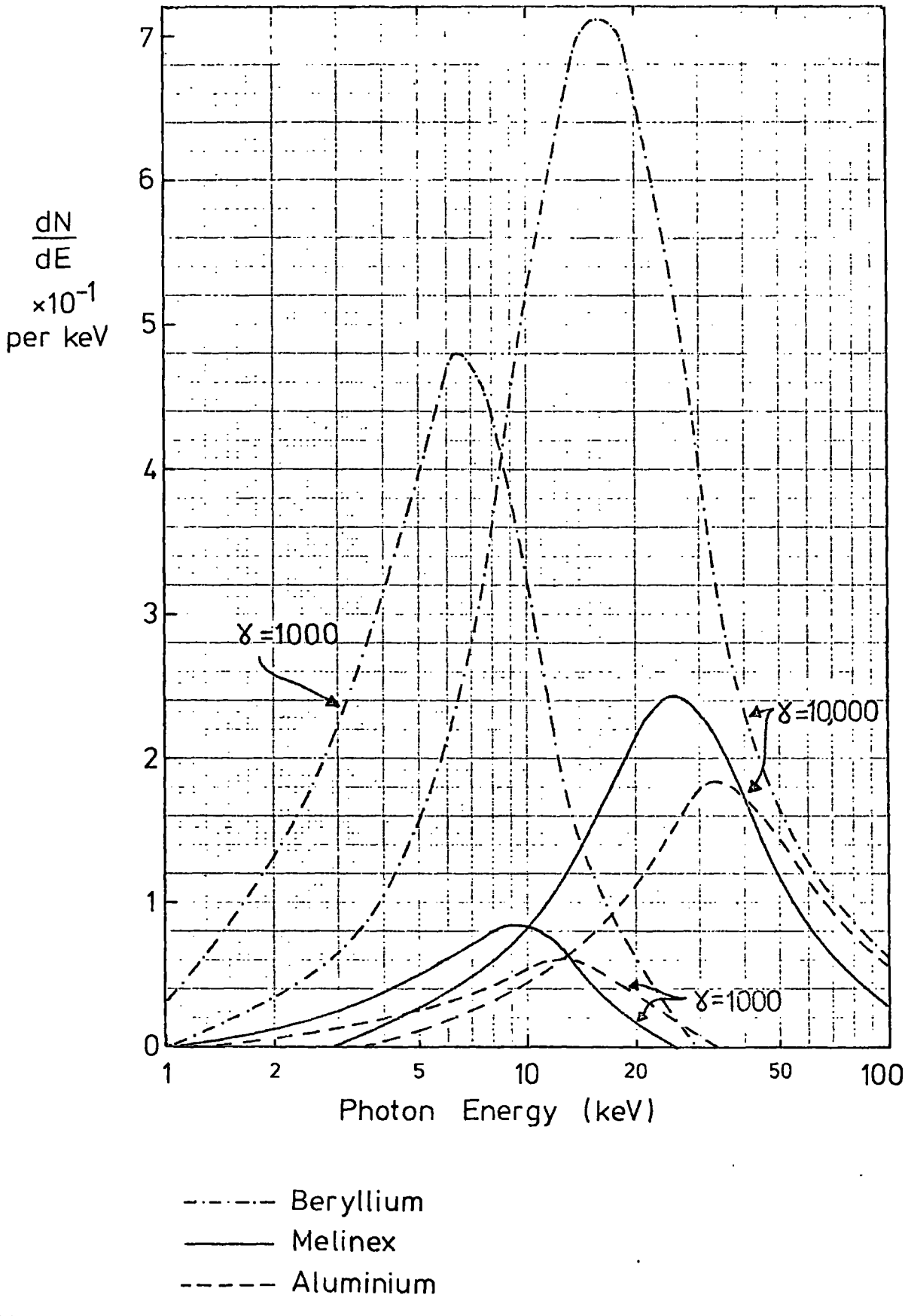

FIGURE 3.5 DIFFERENTIAL TRANSITION RADIATION SPECTRA FROM 1000 FOIL STACKS OF BERYLLIUM, MELINEX AND ALUMINIUM FOR PARTICLES WITH γ = 1,000 AND γ = 10,000

a) The XTR spectrum shows a marked cut-off at very low energies due to absorption in the foils, with a result that it has a peak at soft X-ray frequencies.

b) The lower the Z of the stack the lower in energy is the peak of the distribution - this results from the greater absorbing power of the higher Z elements.

c) The stack with lower Z produces far more photons than one with a higher Z; again this is due to the photon absorption dependence on Z^4.

Also in figure 3.5 are the same set of curves for a particle with γ = 10,000 and, because of the higher gamma, the energy range of the emitted photons has increased considerably. In fact the spectrum extends well up to 100 keV and consequently the material formation zones used are those for 100 keV, i.e. 46, 40 and 30 μm respectively. The major point to emerge from these curves is that as γ increases the mean energy also increases, and there is also a large increase in the number of emitted photons.

Similar curves to those in figure 3.5 can be obtained for stacks with any number of foils. The basic shape remains the same and the mean energy of each distribution increases slightly as the number of foils increases. Integrating each curve over energy gives the energy content of the XTR flux and figures 3.6 and 3.7 show the variation of this energy with the number of foils for particles of γ = 1000 and 10,000: two sets of curves are shown in each figure, one for the soft X-ray component (1 $\rightarrow$ 20 keV) and one for the hard X-ray component (20 $\rightarrow$ 100 keV). The reason for this division into two energy ranges is that soft X-rays have a much higher absorption coefficient in the detector gas than hard X-rays, as will become evident in Chapter 5.

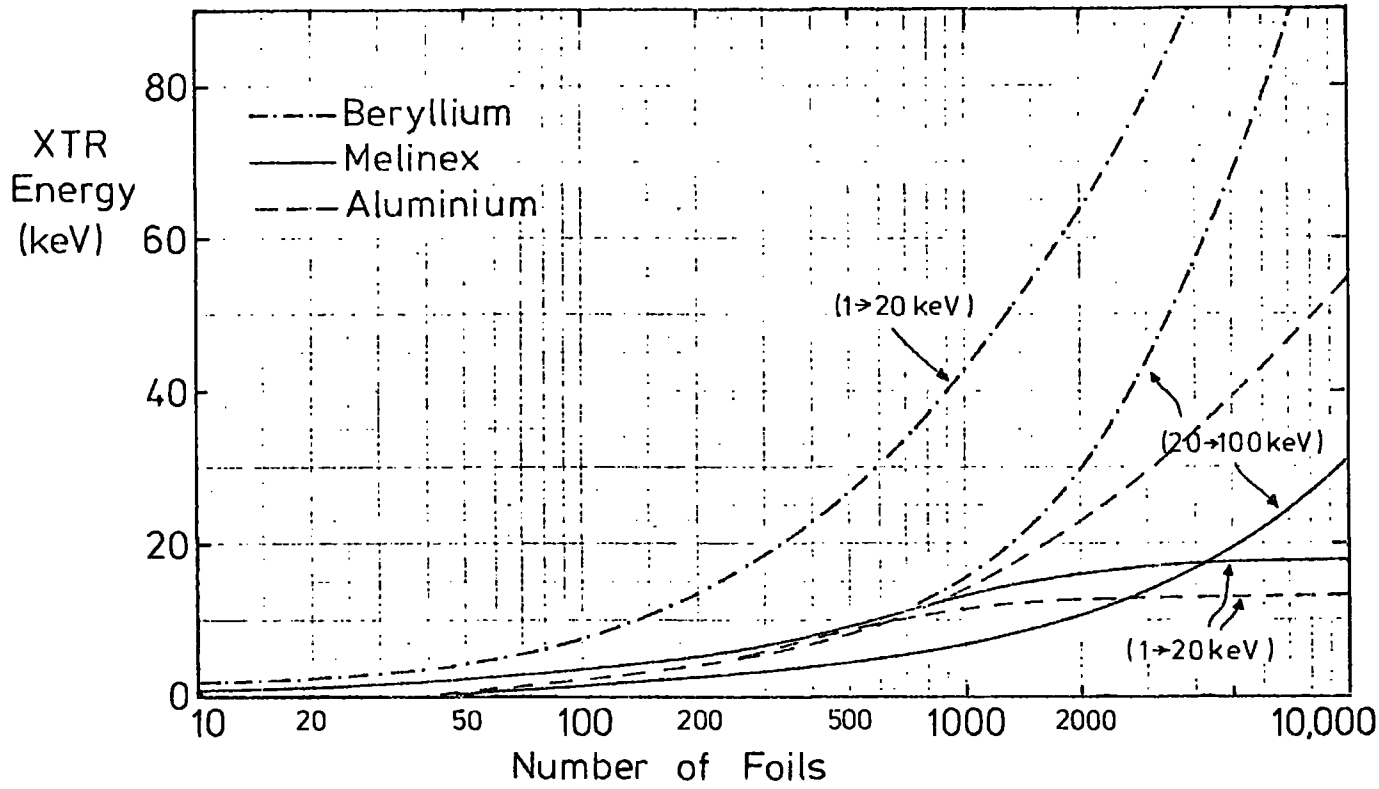

FIGURE 3.6 TOTAL X-RAY TRANSITION RADIATION ENERGY FROM PARTICLE WITH γ = 1,000 AGAINST NUMBER OF FOILS TRAVERSED

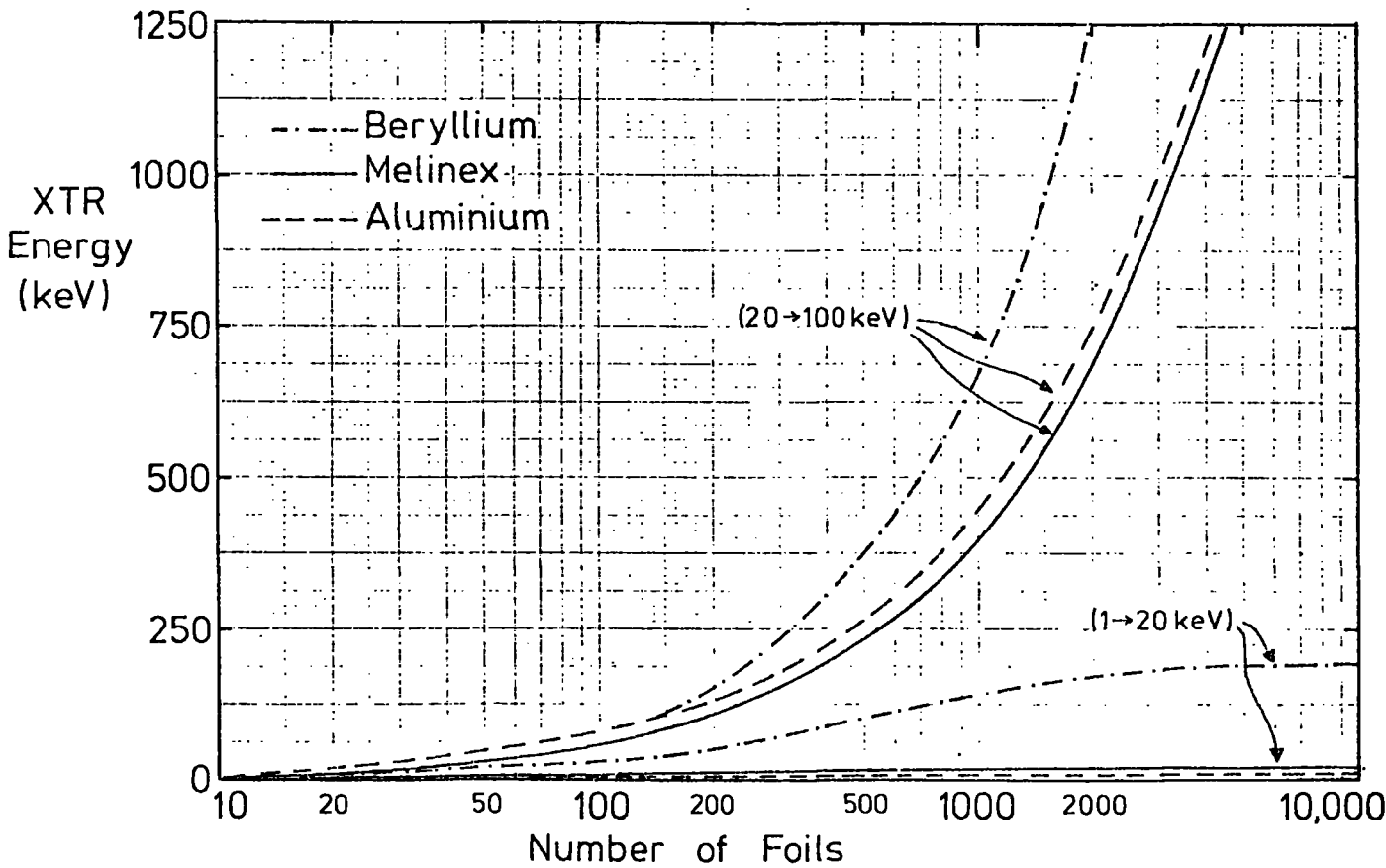

FIGURE 3.7 TOTAL X-RAY TRANSITION RADIATION ENERGY FROM PARTICLE WITH γ = 10,000 AGAINST NUMBER OF FOILS TRAVERSED

It can be seen that, whereas a particle passing through a melinex and aluminium stack will cause the emission of roughly equal quantities of energy, the same particle passing through an equivalent beryllium stack results in a much greater emission of energy than either of these two. This is purely because the low Z of beryllium results in a small loss of X-ray signal through absorption in the foils and clearly illustrates the advantage of using a material with as low a Z as possible; in fact Bateman (13) has proposed the idea of a deuterium foam stack, which creates even more signal than the equivalent beryllium stack. The melinex stack is just better than the aluminium one because of its slightly smaller absorption coefficient over aluminium.

Another important point to emerge from these two figures is that for small γ the majority of the XTR signal is contained in soft X-rays (for stacks of 1000 foils and less) while the situation is reversed at higher gamma. In addition the soft X-ray component saturates at about 1000 foils, so there is no gain in the soft X-ray component of the signal from low γ particles by using larger XTR stacks, a point which is important for both the XTR detection experiments to be described.

The region beyond 1000 foils in figures 3.6 and 3.7 is really only of academic interest as such stacks represent a huge practical undertaking and, in fact, the maximum known size of radiator that has been used to date is one with 1000 foils (15). However the curves do show that there would be an enormous signal in the hard X-ray component.

3.8 XTR output from non-periodic stack

The presence of a strictly periodic medium is not the singlecondition for production of transition radiation; any medium, such as polystyrene or polyurethane foam, providing a multitude of air-material interfaces, will suffice. However the calculation of the expected output is extremely complicated because of the random distribution of the inhomogeneities and variation in pore and wall sizes. According to Garibian (6), the XTR intensity is almost independent of the angle at which a particle enters an interface, i.e. all the foregoing analysis of periodic stacks is true, irrespective of particle incident angle, to a first order.

In part of the transition radiation experiment to be described in Chapter 6 the radiator was a block of polyurethane foam and for the purposes of calculating the expected output its average pore and wall thickness were measured with a travelling microscope and the output was then assumed to be half that of a regular plastic stack with an appropriate number of foils equal in thickness to the foam wall thickness. This is an approximation which is shown experimentally in Chapter 5 to be reasonably valid.

3.9 Conclusion

The main point of this chapter has been to outline the important aspects and characteristics of transition radiation so that an appreciation can be made of the detection techniques, to be described in the following chapter, used in this particular investigation and by other workers.

From the original transition radiation theory developed by Garibian the photon number spectrum created by a charged particle traversing a vacuum-medium interface has been calculated, from which

the photon spectrum from a stack of foils has been derived. The radiation in the forward direction has been shown to consist mainly of X-rays which are very highly collimated with respect to the particle's direction, their production depending upon the foil thickness being at least as thick as the 'formation zone' of the particular medium. Analysis has concentrated on three main radiator materials: melinex and aluminium because of their previous use in this field, and beryllium because of its possible use in the future.

The most important point to emerge, as far as the work to be described is concerned, is that the XTR spectrum from low γ particles peaks at soft X-ray frequencies.

CHAPTER 3: References

1. V.L. Ginzburg and I.M Frank, J.E.T.P. 16, 15 (1946)

2. J.E. Lilienfield, Physik Zeit 20, 280 (1919)

3. P. Goldsmith and J.V. Jelley, Phil. Mag. 4, 836 (1959)

4. H. Boersch, C. Radeloff and G. Sauerbrey, Phys. Rev. Lett. 7, 52 (1961)

5. G.M. Garibian, Sov. Phys. J.E.T.P. 6, 1079 (1958)

6. G.M. Garibian, Sov. Phys. J.E.T.P. 10, 372 (1960)

7. A.I. Alikhanyan, Sov. Phys. J.E.T.P. 14, 1421 (1962)

8. G.M. Garibian, Yerevan Physical Institute Report EØM-TØ-13 (70)

9. J.V. Lepore and R.J. Riddell Jr., Lawrence Berkeley Radiation Laboratory Report (1972)

10. G.M. Garibian, Yerevan Physical Institute Report (1973)

11. S. Prunster, C.L. Wang, L.C.L. Yuan, J. Oostens, Phys. Lett. 28B, No. 1, 47 (1968)

12. L.C.L. Yuan, C.L. Wang, H. Uto and S. Prunster, Phys. Rev. Letters 25 No. 21, 1513 (1970)

13. J.E.Bateman, Nuc. Inst. and Meth. 103, 565 (1972)

14. F. Harris, T. Katsura, S. Parker, V. Peterson and V. Stenger (University of Hawii), R. Ellsworth, G.B. Yodh (University of Maryland), S. Pruss (National Accelerator Laboratory) National Accelerator Laboratory Proposal (1973)

15. A. I. Alikhanian, S. A. Kankanian, A. G. Oganessian, A. G. Tamanian, Yerevan Physical Institute Report EØM-M9-I8(72)

CHAPTER 4

PULSE SHAPE DISCRIMINATION WITH MULTI-WIRE PROPORTIONAL CHAMBERS

4.1 Introduction

The XTR spectra derived in the last chapter show clearly that for particles with small γ the main part of the radiation is contained in soft X-rays. In order to make use of the XTR signal, either for particle energy determination or for particle separation, it obviously has to be detected and analysed in some manner, but because the XTR signal is highly collimated with respect to the incident charged particle its detection relies upon one of two alternatives:

a) The transition radiation detector must be placed a considerable distance away from the stack in order that the incident particle can be deflected from its original direction by a magnetic field and hence leave no ionization of its own in the detector. This procedure is quite adequate for relatively low energy particles but becomes more and more difficult as the magnetic rigidity of the particle increases.

b) The second method is to detect both the XTR and particle ionization together and, if possible, to separate them. This necessitates the use of a detector in which the magnitude of the ionization deposited by the particle is of the order of, or less than, the expected detected XTR signal.

The method adopted in this work is that of (b), using a MWPC and a new pulse shape discrimination technique. Before describing this in detail a brief review of the various techniques used hitherto will be carried out so that a suitable comparison can be made between them and the technique in this work.

4.2 Previous Methods of detecting X-ray Transition Radiation

4.2.1 Method (a)

The type of detector usually employed in this method is a small area solid-state one, either a Ge(Li) or Si(Li) detector or a Na I crystal. If we take, for example, the silicon detector, with a density of 2.35 gm cm^{-3}, then a minimum ionizing particle would lose about 1 MeV in a 1 mm thick crystal, which would completely swamp the 10 keV or so energy content of the XTR signal, so it is vital to prevent any particle ionization loss in the detector. Thus the charged particles are detected by two scintillators before traversing the XTR stack and then deflected away from the detector into a third scintillator of the beam defining telescope. The detector is placed in line with the original beam direction so that the transition radiation is directed towards it. A typical arrangement is shown in figure 4.1.

Because the detector has to be placed several metres away from the stack the space between itself and the stack must be taken by a vacuum tube (or, failing this, a helium bag) to counter loss of X-rays by absorption which would take place if there was just an air-gap. The crystal has a very high X-ray absorption coefficient up to 100 keV so very little of the XTR spectrum is lost.

Apart from the drawback of having to use a magnetic field the small area of all solid-state detectors renders this particular method of little use in using transition radiation as an experimental technique. However, it does provide a relatively easy means of testing the validity of transition radiation theory, e.g. in (1) it is shown that the experimental variation of the angular distribution and total radiated energy with gamma, is in close agreement with that predicted by the theory of Garibian outlined in the preceding chapter.

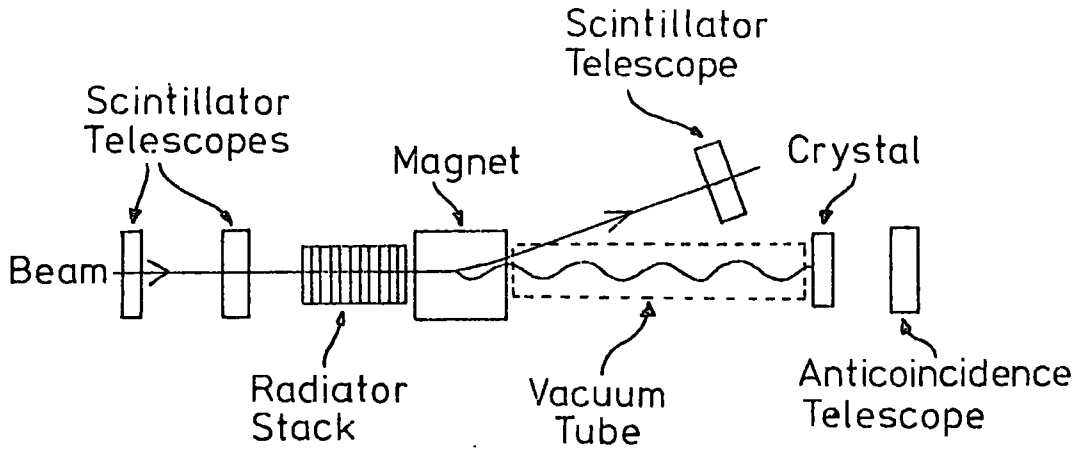

FIGURE 4.1 TRANSITION RADIATION DETECTION WITH A NaI CRYSTAL

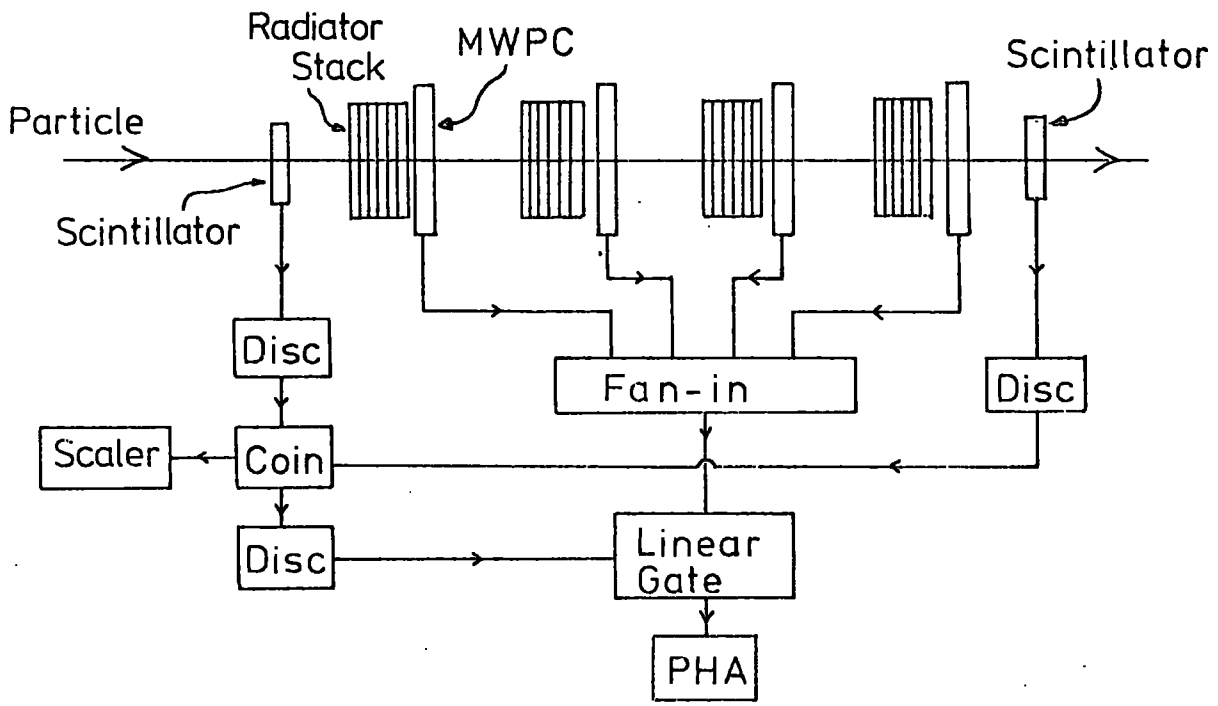

FIGURE 4.2 TRANSITION RADIATION DETECTION WITH A PROPORTIONAL CHAMBER/RADIATOR STACK CONFIGURATION

4.2.2 Method (b)

To ensure the magnitude of the particle ionization is of the order of the XTR signal restricts one almost exclusively to the use of gaseous detectors. The only two which have had any success in this field are the streamer chamber and MWPC.

The streamer chamber application has been investigated by a Russian group (2,3) using a chamber filled with a standard neon-helium mixture to which had been added 10% xenon to increase the X-ray absorption coefficient.

In their first experiment (2) three scintillators constituted the beam telescope, in between which were the XTR stack and streamer chamber. For most of the measurements the stack consisted of 500 or 1000 polyethylene films. Each trigger corresponded to particles traversing, consecutively, the stack and chamber, and photographs of typical events showed the tracks of the primary particle plus one or more short range tracks almost perpendicular to, and originating from, the main one. Although some were inevitably caused by knock-on electrons (delta-rays), measurements with background radiators proved the majority were due to photoelectrons created by the absorption of X-rays.

In a more recent experiment (3) the same group have incorporated method (a) into their technique and deflected the primary particle beam away from its original direction such that identification of photoelectrons is far easier. By counting the number of them created by electrons of different energies they were able to confirm the fact that the XTR energy content increases linearly with the gamma of the particle. From the same results they were also able to predict that pions and protons at energies above 1000 GeV could be separated with 86% efficiency.

The most commonly used detector to date, however, is the MWPC. A typical argon filled chamber represents a thickness of about 2 mgm cm^{-2} so the particle ionization loss is only about 4 keV, which is less than the energy content of the XTR expected from a highly ultrarelativistic particle passing through a typical stack.

Two independent experiments, one by Yuan et al. (4) in 1970 and the other by Harris et al. (5) in 1971, using very similar arrangements, proved the feasibility of using this detector for XTR detection. Basically they used a chamber-radiator sandwich configuration as shown in figure 4.2, in which the number of sandwich elements could be varied; the charged particle was detected by scintillator telescopes at the front and back of the array and the charge collected in each chamber integrated, the outputs of all chambers being added. Thus the resulting pulse height was proportional to the ionization deposited in all the chambers.

The spectrum of pulse heights obtained from the chambers for a monoenergetic beam of particles without the radiators in position was essentially the Landau distribution of the particle ionization loss, as in figure 4.3. The dotted line in this figure is the pulse height distribution for the same monoenergetic particles with the radiators in front of the chambers (normalised to the same number of events as the first curve) and it can be seen that there are far more events of higher energy loss with the radiators in position than without. This is attributed to ionization created by XTR.

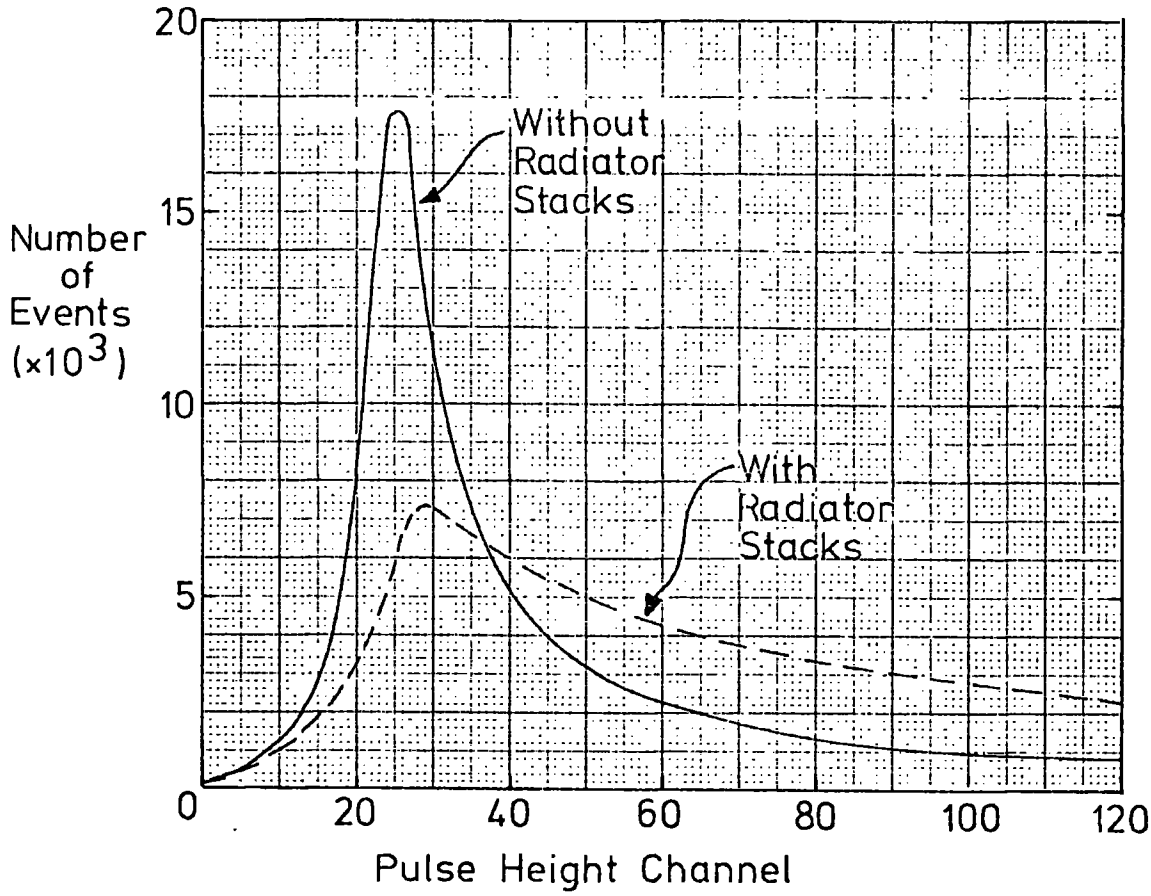

FIGURE 4.3 PULSE HEIGHT DISTRIBUTIONS FROM CHAMBERS IN FIGURE 4.2

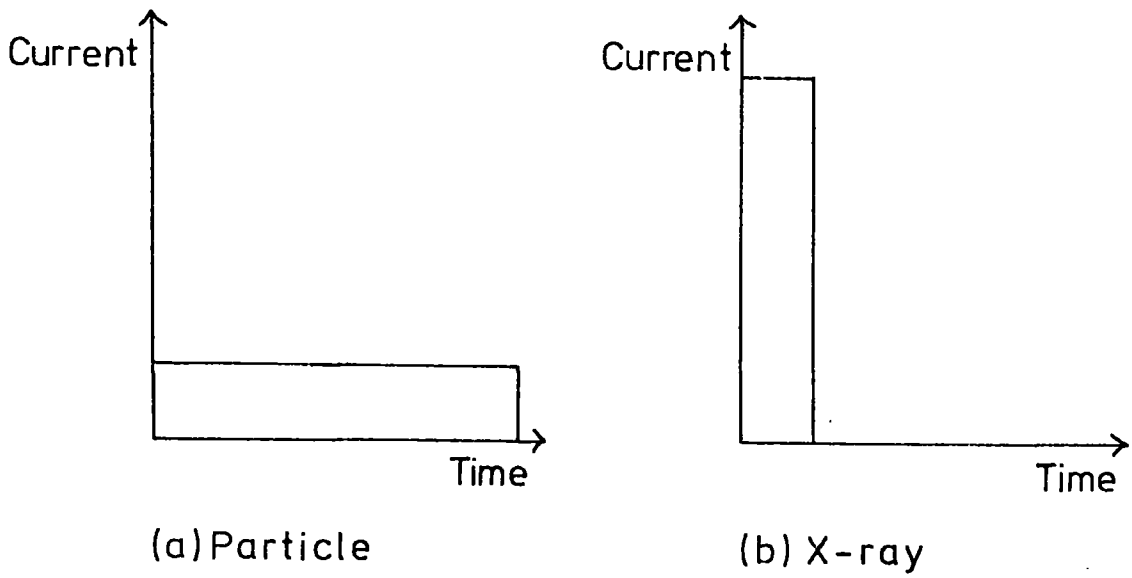

FIGURE 4.4 IDEAL PARTICLE AND X-RAY PULSES FROM PROPORTIONAL CHAMBER

4.3 Technique developed for this work

4.3.1 Introduction

A novel pulse shape discrimination process has been developed to facilitate separation of the particle signal from the XTR signal, and is based on the difference in the spatial distribution of the ionization deposited by the two ionizing radiations. The basis of the technique and the manner in which it is put into practice will be described now, while the main set of results obtained by it will be left for the next chapters.

4.3.2 Physical Basis

It was stated in §4.2.2 that a minimum ionizing particle, traversing normally a typical MWPC, loses about 4 keV in the chamber. For normal high voltages and wire spacing the drift velocity of electrons in MWPC's is about 4 cm./μsec (Chapter 1) so the electrons, constituting half the ion pairs formed by the passage of the particle, will be collected within a time of about 250 nsec. The arrival of each electron at the sense wire results in an avalanche toward the wire and the charge so created, when the wire is connected to an integrating amplifier of input impedance R_i, builds up on the capacitance of the wire to ground, C_i, and decays with the characteristic time constant, $R_i C_i$, of the system, typically a microsecond or so. The pulse height is proportional to the quantity of charge collected.

If, however, the sense wire is connected to a current amplifier with a very low input impedance, such that $R_i C_i \ll 250$ nsec, no integration of the charge will occur and the output of the amplifier will represent the current from the chamber with respect to time. The net result is that the basic high impact parameter ionization produced by the charged particle gives a low level,

approximately constant, current distribution throughout the collection period, which is ideally represented by Figure 4.4(a). Now:

$$i = \frac{dq}{dt}$$

$$\int i\,dt = \int \frac{dq}{dt} \cdot dt = q$$

Thus the area under the curve is proportional to the quantity of charge collected.

An X-ray on the other hand, if completely absorbed by the photoelectric effect, will give rise to a photoelectron which, for soft X-rays, has a very short range compared to the width of the chamber. Figure 4.5 shows electron ranges in three proportional chamber gases, argon, krypton and xenon. These have been obtained from the data of references 6,7,8,9,10 of ranges in air, which are converted to ranges in the above three gases by multiplying by the ratio of the density of air to that of the gas in question.

The distinction should be made here of the difference between range and path length. The path length is the total distance travelled by the electron, as it is scattered by the gas molecules, in coming to rest, whereas the range, purely an experimental concept, can be taken as the thickness of an absorber which the particle can penetrate, though several definitions do exist. Therefore, because of the itinerant path of the electron, the range is always less than path length.

During thermalisation the photoelectron produces a very localised bunch of ionization because of its short range and this drifts towards the sense wire which, in current mode, produces an extremely large current for the short time taken to collect all the charge. In comparison with the particle pulse the

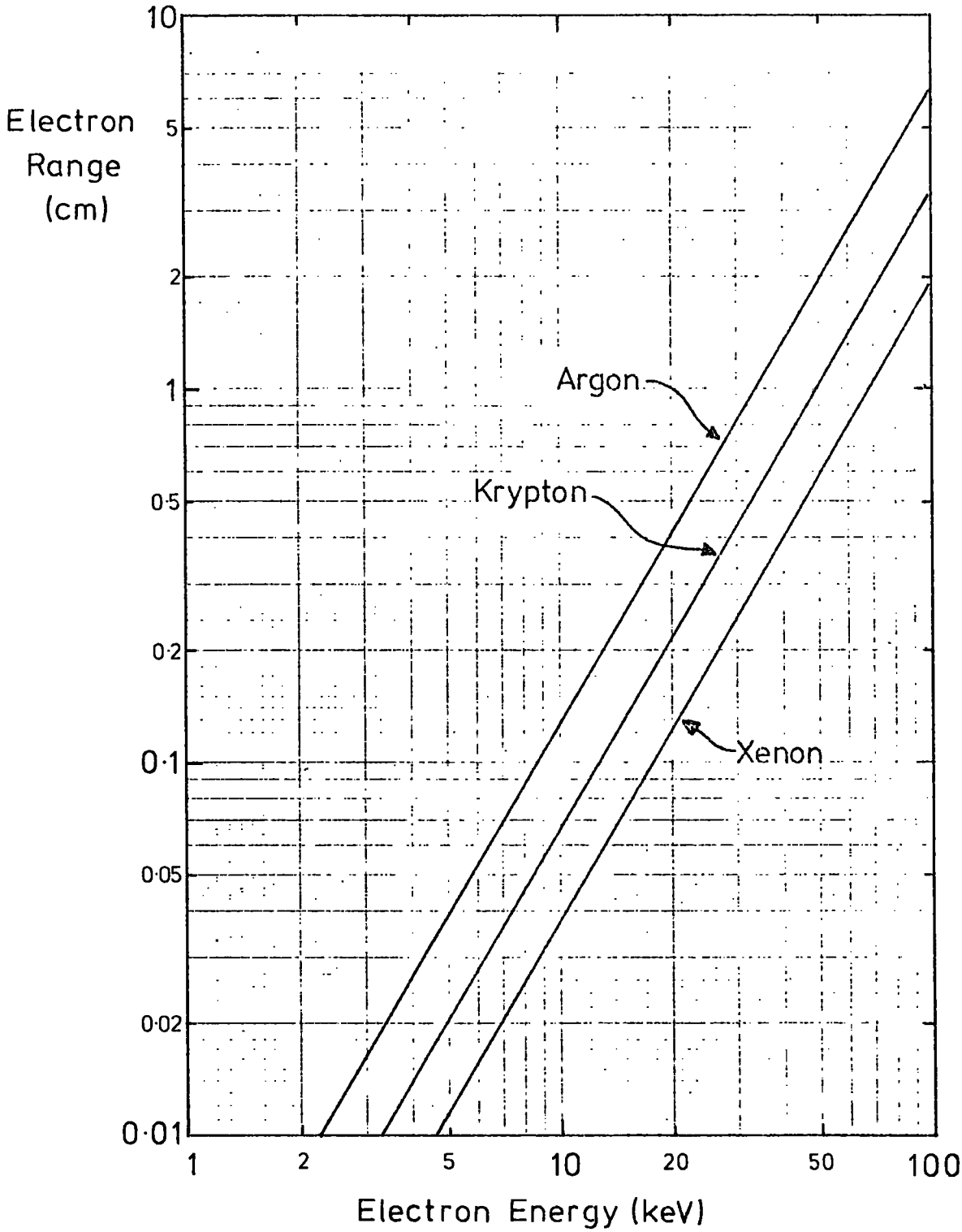

FIGURE 4.5 ELECTRON RANGES IN ARGON, KRYPTON AND XENON

ideal shape of a low energy X-ray pulse depositing a charge 'q' equal in magnitude to that deposited by the particle would be as in Figure 4.4(b).

Thus the net result is that an X-ray current pulse is far greater in magnitude than the equivalent particle pulse because it has a similar area but is an order of magnitude narrower in time. The idea of the new technique is therefore to set a threshold on the output of the current amplifier to exclude the particle pulse yet allow through all the X-ray pulse.

4.3.3 Preliminary investigation

To investigate the efficiency of the above technique a few simple tests were carried out with the following apparatus.

A MWPC, exactly identical in construction to that of chambers A and C in Chapter 2, was set-up with a scintillator telescope beneath it and a radioactive source holder above. The four middle sense wires of the chamber were connected to a current amplifier whose output was monitored by an oscilloscope: the rest of the sense wires were earthed. The oscilloscope could be triggered directly, or externally from the telescope, as shown in Figure 4.6. The additional circuitry in this figure was for a later experiment.

The current amplifier circuit is shown in Figure 4.7 and had an input impedance of less than 10 Ω and a gain given by R_1/R_2, where R_1 and R_2 are given in the circuit diagram, i.e. about 50 in this instance. The chamber was flushed with a mixture of argon and isobutane (70/30 by volume) and operated at 4.2 kV.

With an RCL bridge the capacitance of the sense wires to ground was measured to be about 20 pF which, coupled with the input impedance of the amplifier, gave an RC time of 0.2 nsec, which well satisfies the condition laid down in the last section.

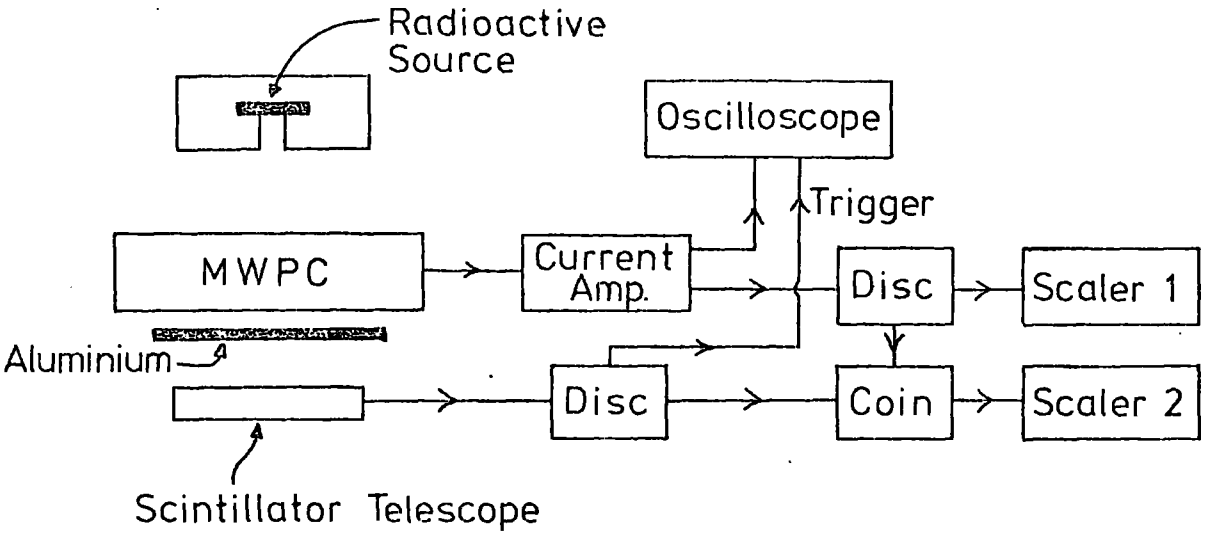

FIGURE 4.6 EXPERIMENTAL ARRANGEMENT FOR INVESTIGATION OF PULSE SHAPES

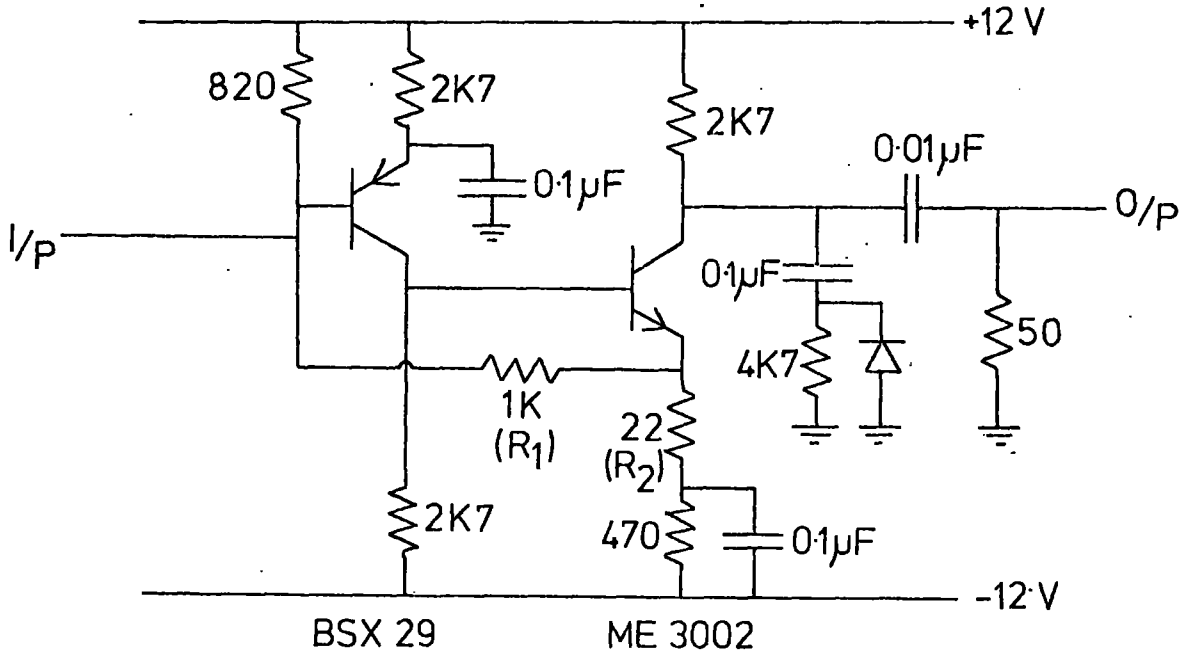

FIGURE 4.7 CURRENT AMPLIFIER CIRCUIT

Figure 4.8(a) shows a CRT trace of five consecutive pulses from an oscilloscipe triggered directly from the current amplifier when an Fe^{55} source (X-ray energy = 5.9 keV) was placed above the chamber. As expected this pulse is quite large and narrow. By feeding the current amplifier with a two or three nanosecond wide pulse from a fast pulse generator it was found that the output width was limited by the bandwidth of the amplifier to about 7 nsec. FWHM and the width of X-ray pulses of energy 15 keV or less is limited purely by this factor. Higher energy X-rays create wider pulses and this is presumably due to the corresponding increase in photoelectron range as the X-ray energy increases, causing the width of the pulse to be determined by the collection time of the ionization.

To determine the nature of the particle pulses the Fe^{55} source was replaced with a Sr^{90} beta source (maximum beta energy, from yttrium daughter nucleus, = 2.26 MeV). This time the oscilloscope was externally triggered from the scintillator telescope to ensure that the particles producing the respective trace did not stop inside the chamber. According to Evans (11) the relation between electron range and energy is given to within 5%, from 0.5 MeV to 3 MeV, by the linear relationship:

$$R_o(\text{gm cm}^{-2}) = 0.52\ E(\text{MeV}) - 0.09 \qquad 4.1$$

Accordingly a 1.1 mm thick sheet of aluminium was interposed between the chamber and telescope which, according to equation 4.1, restricted electrons triggering the oscilloscope to ones with $\beta = 0.74$, i.e. about minimum ionizing. For the particular chamber used here such particles, losing energy at about 2 MeV $gm^{-1}cm^{-2}$, will deposit 4.5 keV in the chamber, which is very similar to the energy of an

(a)

(b)

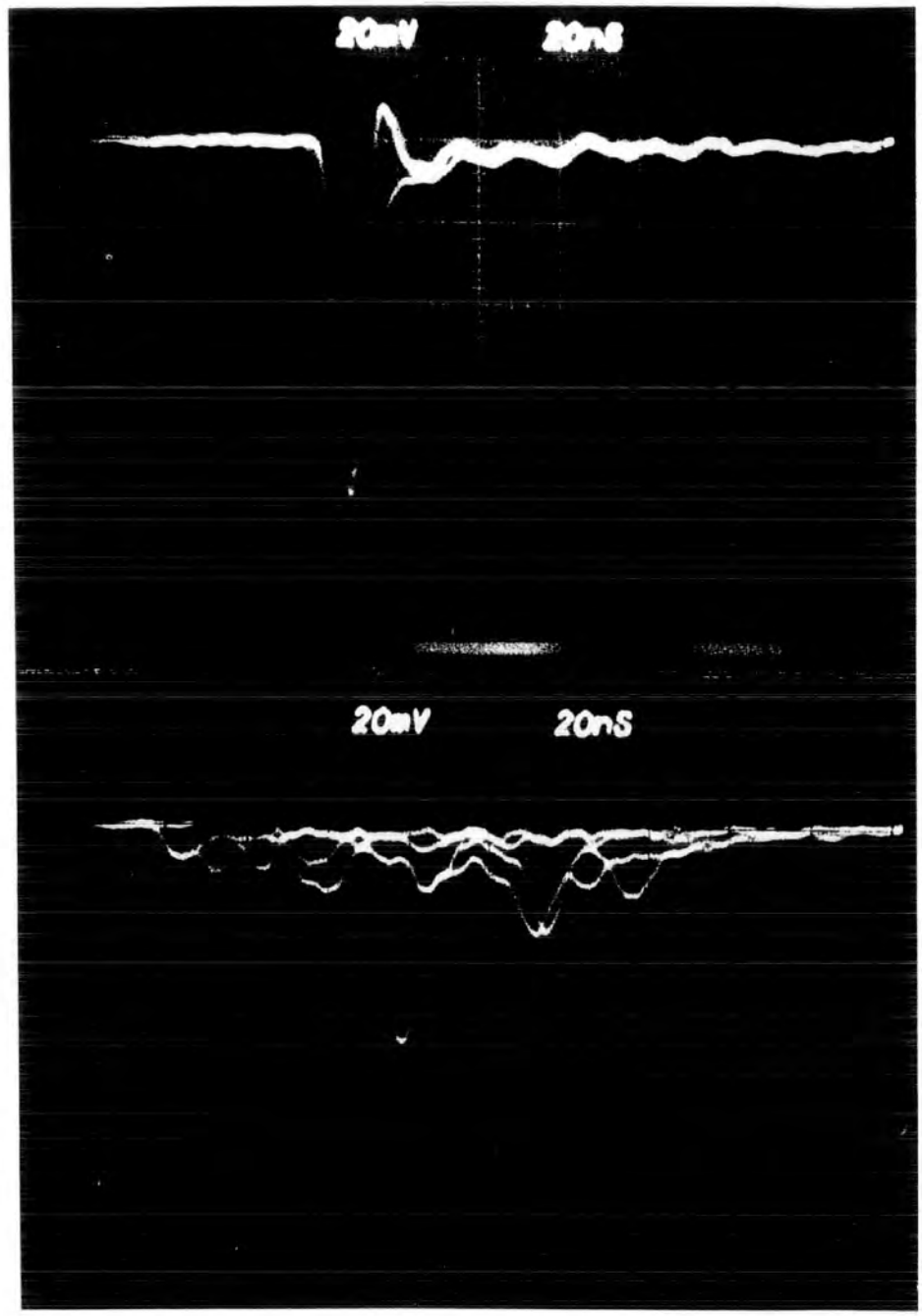

FIGURE 4.8 (a) CRT TRACE OF X-RAY PULSES

(b) CRT TRACE OF BETA-PARTICLE PULSES

Fe^{55} X-ray. Figure 4.8(b) shows five consecutive traces obtained in the manner described above; the duration of the pulses, about 160 nsec, agrees well with a drift velocity of 4 cm/ μsec over the 0.63 cm spacing between the sense wires and HT plane. It can be seen that there is a low level current distribution throughout the collection period but perturbations upon the ideal case described in § 4.3.2 are large energy transfers from particles giving delta-rays with short ranges ($\approx$ 1 mm or so) and these create the series of current spikes observed in the same photograph.

Thus, by setting a suitable threshold level on the output of the amplifier, it should be possible to let through all the X-ray pulses above a certain energy and eliminate the majority of charged particle pulses. The main problem of the technique is that occasionally a delta ray from a charged particle will have sufficient energy to exceed the threshold and will mimic an X-ray - this being referred to as a 'breakthrough'.

4.3.4 Electronic Processing

Figure 4.9 shows the electronic system to be used to implement the above ideas when XTR is being detected with a MWPC.

The charged particles are detected by the scintillators and pass through the stack and chamber. The current amplifier output from the chamber is fanned out to a discriminator and (via a suitable delay) to an integrating fast linear gate. If the amplitude of the current pulse exceeds the preset threshold, the discriminator output strobes the linear gate over the characteristic width of the X-ray pulse. The output from the linear gate is then integrated and fed into a PHA. The latter thus registers a spectrum which is proportional to the area under the current spikes, i.e. proportional to the X-ray energies. To ensure correlation with the

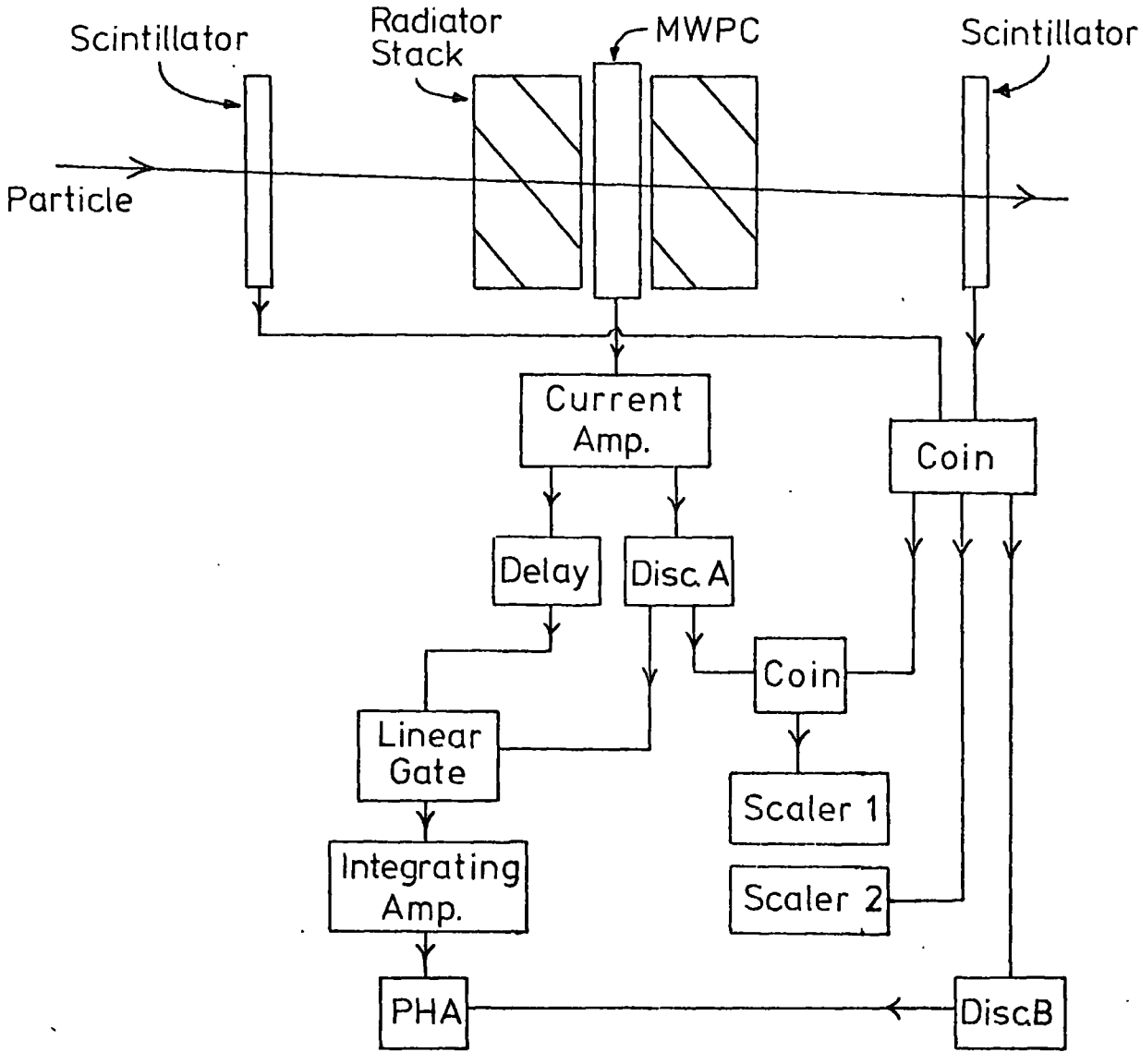

FIGURE 4.9 ELECTRONIC ARRANGEMENT FOR ANALYSING CHAMBER PULSES

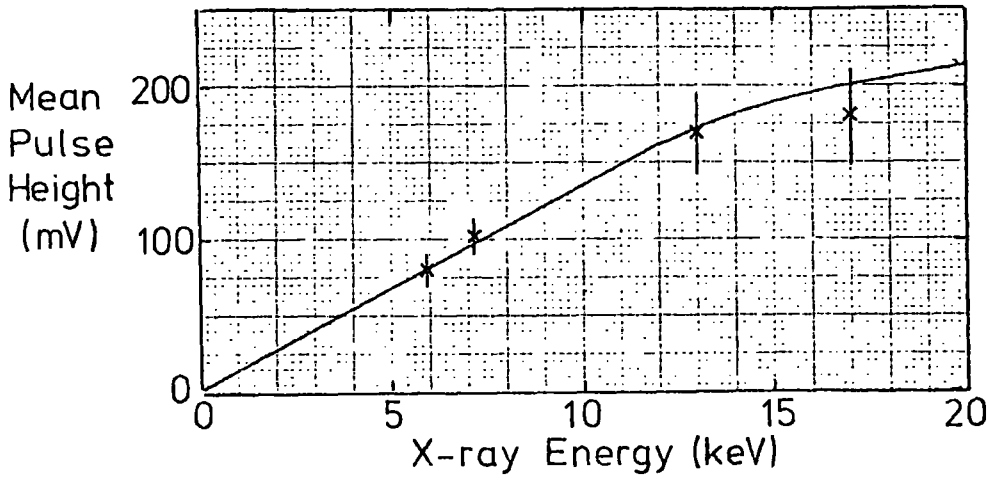

FIGURE 4.10 VARIATION OF X-RAY PULSE HEIGHT WITH ENERGY

passage of a particle the PHA is strobed by the scintillator telescopes. Calibration of the PHA range in terms of X-ray energy is achieved using a few standard X-ray source lines.

4.4 Variation of X-ray Pulse Height with Energy

It has been shown that the width of the X-ray pulse up to about 15 keV is limited by the amplifier bandwidth and remains constant so that up to this energy the height of the current pulse is directly proportional to the X-ray energy.

Above 15 keV the range of the photoelectron starts becoming significant compared to the width of the chamber (≈ 2 mm) and the pulse widens, with the result that height is no longer proportional to energy. The variation of X-ray pulse height with energy was obtained with the set-up in figure 4.6, the mean X-ray pulse height being observed on the oscilloscope, and this variation is shown in figure 4.10. The X-rays were obtained from a standard Radiochemical source which produced fluorescent X-rays from small samples of Cu, Rb, Mo, Ag, Ba and Tb by bombarding them with 60 keV X-rays from an Am^{241} source, the X-rays so produced varying in energy from 8 keV to 44 keV. The curtailment of the proportionality of pulse height with X-ray energy does not affect analysis in the PHA provided the gating pulse applied to the linear gate is wide enough to allow integration of the X-ray pulse over its complete width.

4.5 Factors leading to incorrect X-ray analysis

Ideally each channel of the PHA corresponds to a unique X-ray energy. In practice this is never so because of the variation in pulse heights from X-rays of the same energy, due to the statistical nature of the avalanche in the chamber, and irregularities in the

chamber construction and wire diameters. Again using the set-up in figure 4.6 the output of the amplifier was fed into an integrating amplifier and then to a PHA; the energy resolution of the system for the Fe^{55} 6 keV X-ray peak was about 25% (FWHM). Very small irregularities in the proportional chamber wire spacing (leading to slight changes in gas gain) would perhaps account for this being worse than the equivalent energy resolution of a single wire proportional counter filled with the same gas ($\approx 17 \rightarrow 20\%$).

There is a certain probability that a photoelectron, during its thermalisation process, will make ionizing collisions both inside and outside the active volume of the chamber. If this is so then all of its energy will not be collected by the chamber sense wires with the result that a reduced pulse height will be registered. For chambers which are one or two centimetres wide this is significant only when the photoelectron range exceeds a couple of millimetres or so, which is equivalent to an energy of about 15 keV or greater. As will be seen later one need only consider X-rays up to 20 keV when using argon-filled chambers because the absorption coefficient is so low above this energy and these have a range of 4 mm in argon so there may be a small, though not too serious, error in energy analysis in this last 5 keV range.

A further phenomenon which could contribute the same type of error is the onset of Compton scattering, competing with the photoelectric effect, for photoelectron absorption. In argon the two processes are equal in cross-section at around 60 keV, with the photoelectric effect dominating below this energy so this phenomenon can be considered negligible below 20 keV.

When X-rays are being detected in the presence of a particle there is a further error which arises in analysis. Because of the constant low level distribution of ionization produced by the particle the X-ray pulse will not in fact start from the baseline

(zero energy). By considering the area of the 6 keV X-ray pulse in figure 4.8 then the average height of the particle pulse in the same figure over the collection period of the electrons, about 160 nsec, is about 0.5 keV. Thus on average the X-ray will appear to have 0.5 keV greater energy than it actually has; the correct value for any particular X-ray will vary, though, as it depends greatly where the X-ray occurs with respect to the peaks and troughs of the particle pulse in figure 4.8.

4.6 Particle 'breakthroughs'

4.6.1 Theoretical estimate

The efficacy of the above pulse shape discrimination technique for XTR detection depends upon the relative magnitudes of X-rays and delta-rays above the energy of the threshold setting.

From the spectra generated in the previous chapter we know the number of X-rays at particular energies expected from a particle of known gamma traversing a stack of foils.

A rough estimate of the integral delta-ray spectrum from a particle passing through a chamber can be obtained from the classical Rutherford formula for the probability of an ionizing particle transferring an energy between E and E + dE to an electron in a thickness dx of a medium:

$$\int E\,dE\,dx = \frac{0{\cdot}3\,m_e c^2 z^2 Z}{\beta^2 A}\,\frac{dE}{E^2}\,dx \qquad 4.2$$

where z = particle charge

β = particle velocity

Z, A = atomic number, atomic weight of medium

and dx is expressed in gm. cm^{-2}

The number of delta-rays above a certain energy (the breakthrough rate) is thus, naturally, dependent upon the thickness of the medium, i.e. width of chamber. For the chamber in figure 4.6 $dx = 2.5$ gm cm^{-2} ; substituting this into equation 4.2 and integrating over E at various values of E gives the curve shown in figure 4.11. This is an integral spectrum so, for example, at a threshold setting of 5 keV one would expect a breakthrough rate of 3.5%, which decreases accordingly as the threshold level is increased.

Obviously the signal (X-ray pulses) to noise (breakthroughs) ratio will depend upon the gamma of the particle. When 0.035 photons are absorbed per particle the two are equal and from the predictions of Chapter 3 this X-ray flux is very easily attainable with a particle of $\gamma = 1000$.

4.6.2 Calibration of Discriminator and Pulse Height Analyser

This was achieved with the chamber in figure 4.6 attached to the electronic circuitry of figure 4.9. Discriminator A of the latter circuit determines the threshold which is applied to the output of the amplifier.

A reasonably accurate calibration of this discriminator was made in the following manner. Pulses from a fast pulse generator were fed into it to determine the pulse height corresponding to each threshold setting. The particular discriminator used in this experiment had the calibration curve shown in figure 4.12. A spectrum from Fe^{55} X-rays was then obtained from the chamber in the PHA, during the analysis of which the discriminator threshold was set at its lowest value and a pulse of 30 nsec width applied to the linear gate, which allowed ample integrating time for the X-ray pulse.

The amplifier was then disconnected from the chamber and driven by the pulse generator, the input to the amplifier being

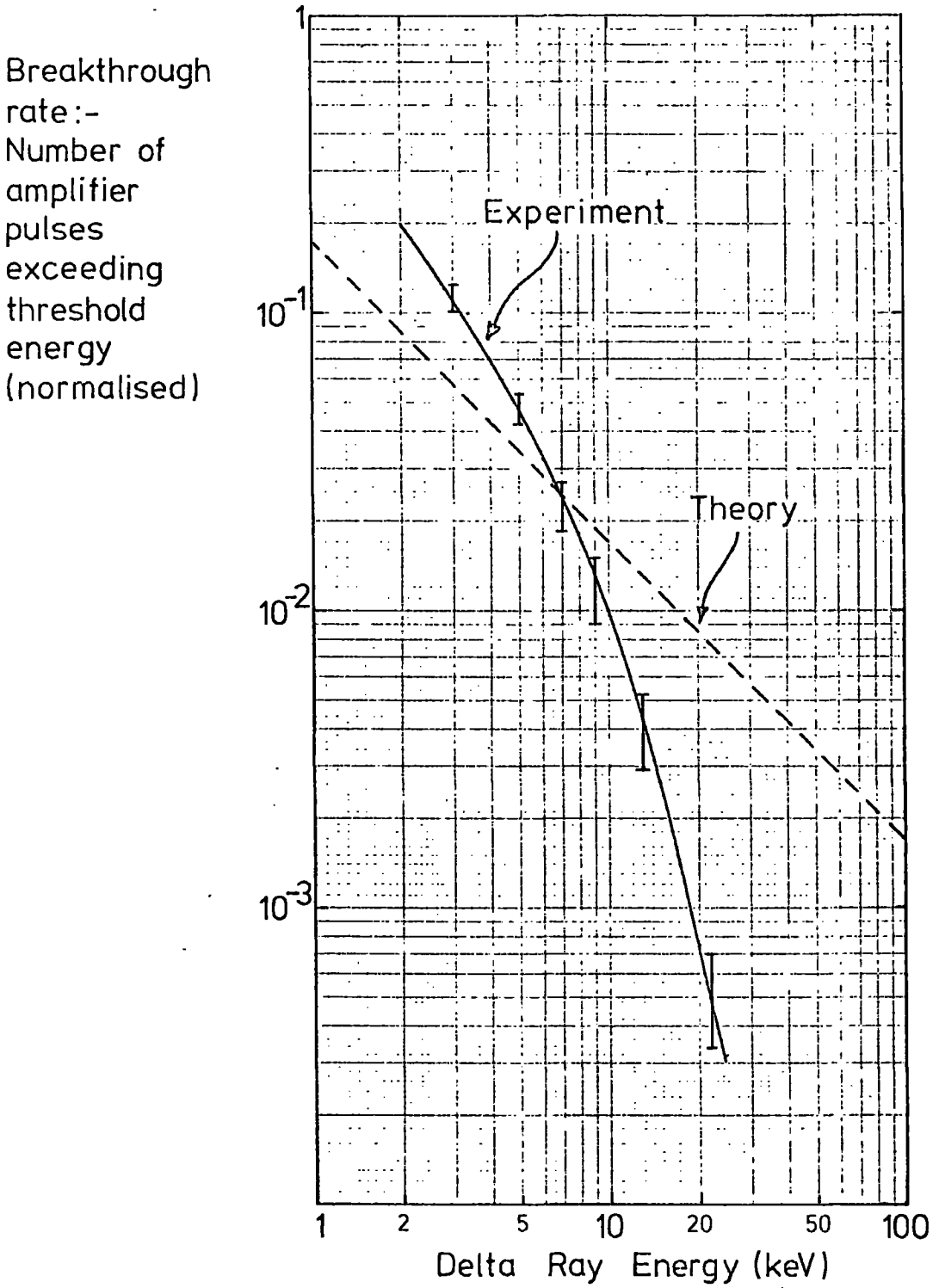

FIGURE 4.11 EXPERIMENTAL AND THEORETICAL DELTA-RAY SPECTRA FROM BETA-PARTICLES

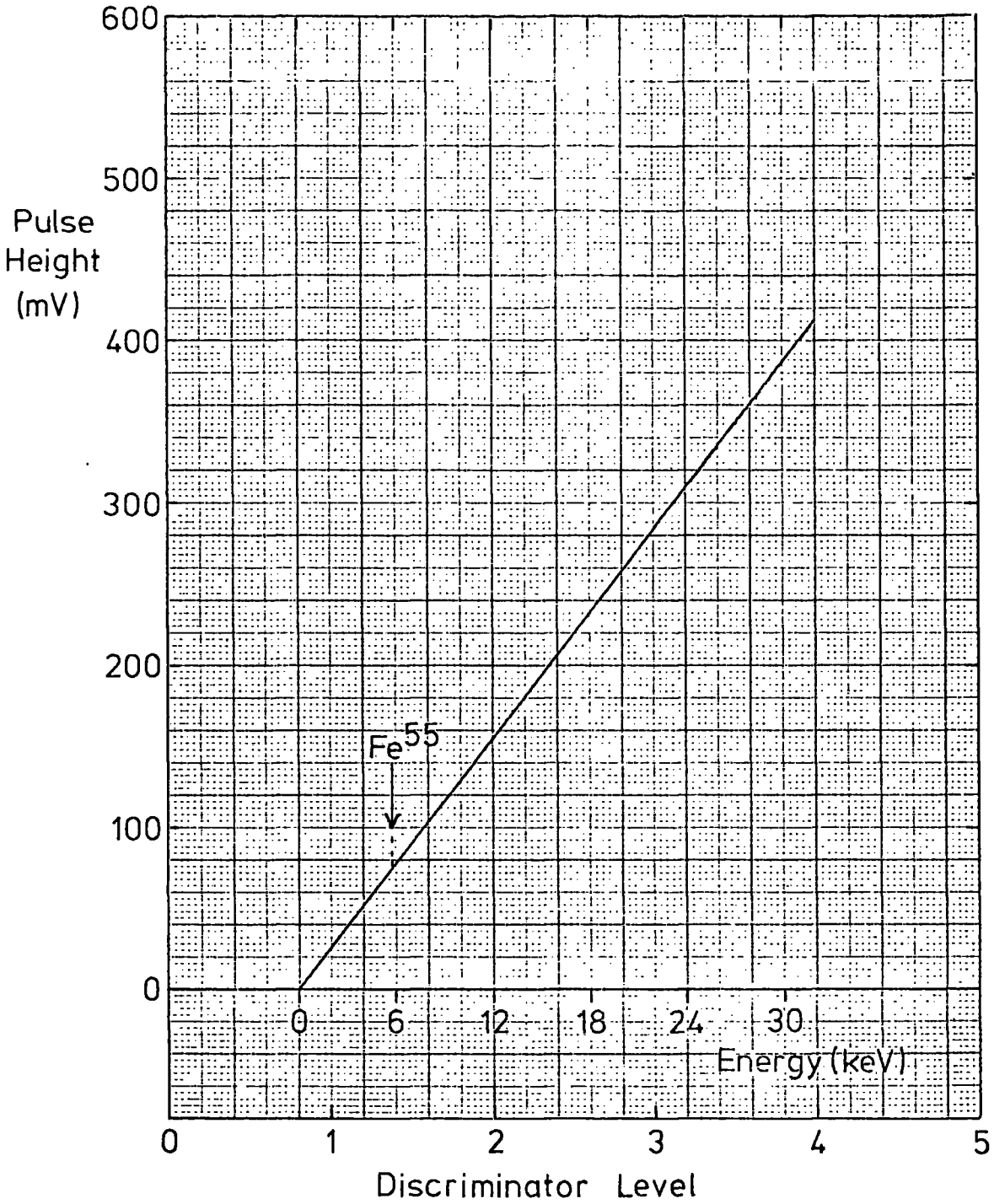

FIGURE 4.12 CALIBRATION CURVE FOR DISCRIMINATOR 'A' IN FIGURE 4.9

adjusted until the output was registered in the same channel of the PHA as the peak of the X-ray spectrum. The pulse height of this particular output was noted and marked as shown in figure 4.12, from which the threshold axis could be redrawn as an energy scale. Assuming delta-rays behave in a similar manner to equivalent energy X-ray photoelectrons then, because of the curtailment of pulse height proportionality with energy shown in figure 4.10, the scale from 15 keV upwards will become more narrowly spaced than the one actually shown.

4.6.3 Experimental breakthrough rate

The chamber, telescope, aluminium absorber and Sr^{90} beta source were set up as in figure 4.6. Because a breakthrough pulse from the chamber could occur anytime during the collection period of the electrons (about 160 nsec) the telescope discriminator pulse was lengthened to 200 nsec and the delay from the chamber discriminator to the coincidence unit was such that the particle pulse could not fire the discriminator before the telescope pulse had started.

The breakthrough rate (scaler (1) / scaler (2)) was then determined for discriminator thresholds from 3 keV to 22 keV; 3 keV was the lowest energy which the discriminator would go down to. The results are shown, together with the theoretical breakthrough spectrum, in figure 4.11; the full line is the best fit through the experimental points.

A discussion of the difference between the two distributions will be left for Chapter 6 when the delta-ray spectra from accelerator particles and cosmic rays will also be presented. However from the experimental curve it seems the breakthrough can be kept below 5% at a threshold of 5 keV (this of course is dependent upon chamber

width and gas composition) so the observation of even a few per cent of XTR photons should be possible against such a small background, a fact which will be confirmed in the following chapter.

4.7 Conclusion

The main methods used by workers in detecting transition radiation hitherto have been outlined; it was shown that in previous techniques using MWPC's the charge collected by the chamber, whether from a particle or photon, was integrated in the first instance to give a pulse height proportional to the charge collected, while the present technique involves charge collection in the current mode, in which an X-ray pulse is far greater in height than the pulse of a particle depositing a similar energy to the X-ray.

High-energy knock-on electrons from the particle produce 'breakthroughs' in the discrimination system but these only fire the system on a few per cent of triggers at the 5 keV threshold. Since the XTR spectra for particles of $\gamma = 1000$ derived in Chapter 3 generally peak above this energy it should be possible to detect XTR photons from such particles in the presence of the particle's own ionization.

CHAPTER 4: References

1. L.C.L.Yuan, C.L.Wang and H.Uto, Phys. Lett. 31B, No. 9, 603 (1970)

2. A.I.Alikhanian, K.M.Avakina, G.M.Garibian, M.P.Lorikian and K.K.Shikhliarov, Phys. Rev. Lett. 25, No. 10, 635 (1970)

3. A.I.Alikhanian, E.S.Beljakov, G.M.Garibian, M.P.Dorikyan, K.Zh.Markaryn and K.K.Shikhliarov, Sov. Phys. J.E.T.P. 16, 222 (1972)

4. L.C.L.Yuan, H.Uto, G.F.Dell Jr. and P.W.Alley, Phys. Lett. 40B, No. 6, 689 (1972)

5. F.Harris, T.Katsura, S.Parker, V.Z.Peterson, R.W.Ellsworth, G.B.Yodh, W.W.M.Allison, C.B.Brooks, J.H.Cobb and J.H.Mulvey, Nuc. Inst. and Meth. 107, 413 (1973)

6. Rutherford, Chadwick and Ellis, 'Radiations from radioactive substances', Cambridge University Press (1951)

7. Sharpe, 'Nuclear Radiation Measurement', Temple Press

8. C.T.R.Wilson, Proc. Roy. Soc. A85, 285 (1911); A87, 277 (1912); A104, 1 (1923)

9. G.F.O'Neill and W.T.Scott, Phys. Rev. 80, 473 (1946)

10. Landolt-Bornstein 1 (5) 347

11. R.D.Evans 'The Atomic Nucleus', McGraw-Hill, p.625 (1955)

CHAPTER 5

DETECTION OF X-RAY TRANSITION RADIATION FROM 1.5 GeV ELECTRONS

5.1 Introduction

Two separate experiments have been conducted to produce XTR and detect it with a MWPC, employing the pulse shape discrimination technique described in Chapter 4. The first utilized 1.5 GeV electrons, produced in the Nimrod accelerator at Rutherford High Energy Laboratory, and a transition radiation stack of 250 polythene sheets, each 40 μm thick. This experiment allowed an accurate determination of the XTR spectrum and a test of the efficiency of the new discrimination technique. The second experiment was carried out to see if the same technique could be applied to detecting XTR from cosmic rays.

The present and following chapters describe the operation and results of both experiments, bearing in mind the limitations outlined in Chapter 4, and compare the results with those expected from the theory developed in Chapter 3. Methods of improving the technique and its suitability for cosmic ray work will be discussed in the concluding chapter.

The accelerator experiment consisted of two parts, one in which detection was accomplished with a sodium iodide crystal, and the second with a conventional MWPC.

5.2 Detection of X-ray transition radiation with a sodium iodide crystal

5.2.1 Experimental arrangement

The layout for both parts was basically the same, and is shown in figure 5.1 with the crystal as detector.

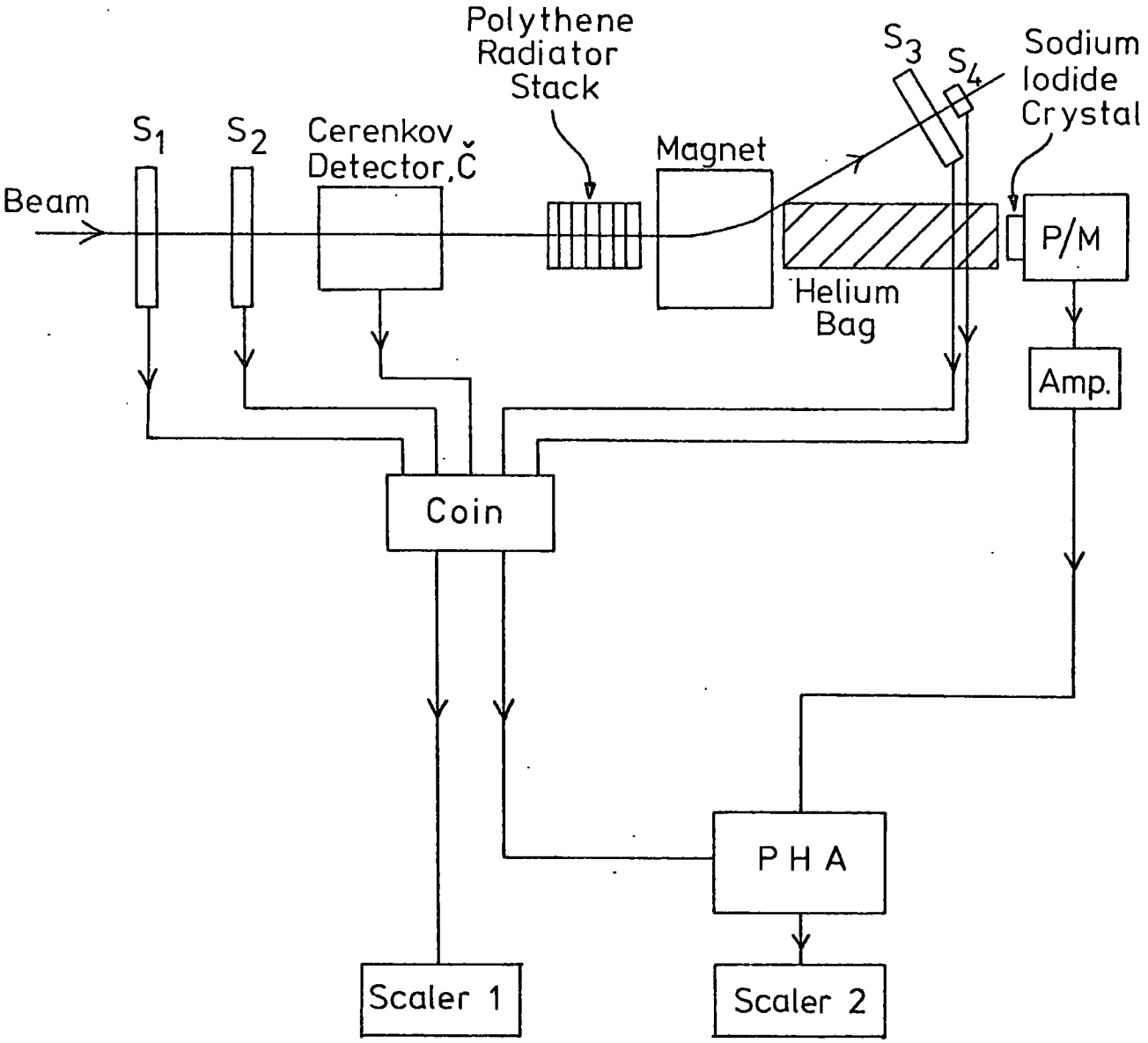

FIGURE 5.1 LAYOUT OF EXPERIMENT FOR TRANSITION RADIATION DETECTION FROM 1.5 GeV ELECTRONS

Protons produced in the Nimrod accelerator were directed on to a copper target, the resulting particles being mainly pions, kaons and photons, Most of the electron component came from the materialisation of the latter. By suitable adjustment of the magnets along the beam line to the $\pi 8$ area of the experimental hall , where the tests were carried out, a beam of negative pions and electrons was obtained.

The particles traversed two scintillators, S_1 and S_2, a sulphur hexafluoride Cerenkov detector, then the transition radiation stack before being deflected by a bending magnet into finger scintillators S_3 and S_4, one placed horizontally and the other vertically.

For the first test the detector was a 1" diameter, 5 mm thick ~~tellurium~~ thallium doped sodium iodide crystal [Na I (Tl)] which was placed adjacent to S_3 and S_4 such that the axis of the particles through the stack passed through the middle of the crystal. The radiator stack was 250 sheets of 40 μm polythene with an air spacing between each sheet of 1 mm. The space between the magnet and detector was filled with a helium bag to reduce the absorption of X-rays.

The crystal was attached to a photomultiplier(type 8550), the amplified output of which was fed directly into a PHA. The latter was strobed by a coincident pulse from the four scintillators and Cerenkov counter to ensure correlation with the passage of a particle. Electrons were signified by $S_1S_2\check{C}\ S_3S_4$ and pions by $S_1S_2\bar{\check{C}}\ S_3S_4$.

All electronics except the scintillator and crystal amplifiers were housed in a screened room alongside the apparatus to keep pick-up to a minimum.

The area of cross-section of the particle beam was about 15 cm x 5 cm, but the two finger counters restricted those particles detected to a very narrow beam and, although the distance between the stack and crystal was almost 300 cm, the fact that the XTR photons are restricted to a cone of half angle $^1/_\gamma$ (γ = 3000 for these tests) meant that they only occupied an area of a fraction of a square centimetre on reaching the crystal so it was assumed there was no loss of signal due to photons missing the crystal.

5.2.2. Experimental procedure

The current in the main bending magnet further up the beam line was adjusted to select particles of 1.5 GeV. Three separate tests were then conducted:

i) The Na I crystal output was analysed for 10,000 electron triggers with the polythene stack in position, as shown in figure 5.1.

ii) This was repeated with the stack replaced by its equivalent thickness of absorber, i.e. a 1 cm thick slab of perspex.

iii) Finally results were obtained from 10,000 electron triggers with neither transition radiator nor absorber in position.

The Na I crystal output is proportional to the energy deposited in it, whether by a particle or photon. Its output on the PHA was calibrated in terms of energy by using the variable energy X-ray source described in the last chapter.

Each particle trigger was registered on scaler (1) of figure 5.1 and if there was a simultaneous output from the crystal this was analysed by the PHA and registered by scaler (2).

Therefore the ratio of scaler (2) to scaler (1) corresponded to the electron detection efficiency of the system.

5.2.3 Results and Discussion

Run (i), with the electrons traversing the stack, gave a detection efficiency of $(59.3 \pm 0.5)\%$, while that of run (ii) with the background radiator yielded $(6.8 \pm 0.3)\%$ efficiency. The latter run gives the number of background counts, which are due to a combination of bremsstrahlung created in the absorber by the electrons and accidentals, i.e. particles passing through the detector during the gating time of the PHA. The third run gave a detection efficiency of $(4.8 \pm 0.4)\%$. Thus about $(2.0 \pm 0.4)\%$ of counts were due to the creation of bremsstrahlung in the stack material, the remaining background being due to accidentals. This high accidental rate can be accounted for by the fact that the gating pulse applied to the PHA was quite long (800 nsec).

The detection efficiency by XTR alone is not just $(59.3 - 6.8)\%$ since there is a possibility of an X-ray being detected at the same time as the occurrence of a background count, and this is only recorded as one event; the true XTR rate is actually higher than the figure given by the above subtraction.

If b = probability of a background count

x = probability of an X-ray count

and c = probability of recording an event whether by X-ray or background alone, or a combination of both, then

$$b + x - xb = c \qquad 5.1$$

Substituting $b = 0.068$ and $c = 0.593$ we obtain $x = 0.566$, i.e. the detection efficiency by XTR alone is 56.6%.

The histogram in figure 5.2 represents the PHA spectrum from run (i), that of 10,000 electrons traversing the polythene stack, i.e. the background counts are included. Had they been subtracted, 7.2% of the XTR counts would also be removed for the reason given above, so it is impossible to get the true XTR spectrum. The above procedure only adds 4.5% more counts due to the background.

The full line in figure 5.2 represents the XTR spectrum from 10,000 electrons traversing the above polythene sheet stack which has been computed from the expression for the differential number spectrum of photons from a radiator stack derived in Chapter 3. The absorption of X-rays in the helium and its container walls has been folded into this distribution, assuming an absorption coefficient in helium as shown in figure 5.3. According to the above computation there are 1.03 photons emitted per particle from the stack, and 0.97 absorbed per particle by the detector. Thus there is only a 6% loss of signal in the helium bag, the majority of which occurs in the region 0 - 3 keV.

Agreement between the two distributions is exceedingly good, the experimental one peaking at about 17 keV and the theoretical one at about 14 keV. The main difference between the two is that the former distribution is only about 50% of the height of the theoretical one at the peak energy, but contains a greater number of X-rays to the right of this peak, falling off gradually to 100 keV, while the theoretical one falls quite sharply from its peak to 50 keV. This is almost certainly due to creation, and absorption by the crystal, of more than one X-ray for the passage of one particle which is recorded in the PHA as the sum total of their energies but is only registered as a single event on the scaler. Thus the number of high energy events analysed is

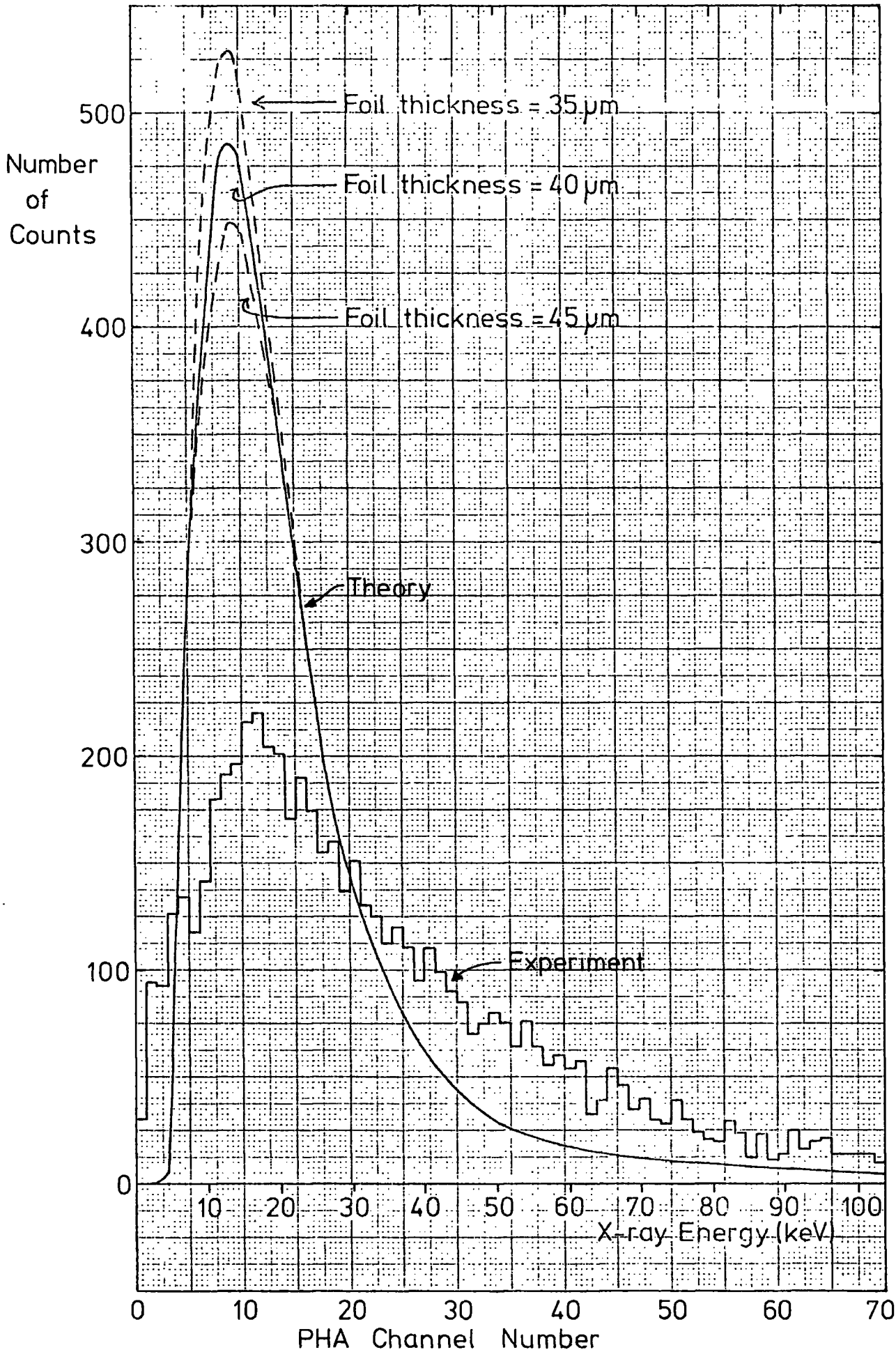

FIGURE 5.2 EXPERIMENTAL AND THEORETICAL TRANSITION RADIATION SPECTRA FROM 10,000 1.5 GeV ELECTRONS DETECTED BY NaI CRYSTAL

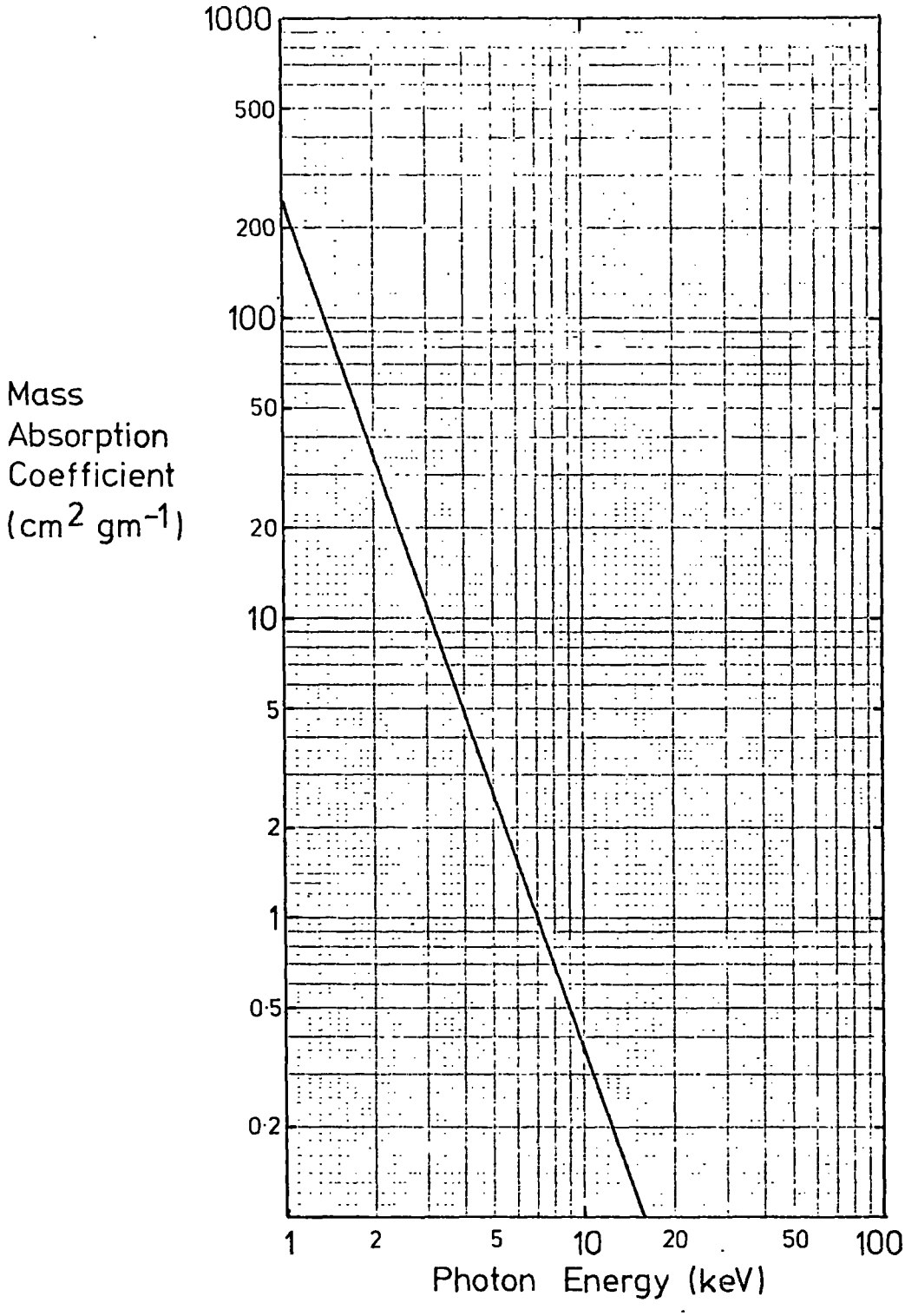

FIGURE 5.3 MASS ABSORPTION COEFFICIENT OF HELIUM

increased at the expense of low energy ones, thereby accounting in part for the difference in the height of the peaks.

The total number of photons in the predicted spectrum yields an electron detection efficiency of 97%, which is just over half as large again as that measured experimentally. This again can be accounted for, partly, by the events in which more than one X-ray is absorbed by the crystal.

From the experimental distribution a beam of 1.5 GeV pions and electrons could be separated with 57% efficiency, since 1.5 GeV pions would not produce a detectable quantity of XTR.

5.2.4 Accuracy of distributions

i) Experimental

It has been assumed that no XTR passes beyond the circumference of the crystal and this, as shown earlier, is quite valid because of the very small half angle of the cone of the radiation. The resolution of the crystal could degrade the spectrum but at an energy of 22.2 keV (the Ag k_{α} line) the FWHM of the distribution was about 24% so, at and below this energy, X-ray analysis would be fairly accurate.

In addition it was assumed there were no impurities or leaks in the helium bag; if this assumption were wrong the experimental electron detection efficiency would be brought nearer the predicted value because of absorption of some of the XTR signal.

ii) Theoretical

The theoretical distribution assumes that all X-rays which reach the crystal are absorbed by it and this is reasonably valid since the X-ray detection efficiency of the crystal in the energy range 10 - 70 keV was known to be greater than 98%. The polythene sheets were 40 μm thick and even allowing for a 10% variation in

thickness either way the predicted spectrum barely changes shape at all, except that the height of the peak goes up for thinner sheets and down for thicker ones: the dotted lines in figure 5.2 show the expected spectra for 35 μm and 45 μm thick sheets, the one for the former stack containing 11% more photons, and 8% more energy, than the latter one. The position of the peak energy remains constant to within 0.2 keV.

5.3 XTR detection with MWPC's

For the next series of tests the crystal was replaced by a 20 cm x 20 cm active area MWPC of the same basic construction as the small chambers, A and C, used in the dead-space measurements. The sense wire spacing was 2 mm and the HT plane - sense wire plane separation was 0.8 cm.

The chamber was flushed for several hours with a mixture of 90% argon and 10% methane and then sealed. In this way it was found the chamber would operate without deterioration or change in gas gain for up to a week. The central eighty wires were connected together and attached to a current amplifier of the type shown in figure 4.7. The amplifier output and trigger pulse from the scintillators were fed into the electronic processing circuit of figure 4.9. Because the purpose of this particular experiment was to determine the efficiency of the new pulse shape discrimination technique the bending magnet was not utilised and both XTR photons and particles were directed toward the chamber. The two finger counters, S_3 and S_4, were placed behind the MWPC so that their point of intersection centred on the mid-point of the chamber.

5.3.1 Experimental procedure

The threshold of the discriminator into which the chamber amplifier was fed was calibrated in terms of pulse height and the PHA range in terms of energy as described in § 4.6.2. The gating pulse applied to the linear gate was 30 nsec, as in the previous test.

Runs were then made in the following manner. The polythene stack was placed, not in its previous position, but directly in front of the MWPC so that there was no loss of signal from absorption in the air. The discriminator threshold was reduced to its lowest value (equivalent to 3.0 keV) and the ratio of counts on scalers (1) and (2) measured for 1.5 GeV electrons. Scaler (1) gave the sum total of delta-ray breakthroughs, bremsstrahlung and XTR photons which were detected.

A similar run was made with 1.5 GeV pions and because of the reduced gamma of this particle relative to the electron there was negligible XTR signal. Comparison of this run with one of pions traversing neither a stack nor equivalent absorber showed the detection of bremsstrahlung by the chamber was negligible so the result of pions traversing the stack essentially gave the delta-ray breakthrough rate. This meant good statistics on the latter could fairly quickly be obtained because the composition of the $\pi 8$ beam at 1.5 GeV was roughly 90% pions and 10% electrons. Conversely the low percentage of electrons meant long runs were necessary to obtain equal statistics on the XTR count rate.

These runs were repeated at gradually increasing thresholds up to an equivalent energy of 17.1 keV.

Finally, an independent run was made with 10,000 1.5 GeV electrons traversing 80 cm of packing foam to see how XTR production in this compared with that in the regularly spaced polythene stack.

5.3.2 Results and discussion

Figure 5.4 shows the two experimental integral distributions for pions and electrons traversing the polythene stack, the lower curve being the delta-ray spectrum and the higher one the combined delta-ray and XTR spectrum. Allowing for events where an X-ray and delta-ray occur simultaneously, as described in § 5.2.3, subtraction of one from the other yields the true XTR spectrum shown in figure 5.5, where the pure delta-ray spectrum is shown again for comparison.

Also shown in figure 5.5 are the expected delta-ray spectrum for a 1.6 cm thick chamber with a 90% argon/10% methane gas filling, as predicted by the Rutherford formula for the probability of energy transfer (equation 4.2) and the predicted XTR spectrum which should be measured by the MWPC. The latter was obtained in the following way:

The transmitted component of X-rays passing through a thickness dx(gm cm^{-2}) of medium is given by:

$$I = I_o \, e^{-\mu \, dx} \qquad 5.2$$

where I_o = original X-ray flux

μ = X-ray mass absorption coefficient of the medium

If $\frac{dN}{dE}$ represents the X-ray number spectrum emerging from the polythene stack, then taking into account the absorption of photons in the chamber windows, the number spectrum absorbed in the chamber is given by:

$$\frac{dN_A}{dE} = \frac{dN}{dE} \, e^{-\mu_M dx_M} \left[1 - e^{\mu_G dx_G} \right] \qquad 5.3$$

where suffixes M and G refer to melinex and gas respectively. The mass absorption coefficient for argon is shown in figure 5.6, and was obtained from X-ray absorption data in reference 1. The melinex absorption coefficient has already been shown in figure 3.4.

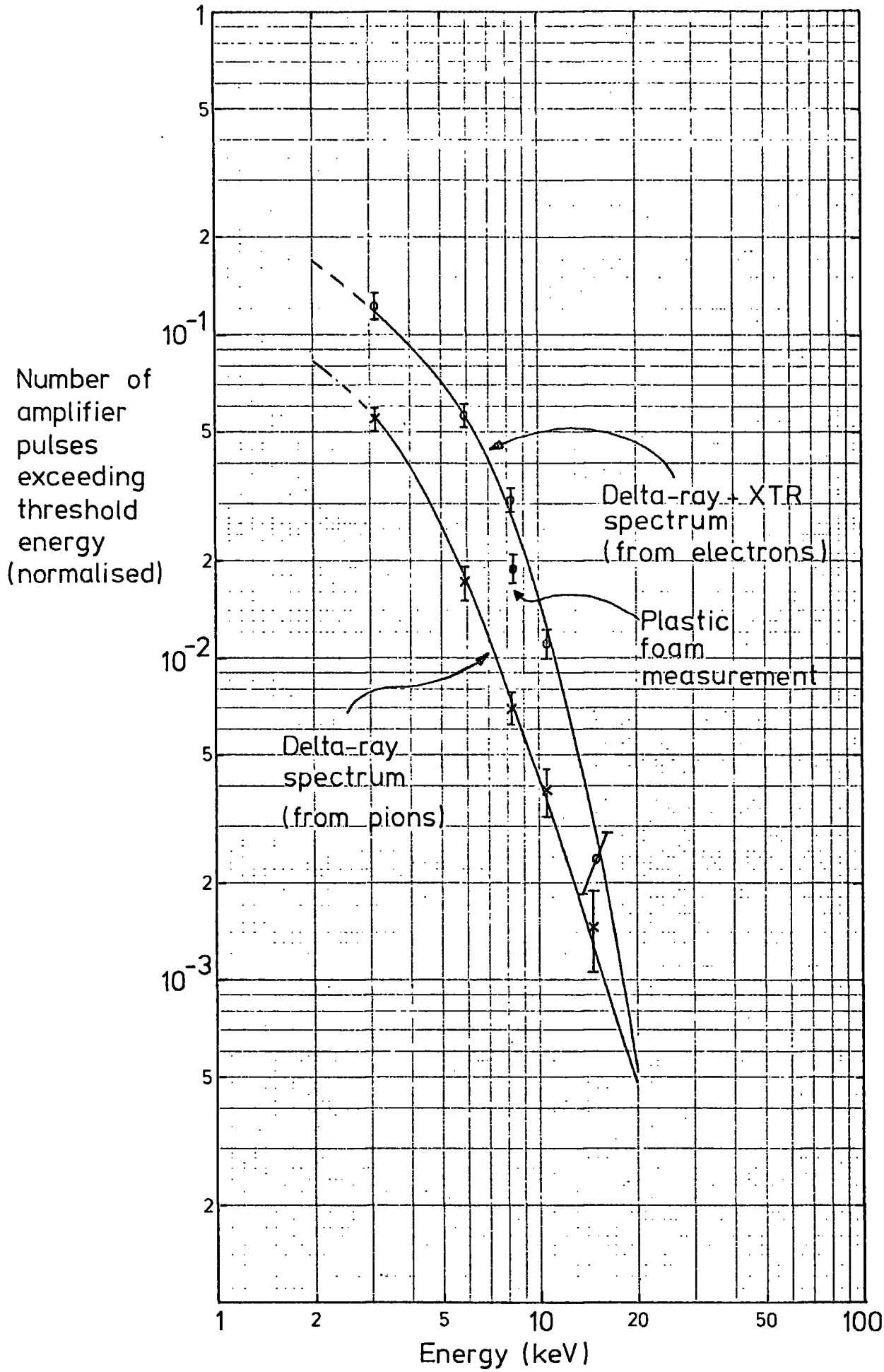

FIGURE 5.4 EXPERIMENTAL INTEGRAL DELTA-RAY AND (DELTA-RAY + XTR) SPECTRA FROM 1.5 GeV ELECTRONS DETECTED BY CHAMBER

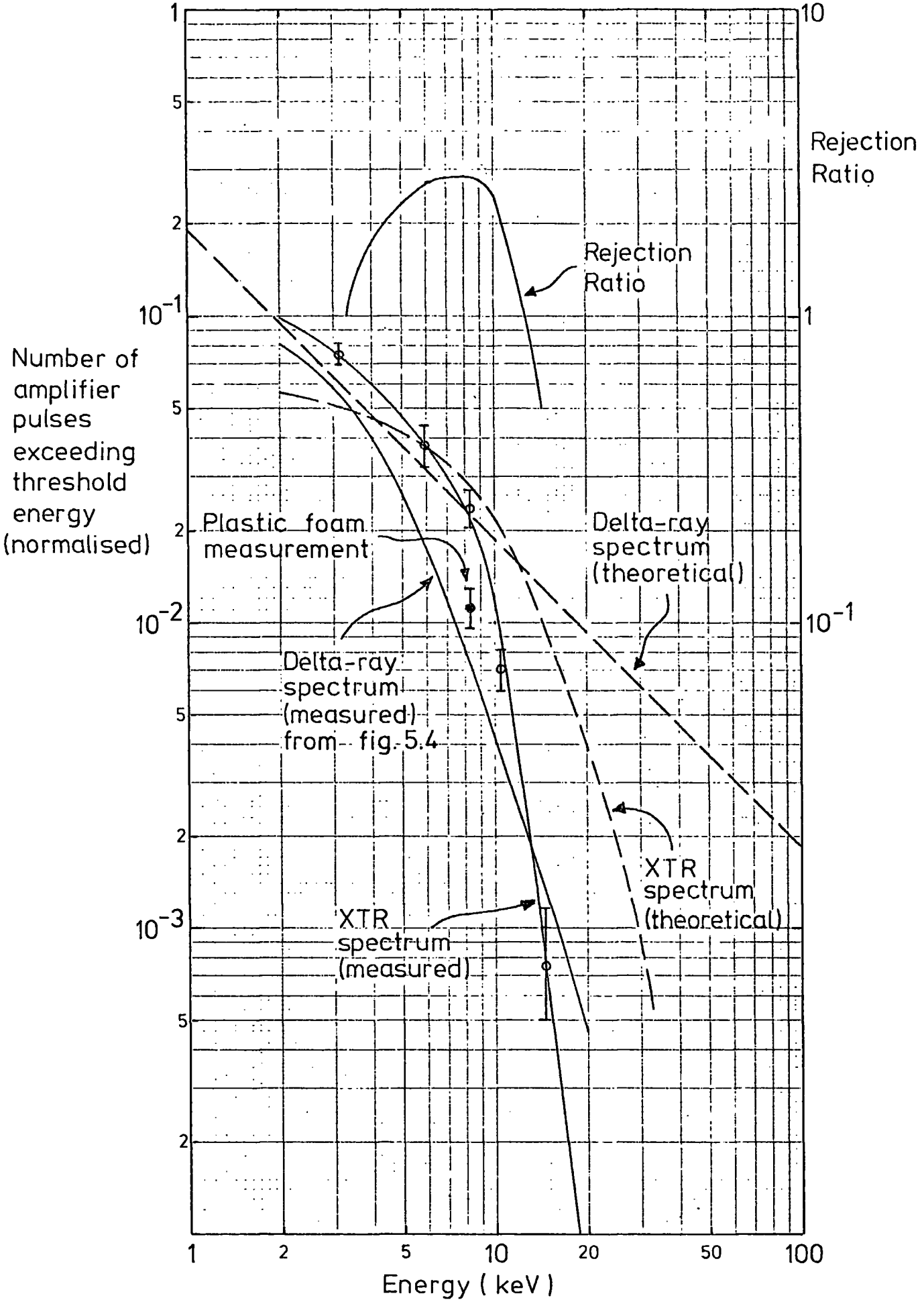

FIGURE 5.5 EXPERIMENTAL AND THEORETICAL INTEGRAL DELTA-RAY AND XTR SPECTRA FROM 1.5 GeV ELECTRONS DETECTED BY CHAMBER

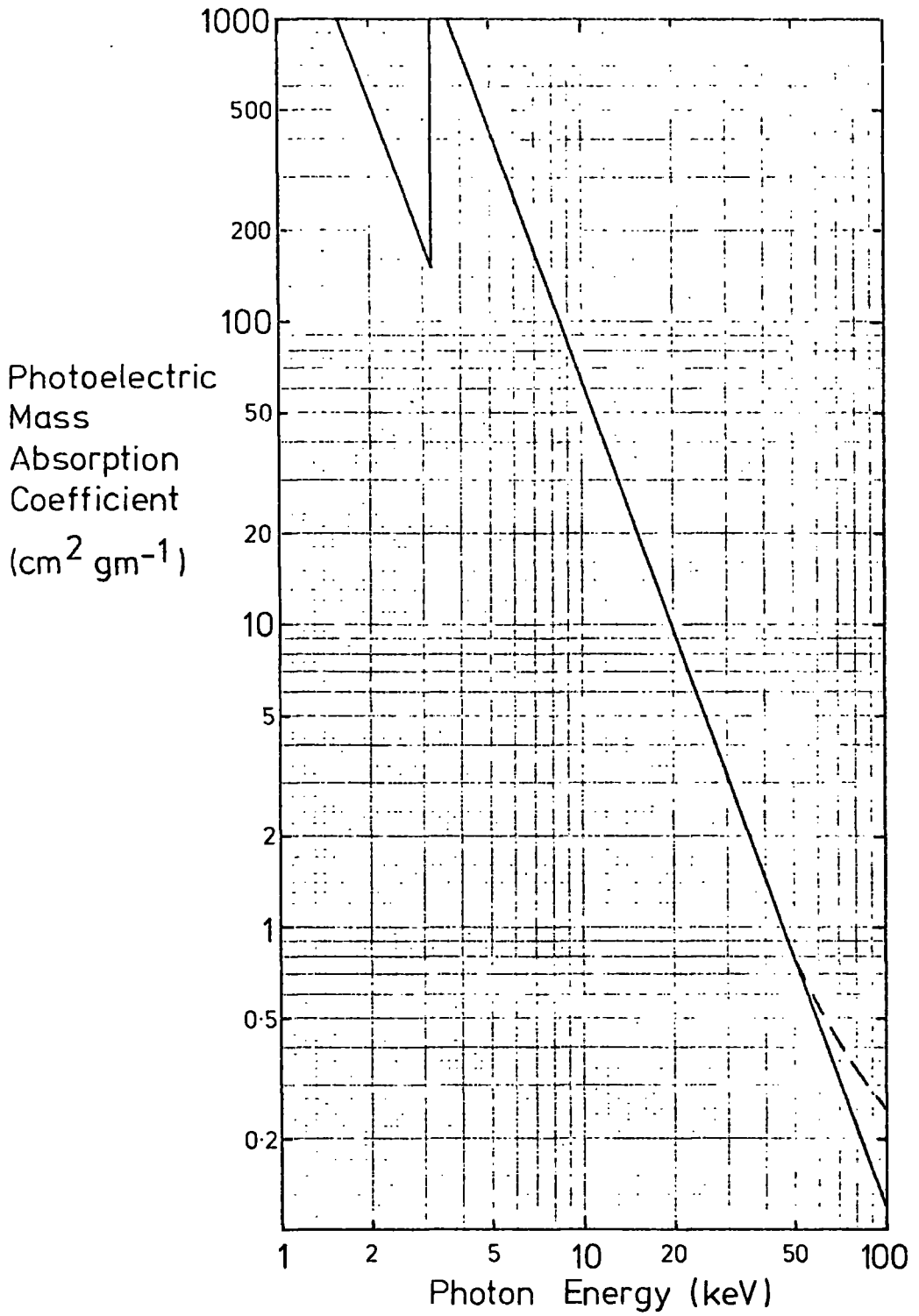

FIGURE 5.6 PHOTOELECTRIC MASS ABSORPTION COEFFICIENT OF ARGON

The ratio of $\frac{dN_A}{dE}$ to $\frac{dN}{dE}$ gives the chamber detection efficiency as a function of energy, and computation of equation 5.3 to determine this ratio yields the efficiency curve in figure 5.7. It has a peak efficiency of 39% in between 5 and 6 keV, which falls quite rapidly on either side so there is a large fraction of signal missed by the chamber. The XTR spectrum expected from the chamber is obtained by multiplying this efficiency curve by the experimentally measured spectrum emerging from the transition radiation stack.

The spectrum detected by the Na I crystal in the first experiment contained only a 6% loss from the number of photons actually emerging from the polythene stack; therefore this spectrum (figure 5.2) was taken as the experimental one and figure 5.8 shows the result of folding the detector efficiency curve into the spectrum. Integration of this differential spectrum yields the integral XTR spectrum expected from the chamber, shown in figure 5.5.

5.3.3 Analysis of delta-ray and XTR spectra

A direct comparison of the experimental delta-ray spectrum with that obtained for beta rays in Chapter 4 will be deferred until the cosmic ray results have also been presented. However, in figure 5.5 the experimental distribution once again decreases more rapidly than the theoretical one as the energy increases and this is assumed to be due to the increase in range of the delta-ray with energy, such that the width of its current pulse increases at the expense of its height.

The shape of the experimental XTR spectrum can fairly easily be explained. Figure 5.8 shows that the peak of the expected differential spectrum occurs at about 6 keV. Up to this energy one would therefore expect a gradually decreasing integral spectrum,

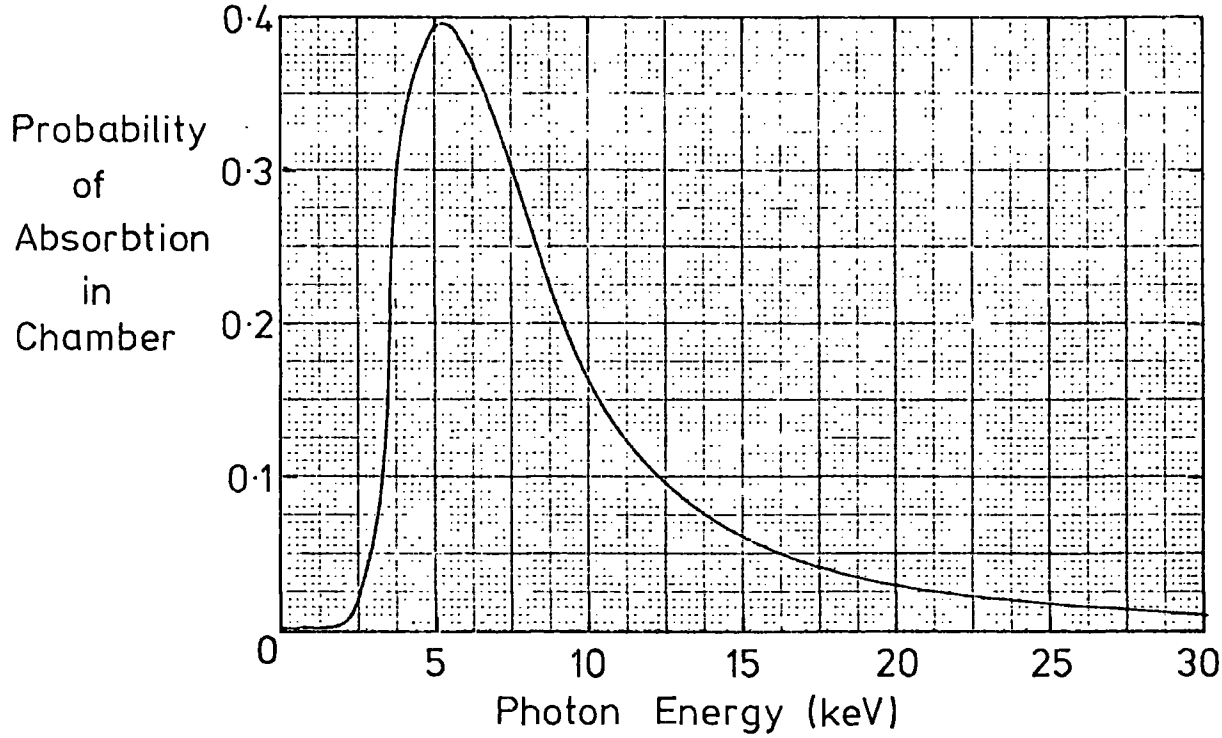

FIGURE 5.7 DETECTION EFFICIENCY OF 1.6 cm THICK ARGON/METHANE PROPORTIONAL CHAMBER

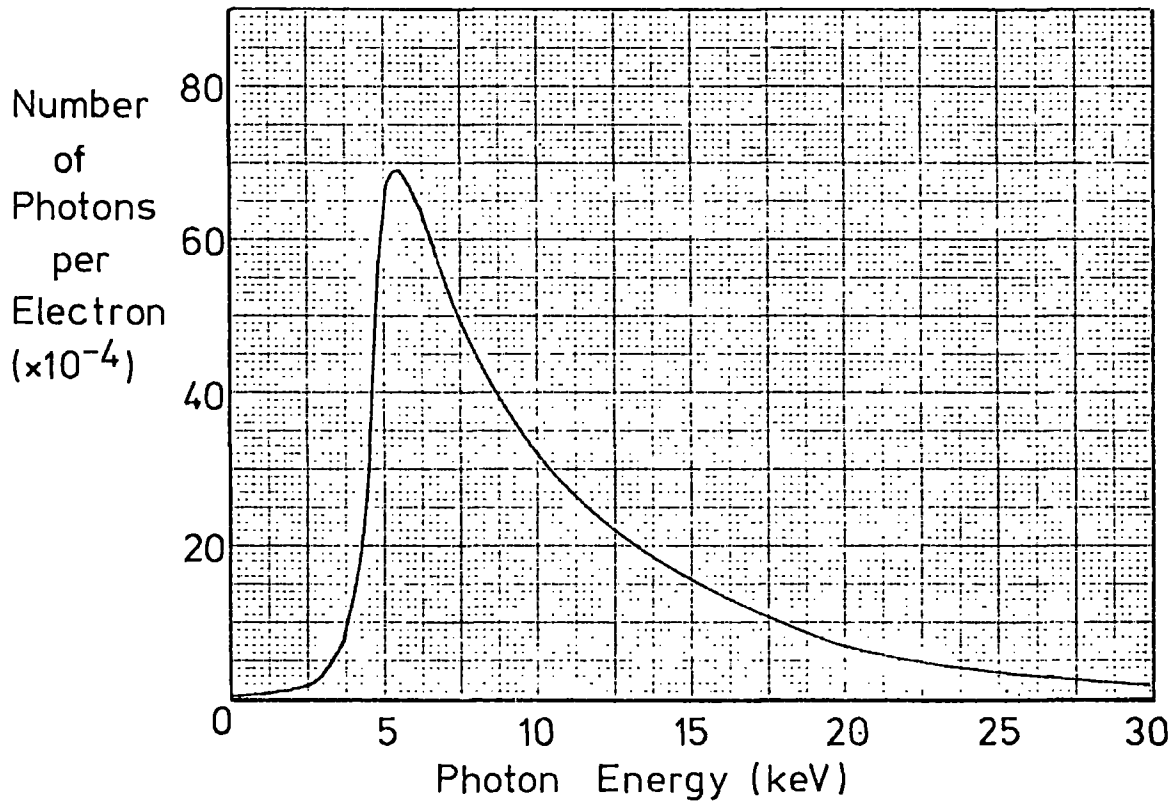

FIGURE 5.8 PREDICTED DIFFERENTIAL TRANSITION RADIATION SPECTRUM FROM 1.5 GeV ELECTRONS MEASURED BY CHAMBER

but above 6 keV, when the number of X-rays detected drops quite dramatically, it should decrease far more rapidly, and indeed there is a distinct change in slope of the integral spectrum between 6 and 8 keV.

The expected XTR spectrum has the same general shape as that measured directly by the chamber, but is smaller at low energies and larger at higher energies. The 6% loss in signal in the crystal experiment concerned only very low energy X-rays so this accounts for the low value of the expected XTR spectrum in this region. The discrepancy at higher energies is due to the corresponding X-ray photoelectrons having longer ranges as described earlier and so the experimental spectrum recorded is smaller than it should be. Allowing for these two minor differences the overall agreement of these two spectra show that the pulse shape discrimination process is functioning correctly and can efficiently separate an X-ray signal from that of a particle.

The ratio of the experimental X-ray detection efficiency to delta-ray breakthrough rate gives the rejection ratio curve also shown in figure 5.5. The peak of this curve gives the energy threshold at which rejection of transition radiation events from non-transition radiation events (or the separation of electrons from pions, say) is greatest, and in this case corresponds to about 8 keV.

Figure 5.9 shows the pulse height spectra from the MWPC for the two runs with 10,000 1.5 GeV electrons with and without the radiator stack in position, at the lowest threshold setting of 3 keV. With the stack there is a 12.9% detection efficiency, and without 5.5%; the latter distribution essentially represents the delta-ray spectrum. Figure 5.10 shows the delta-ray distribution subtracted from the combined delta and XTR spectrum which, apart

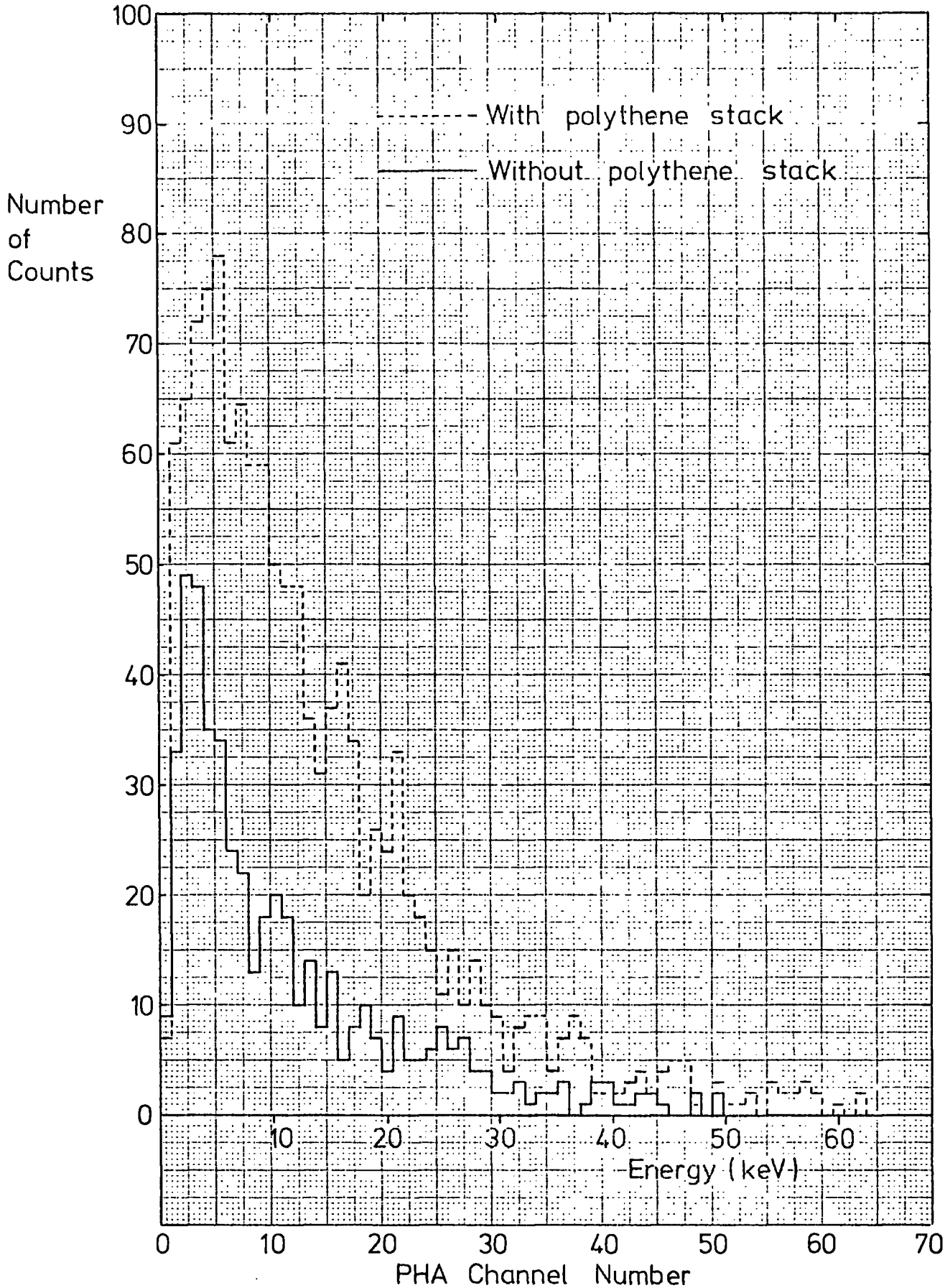

FIGURE 5.9 PULSE HEIGHT SPECTRA FROM 10,000 1.5 GeV ELECTRONS WITH AND WITHOUT POLYTHENE STACK (THRESHOLD = 3.1 keV)

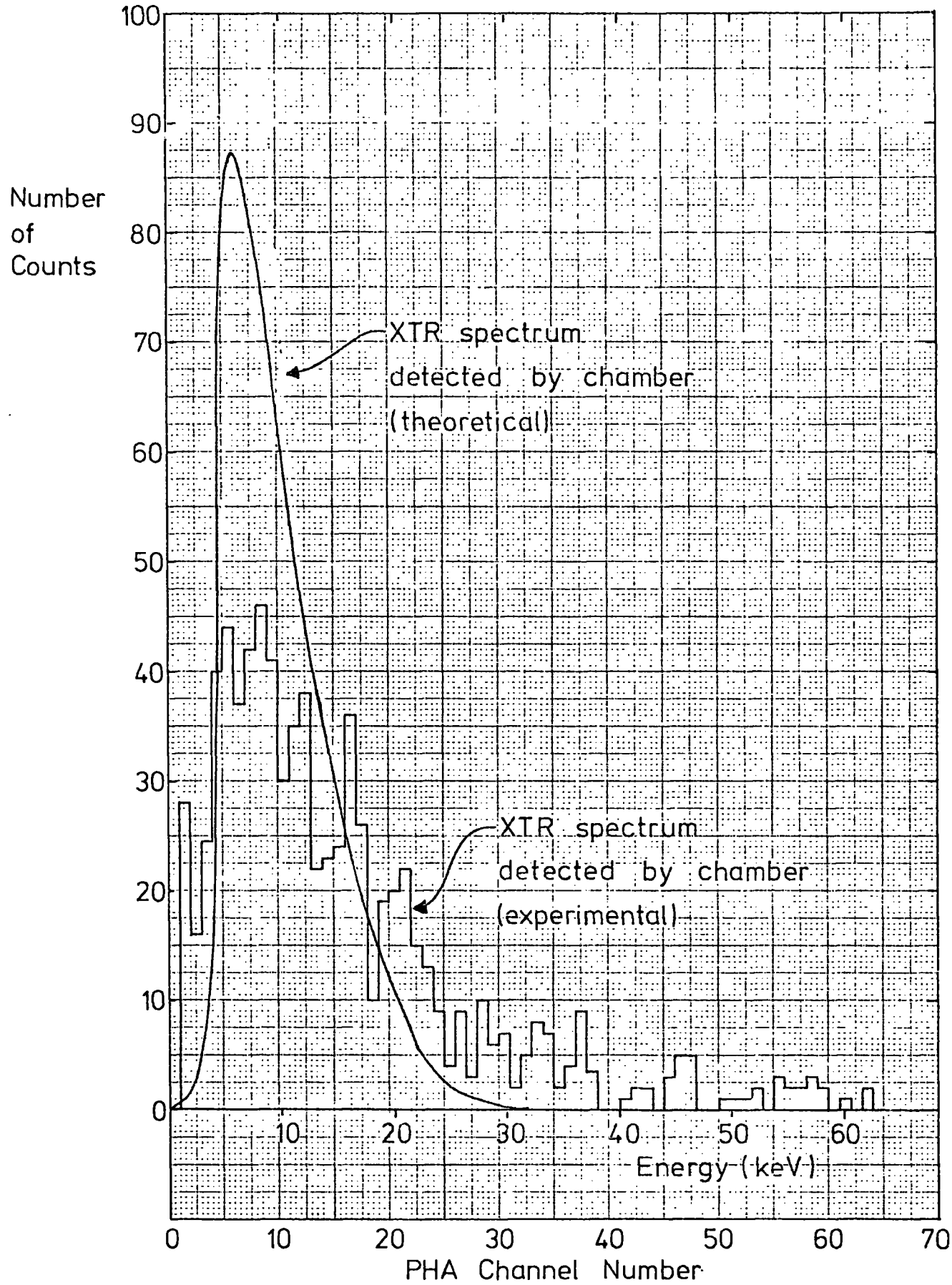

FIGURE 5.10 EXPERIMENTAL AND THEORETICAL DIFFERENTIAL XTR SPECTRA FROM 10,000 1·5 GeV ELECTRONS

from a small error due to events where an X-ray and delta-ray pulse occur simultaneously, represents the true detected XTR spectrum. The smooth curve superimposed upon the PHA spectrum is that of the theoretical spectrum from the polythene stack, shown in figure 5.2 into which has been folded the loss of X-rays in the melinex window of the chamber and the chamber detection efficiency.

The experimental distribution represents a total of (772 ± 40) photon counts, while the theoretical one predicts 900. The closeness of these two figures, though they do not agree within experimental error, indicate that the transition radiation theory is reasonably accurate.

The experimental distribution is considerably wider than the theoretical one, but the important point is that both peak at around the same energy, that of the former at 7.4 keV, and the latter at 6.1 keV. The major reason for the wider experimental distribution is the finite energy resolution of the chamber.

5.4 X-ray transition radiation in plastic foam

Only one measurement with the plastic foam was taken because of the limited beam time available. The discriminator threshold chosen was at the energy corresponding to the peak of the rejection ratio curve for the polythene stack, i.e. 8.25 keV; it was presumed that the foam would yield the same type of XTR spectrum as the polythene stack (though not necessarily the same magnitude) because of their similar chemical composition.

The plastic foam had an average void size of 600 μm and average wall size of about 30 μm. These are greater than the

respective formation zones for 1.5 GeV electrons up to the maximum photon energy of interest here, 20 keV (as shown earlier in figure 3.2). As the foam was 80 cm long it corresponded approximately to a stack of 1250 foils. From figure 3.6, showing the XTR energy content generated by a particle of $\gamma = 1000$ traversing different size stacks, an idea can be obtained of the difference between the foam and 250 foil polythene stack. The diagram shows 14 keV is produced in 1250 melinex foils and 6 keV in 250 melinex foils. Although the former energy is over twice as large as the latter, most of the difference in energy will be contained in photons around 20 keV, because of preferential absorption of low energy photons in the last part of the stack, and these higher energy photons have a much smaller absorption probability in the chamber. Therefore, to a first order, the foam can be taken as equivalent to the polythene stack.

The combined delta-ray and XTR photon rate for electrons traversing the foam was (0.019 ± 0.002) per particle, as shown in figure 5.4. This is equal to a pure XTR signal of (0.011 ± 0.002) per particle, which is roughly half that obtained with the polythene stack (figure 5.5).

Allowing for the approximate equivalence of the polythene and foam stacks used in this instance, the above result supports that of other experiments which find that a foam radiator generally produces one third to one half the radiation from a similar, regularly spaced, foil stack (2,3).

5.5 Conclusion

The discrimination technique developed in Chapter 4 has been shown to work effectively in a particle beam of 1.5 GeV electrons and pions. The transition radiation produced by the electrons (the spectrum of which was in fair agreement with that predicted by theory for the 0 $\rightarrow$ 20 keV range) enabled electrons to be partially differentiated from the non-radiating pions, a maximum rejection ratio between the two of 2.8 being achieved, at a transition radiation photon energy of 8.25 keV.

A foam stack was found to be about half as efficient a radiator as one composed of polythene foils, a very important result in view of the ease of obtaining a foam stack relative to one with regularly spaced foils.

CHAPTER 5: References

1. The Chemical Rubber Company Handbook of Chemistry and Physics.

2. L.C.L.Yuan, Int. Conf. on Instrumentation for High Energy Physics, 334 (Frascati 1973)

3. F.Harris, T.Katsura, S.Parker and V.Z.Peterson (University of Hawaii), R.W.Ellsworth and G.B.Yodh (University of Maryland), W.W.M.Allison, C.B.Brooks, J.H.Cobb and J.H.Mulvey (University of Oxford), Nuc. Inst. & Meth. 107, 413 (1973)

CHAPTER 6

DETECTION OF X-RAY TRANSITION RADIATION FROM COSMIC RAYS

6.1 Introduction

The main purpose of this experiment was to investigate the possibility of detecting transition radiation from cosmic rays.

The major component of the sea-level cosmic ray spectrum is the muon (m_μ = 106 MeV). Unfortunately the vertical spectrum contains a large fraction of low energy muons which will not produce a significant quantity of transition radiation, e.g. a muon with gamma equal to 1000 has an energy of 100 GeV, and the vertical spectrum has a mean energy of around 1 to 2 GeV. To absorb particles with energy less than 100 GeV would require 60 metres of iron, assuming an energy loss of 2 MeV gm^{-1} cm^{-2}, which was out of the question in this case, so it was found necessary to use only those particles with large incident zenith angles since the longer path length in the atmosphere in this direction absorbs many of the low energy particles and increases the mean energy to about 20 GeV. Although the vertical sea-level spectrum contains about 70% muons, 29% electrons and 1% protons and neutrons, the single particle spectrum at zenith angles greater than 80^o consists entirely of muons, since all other particles are absorbed in the thickness of the atmosphere ($\approx$ 5000 gm cm^{-2}).

6.2 Experimental arrangement

The flux of horizontal muons of any energy is very low so a system was built with a fairly large solid angle acceptance. There already existed in the laboratory scintillator telescopes of area 60 x 30 cm^2 so a MWPC was designed from perspex with an active area of 66 x 33 cm^2. Two scintillators were to act as a trigger for cosmic

rays so the slightly larger area of the chamber over the scintillators was to ensure that no particle went through the edges of the chamber where the field is distorted due to the increased diameter of the outer sense wires and the dielectric material of the chamber frame itself.

The MWPC was constructed from four perspex frames, the two outer ones which held the 50 μm melinex windows being $\frac{1}{4}$" thick. The H.T. wires and sense wires were wound on the two middle frames, each $\frac{3}{8}$" thick (thus giving a cathode/sense-wire plane spacing of 9.5 mm) and in between which was an 'O' ring. The wire material for both planes was exactly the same as for previous chambers. The four frames were clamped together by brass OBA bolts, the seal between each middle and outer frame being made with twinstick.

Because no positional information was required from the chamber the sense wires were more widely spaced than normal at 0.5 cm. This meant less wires were required and also the chamber could be operated at a correspondingly lower voltage than with conventional 2 mm spacing. The resolution of the chamber was in no way impaired by this procedure; in fact tests showed that even up to a wire spacing of 8 mm the resolution remained about 25% at an energy of 6 keV, as shown in section 4.5, for 2.5 mm spacing. This is, however, to be expected since the average distance travelled by the positive and negative ions to their respective electrodes when the cathode/sense-wire plane spacing equals 9.5 mm is not significantly increased when the sense wire spacing is increased from 2 mm to 8 mm, and hence diffusion and capture of electrons is similarly not increased.

The large area of the chamber meant the sense wires had a fairly high capacitance to earth, about 350 pF in fact. The technique used here to separate the particle pulse from the X-ray pulse relies

upon the RC decay time of the chamber and amplifier being as small as possible; although it was now still less than the collection time of the electron component of the ionization in the chamber the high capacitance reduced the bandwidth of the amplifier. Consequently the width of an Fe^{55} X-ray pulse was greater than 7 nsec FWHM, with a corresponding reduction in height, and the efficiency of the system for separating particles from X-rays was severely reduced.

Therefore it was necessary to divide the sense wire plane into three equal sections. To produce an adequate pulse height from the chamber while it was still operating in the proportional region each section was operated from a pair of cascaded amplifiers, the outputs of which were summed, as in figure 6.1.

If two current amplifiers identical to that of figure 4.7, each with a gain of 50, were cascaded it was very difficult to prevent them from oscillating and it was necessary to reduce the gain of the first amplifier in each pair to 10 (by increasing R_2 to 100Ω) to achieve satisfactory operation. In addition the circuits were very sensitive to earth loops, again going into oscillation unless they were very carefully earthed at one point.

In order to restrict cosmic rays passing through the chamber to zenith angles greater than 82.5^{o} the two particle defining telescopes, A and B, were placed 240 cm apart, figure 6.2. The third scintillator telescope, C, acted as an anti-shower counter and was placed above B in the horizontal plane. Telescopes B and C and the proportional chamber are shown in the photograph in figure 6.3; telescope A is out of view on the left.

The electronic processing circuit was that shown in figure 4.9 with the addition that the anti-shower telescope provided a veto pulse to the coincidence unit between telescopes A and B. Apart from

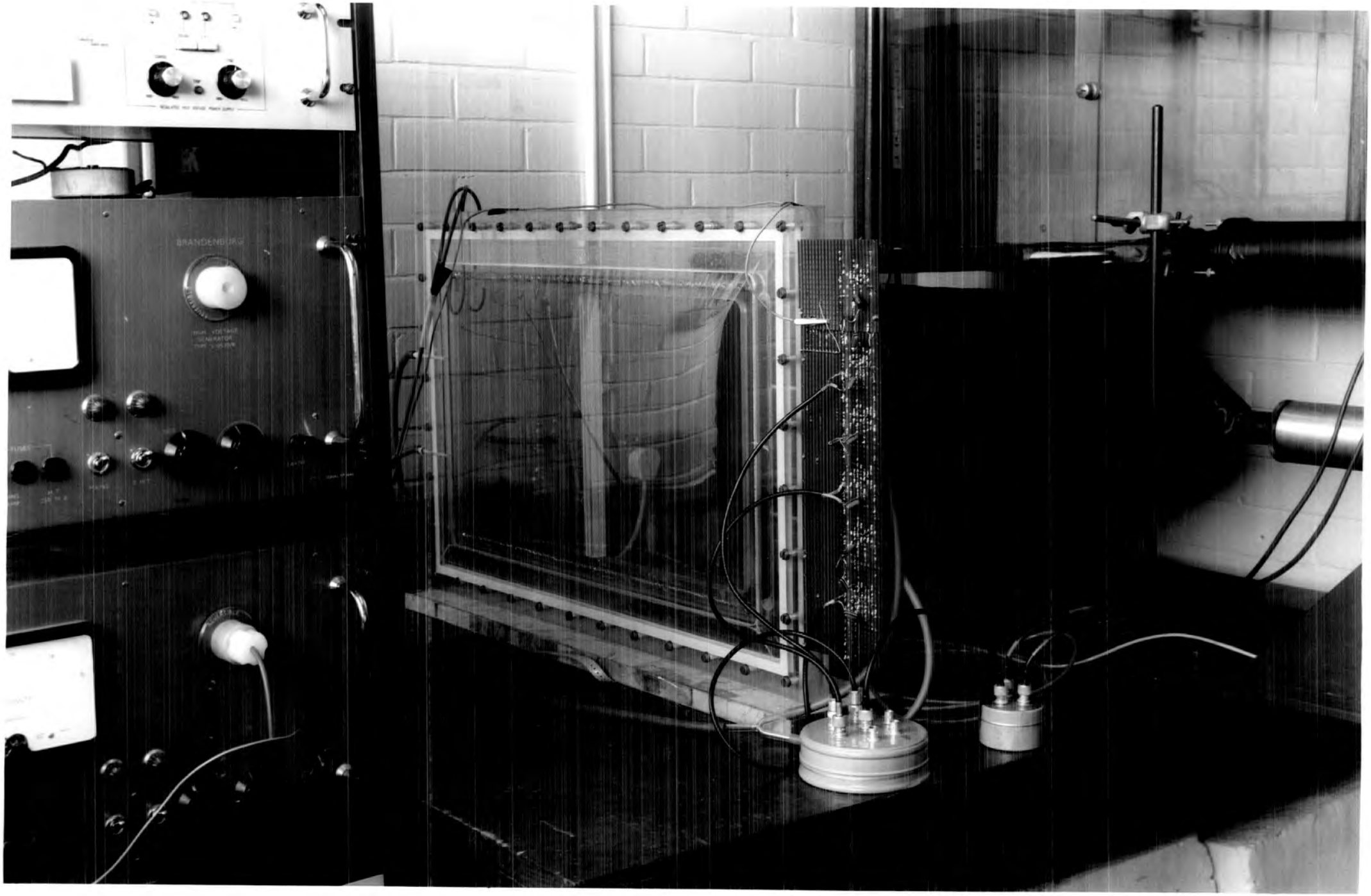
BRANDENBURG

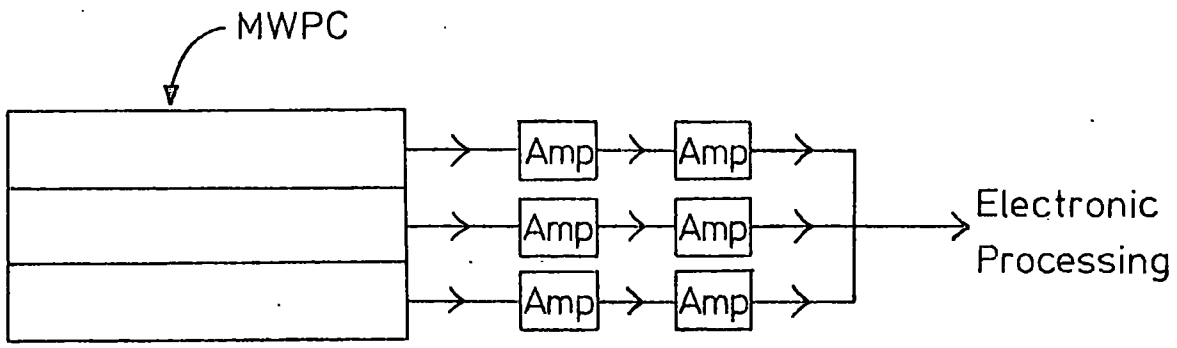

FIGURE 6.1 DIVISION OF PROPORTIONAL CHAMBER INTO THREE SECTIONS

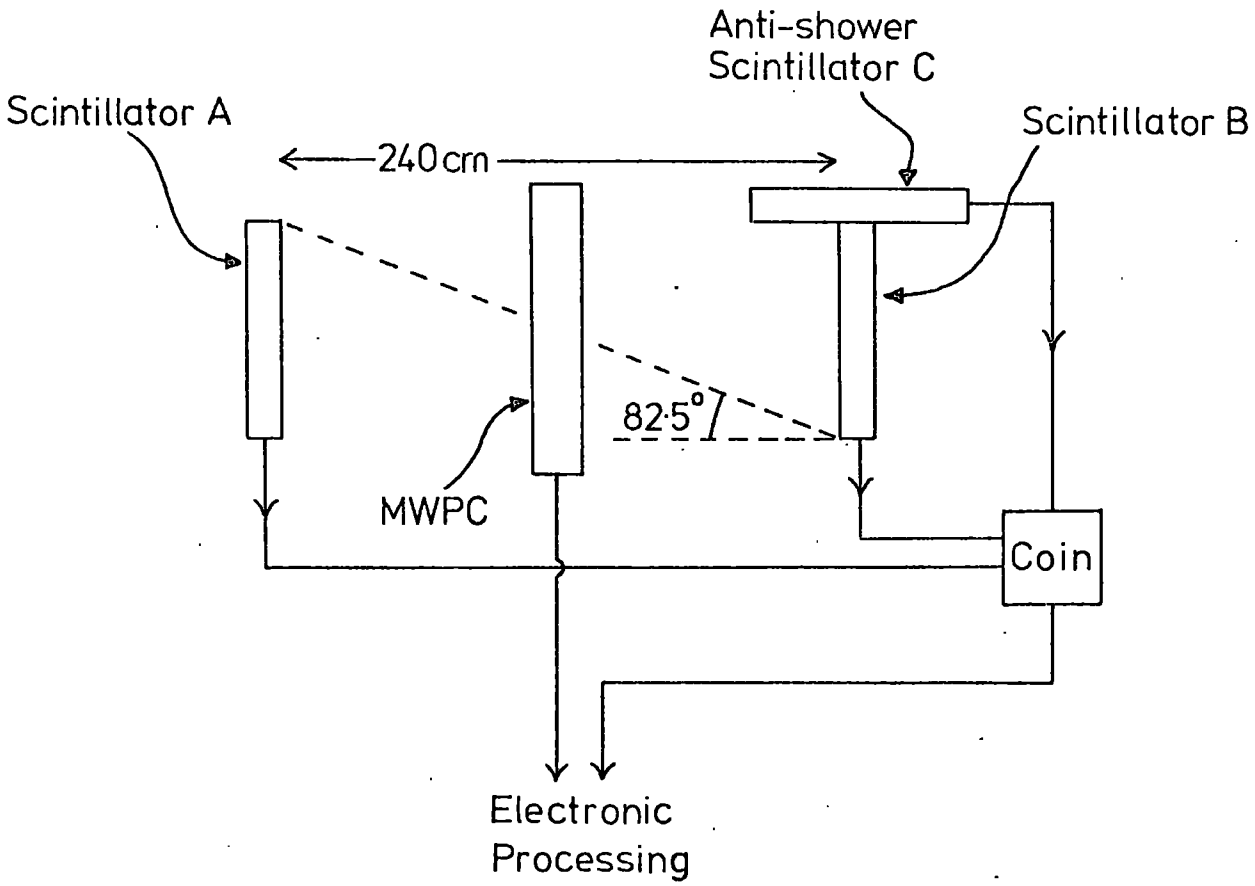

FIGURE 6.2 SIDE VIEW OF CHAMBER/SCINTILLATOR ARRANGEMENT

FIGURE 6.3 (OVERLEAF) PHOTOGRAPH SHOWING PROPORTIONAL CHAMBER AND SCINTILLATOR TELESCOPES B AND C

the current amplifiers attached to the chamber all electronics were in the form of modules manufactured by EG & G, the PHA a Northern Scientific type NS 900, and the scalers were made by Borer (Switzerland), type 613. The cathode-anode spacing on this chamber being 9.5 mm, the maximum electron collection time was about 240 nsec. with an electron drift velocity of 4 cm/ μsec so the scintillator coincident pulse was lengthened to 400 nsec to ensure no delta-ray or X-ray signal was missed, and the chamber pulse was delayed slightly so that it did not arrive at the coincidence to the scaler before the scintillator pulse. In addition both the chamber and scintillator pulses were delayed by equal times to ensure the veto pulse (which was 600 nsec long) started before (and ended after) the trigger pulse.

6.3 Transition radiator stack

It was concluded at the end of the last chapter that plastic foam radiator stacks are about half as efficient transition radiation producers as ones consisting of regularly spaced dielectric sheets. It was therefore thought wise to accept this 50% loss in signal and carry out the cosmic ray experiment with some kind of suitable plastic foam, rather than spend time in constructing a regular stack of melinex sheets, which would be quite an undertaking for this experiment because of the large area of the chamber.

Several samples of material, mainly various types of packing foam, were investigated with a travelling microscope; bearing in mind the need for the thicknesses of the two different dielectrics to exceed their respective formation zones polyurethane foam was found to be the best type of material. From a set of ten random measurements its structure had the following dimensions:

Wall thickness = (20 $\pm$ 7) μm

Average bubble size = (270 $\pm$ 40) μm

Since polyurethane is very similar in chemical composition and density to melinex it was assumed their formation zones would be almost identical. From the formation zone curves in figure 3.2 the foam wall size exceeds the formation zone for any energy upto a photon energy of 20 keV, the highest energy of interest in this experiment, but the bubble size (air) does fall below its formation zone for photon energies below about 6 keV and consequently there would probably be a very small loss in signal below this energy. However the most important factor with radiator stacks is to keep absorption in the solid dielectric to a minimum and for this reason polyurethane was chosen as the optimum material.

Two blocks of foam were used, one on either side of the chamber, since the muons were not uni-directional but could approach from either side of the chamber. The area of cross section of each block was sufficiently larger than the active area of the chamber to ensure that all particles would traverse the total thickness of each, which was 33 cm. Thus, assuming a wall/bubble combination to measure 290 μm, there were an equivalent number of foils of about 1140, representing a thickness of 2.3 gm cm^{-2}.

6.4 Experimental procedure

Discriminator 'A' into which pulses from the chamber amplifiers were fed, and the PHA, were calibrated as described in Chapter 4.

In this experiment the accumulation of data was very slow because of the low intensity of muons; in fact there were only 1.4 triggers per minute. Consequently it was necessary to run the experiment 24 hours a day and it was found there was often a day to

day variation in the discriminator threshold, up to 4% at the 6 keV level of 80 mV. The total variation over the whole experiment was 14%. Because of this it was necessary to carry out daily calibrations in order to keep an accurate check on the equivalent energy of each threshold setting.

During the experiment daily checks were also made to ensure that the gain of the chamber did not vary, by monitoring the channel number of the peak of the spectrum from the chamber of the Fe^{55} 6 keV X-ray.

The basic procedure was as in the last experiment. The delta-ray breakthrough rate was determined for runs without the stack at a range of threshold settings between 2.8 and 20 keV. Then the combined breakthrough and XTR photon rate was measured by carrying out runs with the polyurethane foam in position. The 'with stack' and 'without stack' runs were alternated daily. The CRT photograph in figure 6.4 is from an event where the current pulse from the chamber exceeded the preset threshold energy; it shows a large spike against the low level particle ionization and represents the detection of a possible transition radiation photon. It was taken during a run with a 4.1 keV threshold with the polyurethane stack in position. With reference to figure 4.9 the scope input was the output of the current amplifier, the scope being triggered from the coincidence between discriminator A and the scintillators; thus the trace is from a muon which caused a 9 keV current spike though it is not possible to say categorically whether this represents an X-ray or delta-ray. Similar runs were also made with approximately the same thickness of absorber as the polyurethane foam, but without the multitude of interfaces. Two slabs of perspex, equivalent in thickness to the polyurethane foam, were used for these dummy runs.

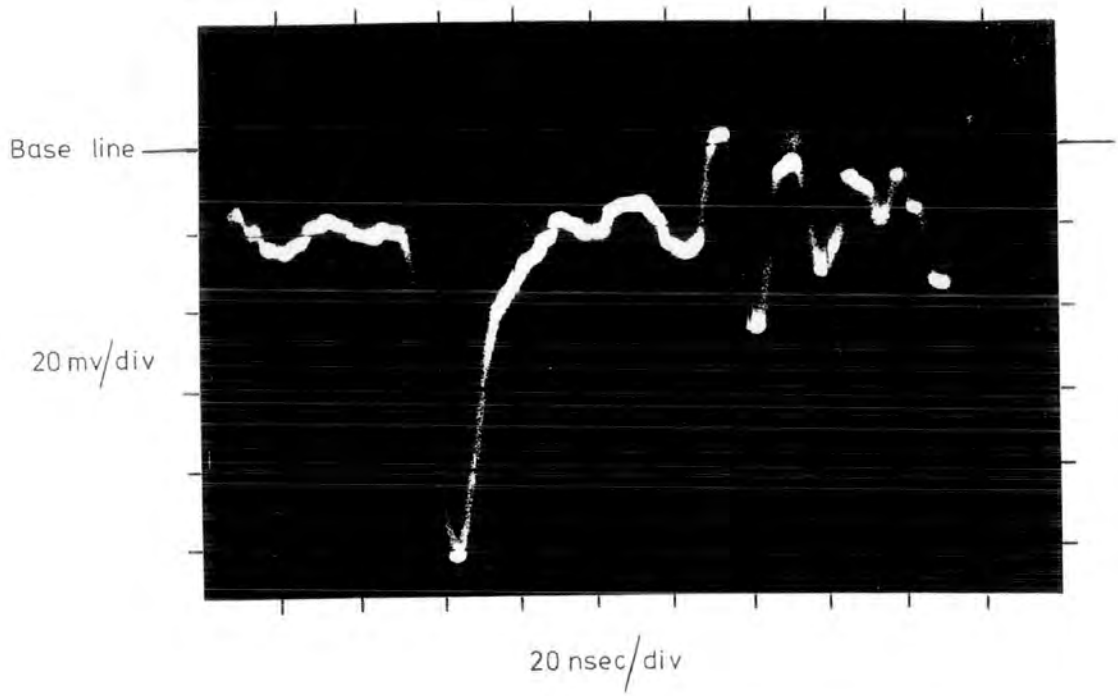

FIGURE 6.4 CRT TRACE OF A POSSIBLE TRANSITION RADIATION PHOTON

The gating pulse applied to the linear gate from the discriminator was 30 nsec.

6.5 Results

Figure 6.5 shows the integral spectra for delta-ray breakthrough (crosses) and the combined delta-ray and XTR photon rate (circles). Data was taken alternately with and without the radiator stack in position at the same threshold setting; the reason that corresponding points on each of the two spectra do not always coincide with the same energy is because of the fluctuations in discriminator threshold mentioned earlier.

Every point in the above figure corresponds to about 4000 triggers which, at 1.4 triggers per minute, is about two days data collection per point. The complete figure therefore represents about two months running. Data from further runs, in which the threshold of the discriminator varied by more than 4%, was not used.

The distribution of readings for each experiment in the preceding and present chapters was assumed to be binomial so that, if x events were recorded from a total of n coincidences, the absolute error on x was $\left[n(x/n)(1 - x/n)\right]^{\frac{1}{2}}$. The error bars in figure 6.5 are calculated from this term and it can be seen that below 11 keV there is a clear XTR signal above the delta-ray spectrum. Above 11 keV the errors on each spectrum begin to overlap and the two distributions gradually coalesce.

The lower curve in figure 6.6 shows the integral XTR spectrum from cosmic rays, which was obtained by direct subtraction of the delta-ray spectrum in figure 6.5 from the combined delta ray plus XTR spectrum; because the last two spectra are so close together the true XTR spectrum from this subtraction has negligible error due

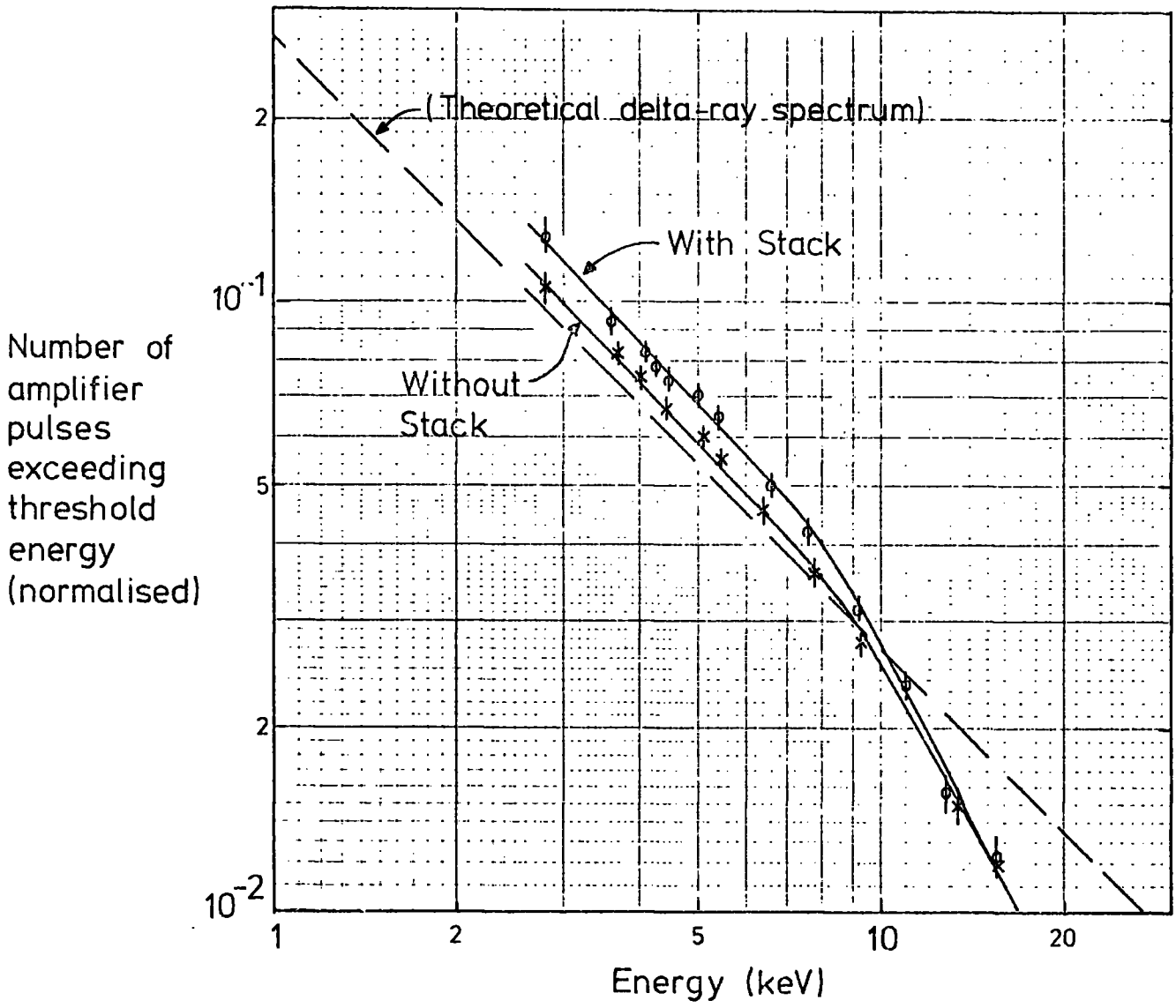

FIGURE 6.5 EXPERIMENTAL INTEGRAL DELTA-RAY AND (DELTA-RAY + XTR) SPECTRA DETECTED BY CHAMBER FROM MUONS

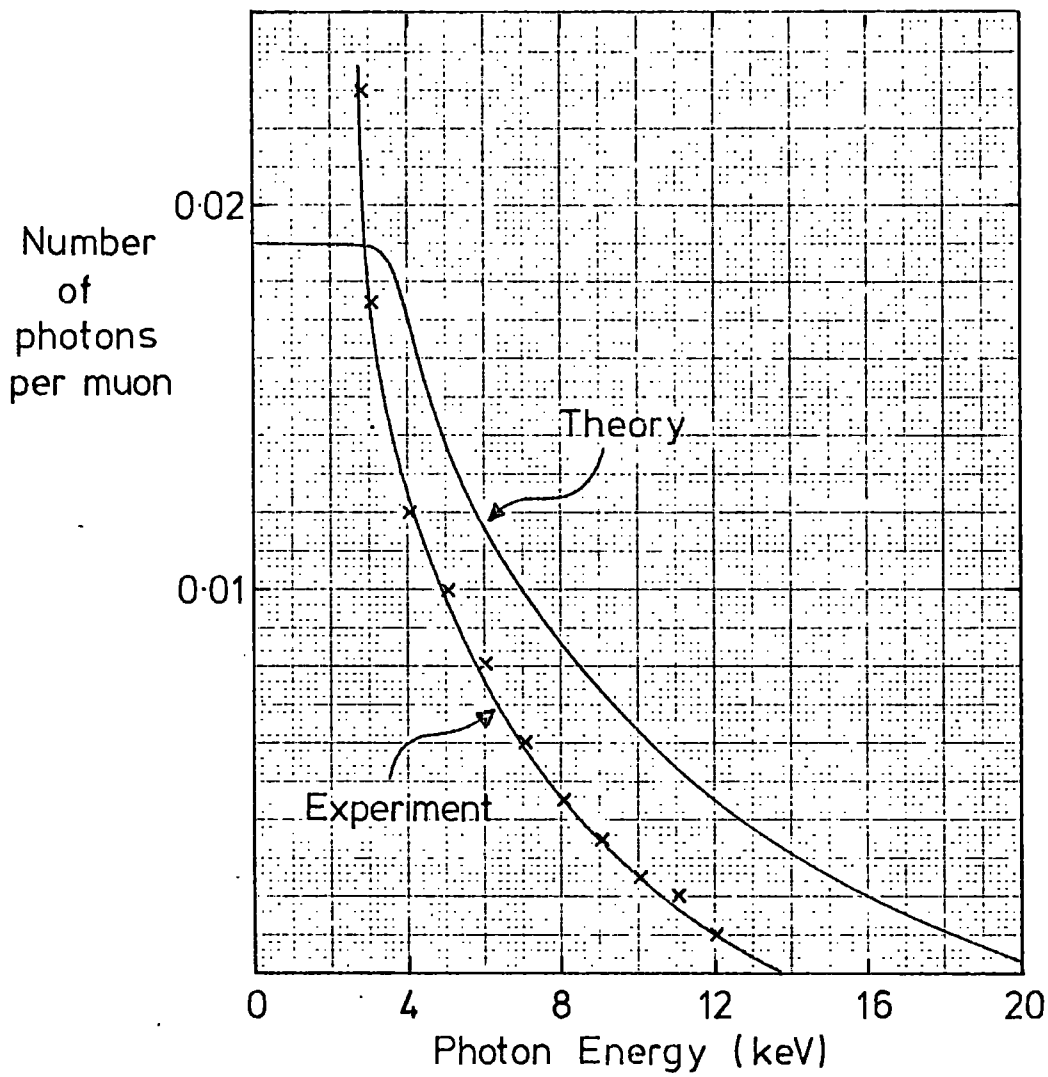

FIGURE 6.6 EXPERIMENTAL AND THEORETICAL XTR SPECTRA DETECTED BY CHAMBER FROM MUONS

to an X-ray and delta-ray pulse exceeding the discrimination level during the same event.

Figure 6.7(a) then shows the differential XTR spectrum derived from the above integral spectrum. Both this spectrum and the one in the last figure only go down to an energy of 2.8 keV as this represents the lower limit of the discriminator threshold.

The points in figure 6.5 were obtained from the ratio of the number of muon triggers accompanied by a signal exceeding the discriminator threshold to the total number of triggers, at each of the various threshold levels. However, besides registering this particular ratio each run also produced the pulse height spectrum of the above signals, i.e. the energy spectra of delta-rays and XTR photons, because each signal exceeding the discriminator threshold was fed into an integrator and the resultant pulse analysed in the PHA. Figure 6.8 shows the two spectra for runs with and without the stacks in position at the lowest threshold setting of 2.8 keV. Each spectrum is derived from 4000 triggers and it is clear that the spectra with the stack contains a larger signal than that without. Subtraction of the latter from the former gives the differential XTR spectrum detected by the PHA and is shown in figure 6.7(b). Thus both diagrams in figure 6.7 represent the same spectrum, the data for each being obtained in different ways.

Two further PHA spectra, one with the stack in position and one without, are shown in figure 6.9 for a threshold setting of 5 keV, where the delta-ray breakthrough is only 5.8% and XTR production about 1%. The two spectra are clearly less well separated than those of figure 6.8

Data taken from the runs with the polyurethane stacks replaced by their equivalent thickness of solid absorber show there

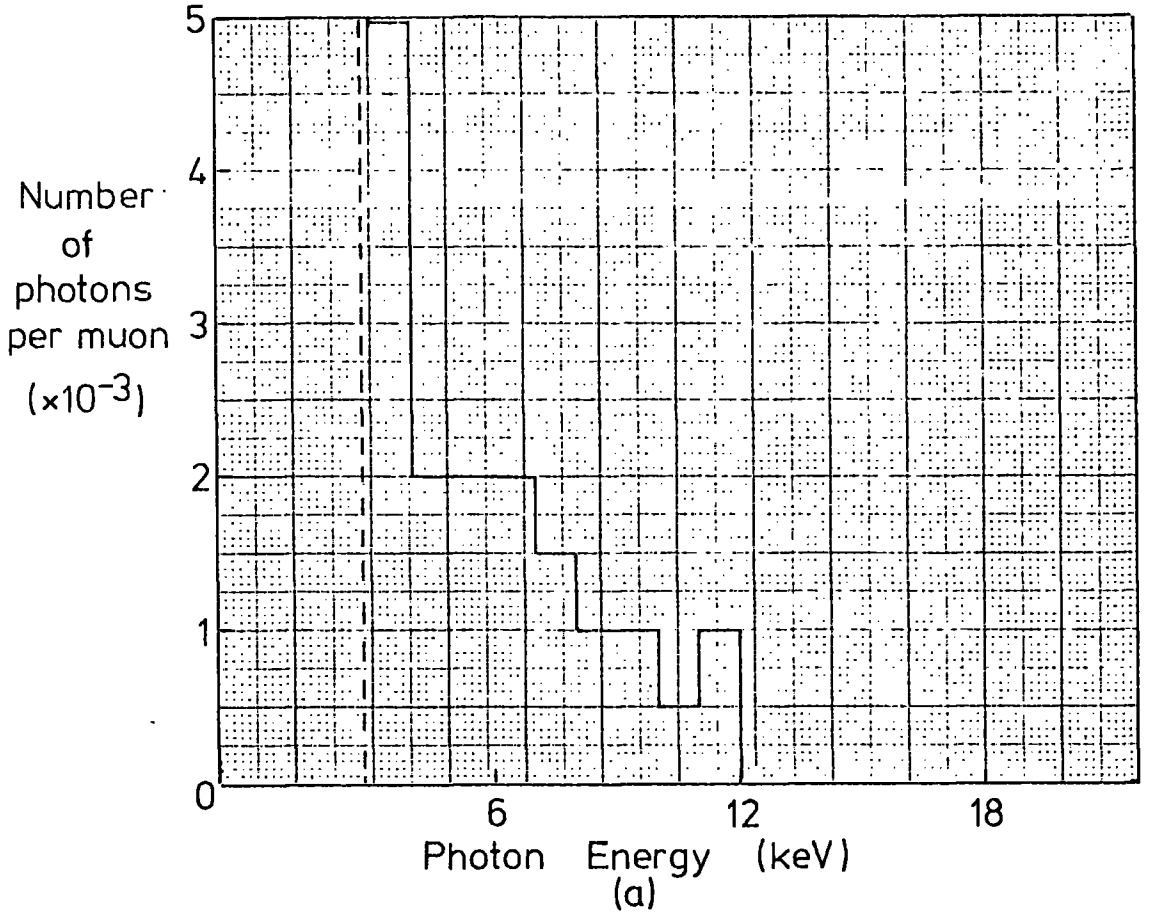

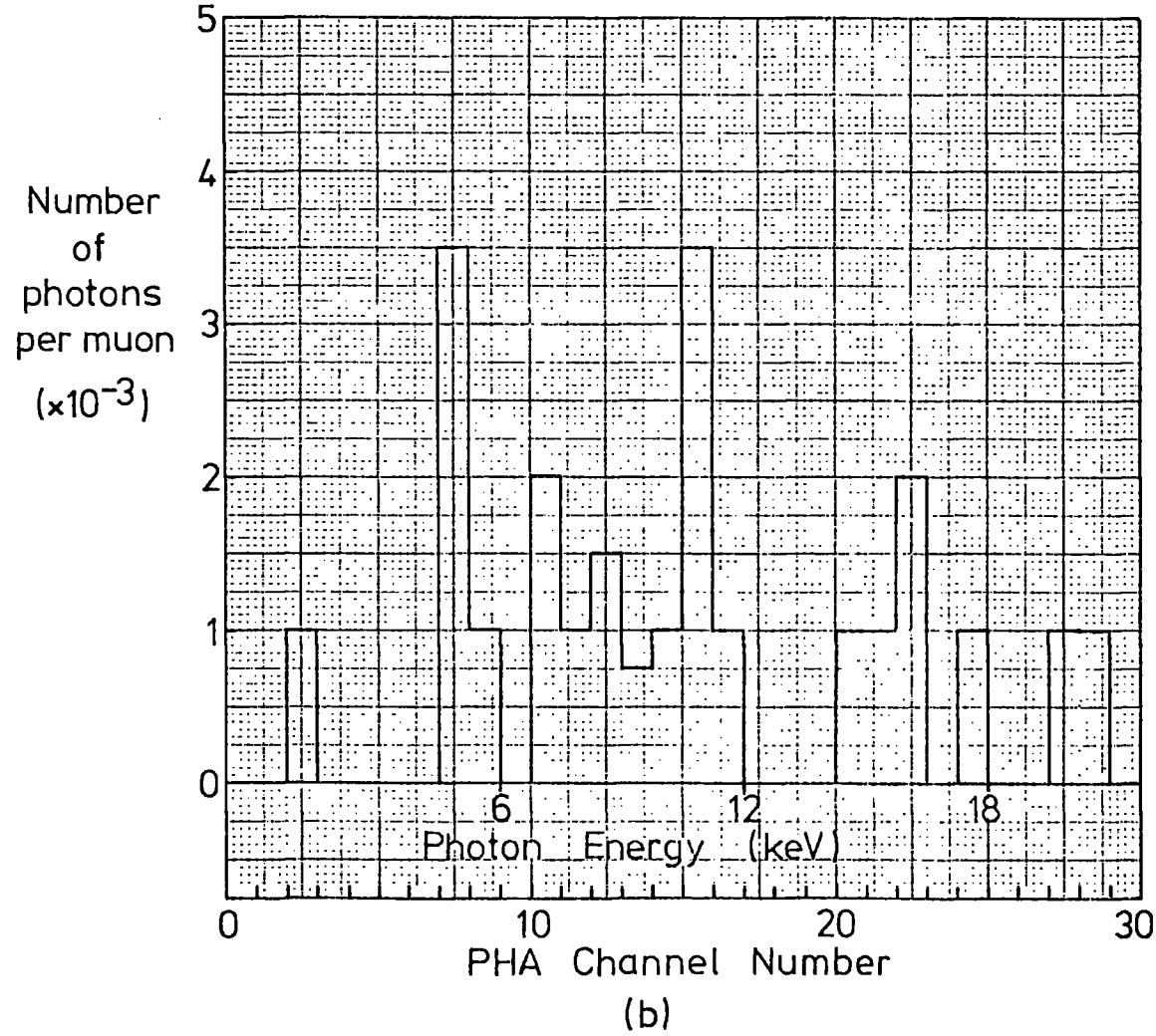

FIGURE 6.7 EXPERIMENTAL DIFFERENTIAL XTR SPECTRA DETECTED BY CHAMBER FROM MUONS

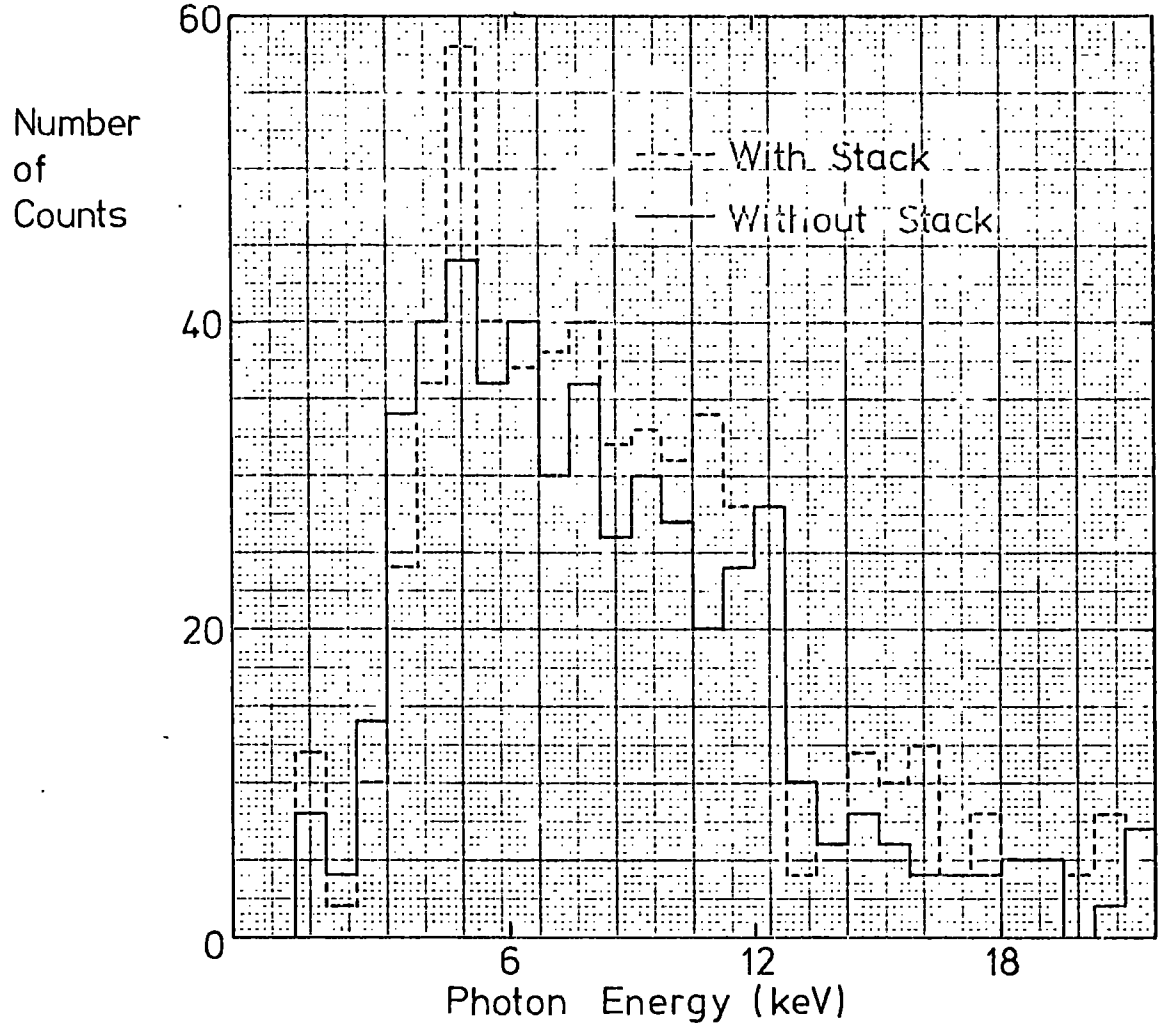

FIGURE 6.8 PULSE HEIGHT SPECTRA FROM 4000 MUONS WITH AND WITHOUT POLYURETHANE STACK (THRESHOLD = 2.8 keV)

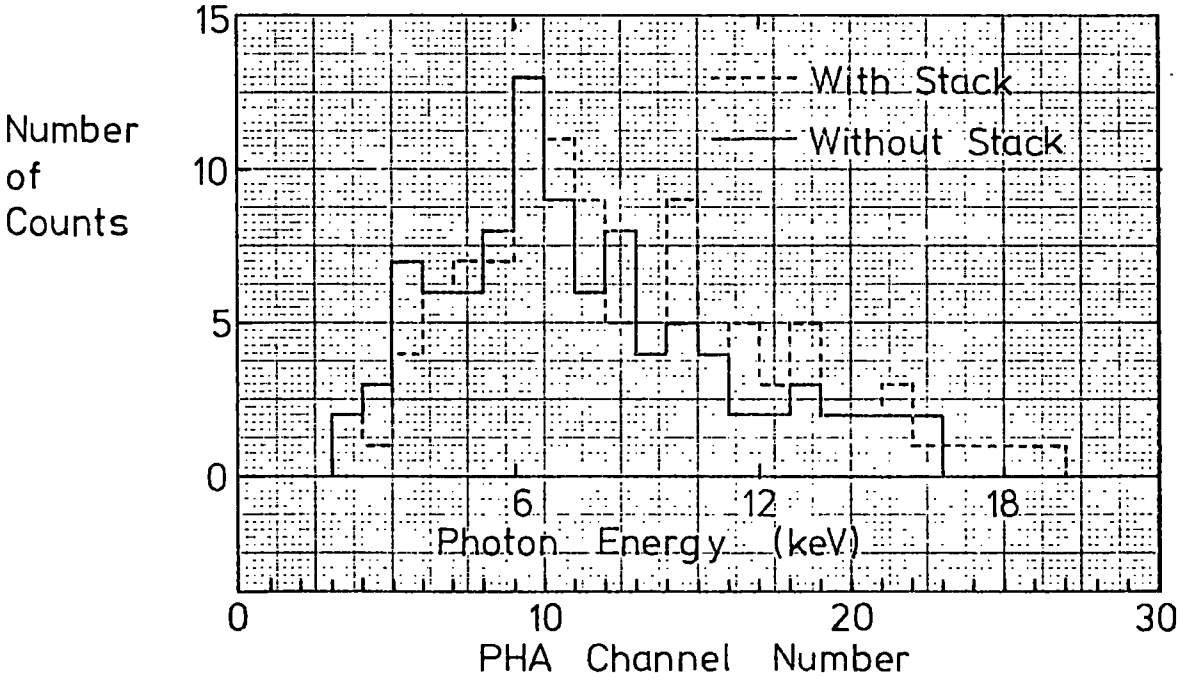

FIGURE 6.9 PULSE HEIGHT SPECTRA FROM 4000 MUONS WITH AND WITHOUT POLYURETHANE STACK (THRESHOLD = 5.0 keV)

was negligible production of knock-on electrons or bremsstrahlung in the stack; figure 6.10 shows the stack results again (circles) and the breakthrough obtained with the perspex absorber (solid circles). The curve through the latter points coincides almost exactly with that for the delta-ray spectrum in figure 6.5.

6.6 Discussion

6.6.1 Delta-ray spectra

A comparison of the three integral delta-ray spectra obtained so far show they are all very similar but with some small important differences.

The spectrum from Sr^{90} beta-particles, figure 4.11, and that from 1.5 GeV pions, figure 5.4, are almost identical in slope at all energies but the beta-particle delta-ray spectrum is displaced to a higher energy, relative to its predicted curve, by a factor of 1.9 ± 0.3 over the range 3 to 20 keV. This rather large difference can perhaps be accounted for by two main reasons:

i) It is possible that some of the beta-particle triggers are not, in fact, due to minimum ionizing particles but to those of a smaller velocity and hence greater ionizing power. Although an absorber was used in the Sr^{90} beta-particle experiment range straggling would still let a few low energy particles through.

ii) A considerable shift in the two curves would occur if there was a small difference in the discriminator calibration of both experiments, e.g. an under-calibration of one by 10% would lead to all points being shifted to a higher energy by an average of 30%.

The delta-ray spectrum from muons, on the other hand, though greater than the theoretical spectrum at low energies, has a smaller gradient than the other two experimental spectra up to 5 or 6 keV,

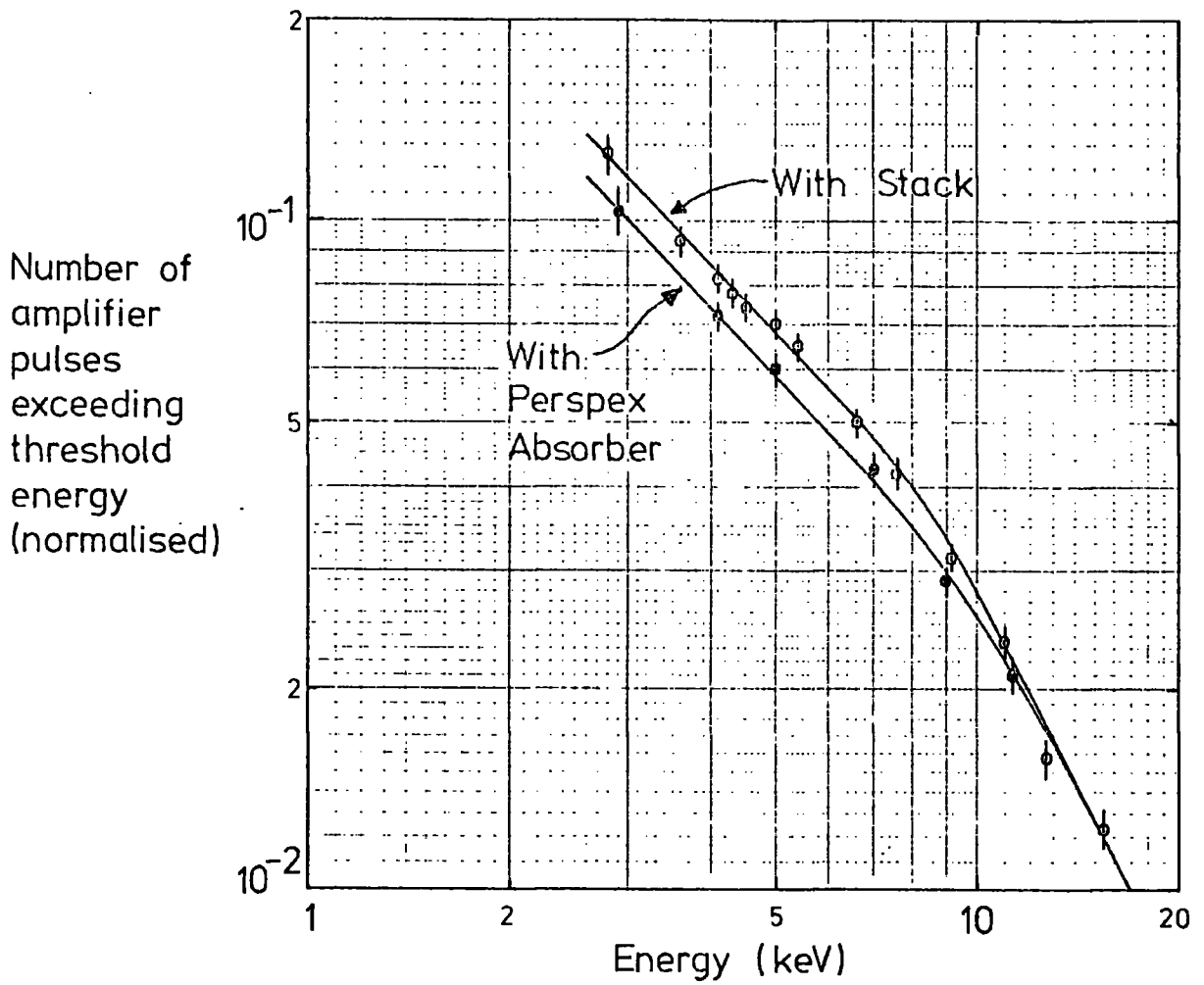

FIGURE 6.10 EXPERIMENTAL BREAKTHROUGH RATE USING PERSPEX ABSORBERS (AND DELTA-RAY + XTR SPECTRA FOR COMPARISON)

then falls away in a similar manner to the other two above this energy. This implies, since the spectra are integral, that fewer delta rays between 3 and 5 keV are produced here than with the beta-rays or pions, which should certainly not be so. Despite the grouping of the sense wires and the use of several current amplifiers in this experiment it is possible that the extra large capacitance in the large chamber could still be degrading analysis in this energy region but the analysis of transition radiation photons will not be affected since their spectrum is obtained by the subtraction process described in the previous section.

It was pointed out in Chapter 4 that, because a particle produces an almost constant low level distribution of ionization, the pulse from a delta-ray, or an X-ray creating ionization simultaneously with the particle, will not in fact start from the baseline (zero energy) of an oscilloscope trace but, on average, 0.5 keV above it. Since this has a much greater relative effect at low energies the signal recorded by the experiment should be higher than expected at low discrimination levels. This is therefore the major cause for the shape of the muon delta-ray spectrum which, up to about 8 keV, is shifted 0.3 keV to a high energy relative to the theoretical spectrum, and it would also partly explain the high breakthrough rate obtained with Sr^{90} beta-particles at low energies.

It was explained earlier that photoelectrons from 15 keV X-rays or greater have ranges in argon which are becoming comparable with the chamber thickness, and their corresponding current pulses become wider at the expense of height so that they cannot exceed the discriminator threshold for their particular energy. This, therefore, accounts for all three delta-ray spectra falling below the theoretical spectrum as the delta-ray energy increases.

6.6.2 X-ray Transition Radiation Spectrum

It has been found that there are 0.023 photons of energy greater than 2.8 keV detected by the proportional chamber for every muon traversing the radiator stack. Though this number is clearly too small to enable a measurement of the horizontal muon energy spectrum there are ways of increasing the photon flux and improving the technique, and these will be dealt with in the following concluding chapter.

It is useful to calculate the theoretical photon spectrum expected from a horizontal muon spectrum derived experimentally and compare it with the measured photon spectrum obtained here. MacKeown et al. (2) have measured the differential momentum spectrum of muons with zenith angles greater than 82.5^{o}, and their resultant spectrum is shown in figure 6.11. This spectrum was divided into eight cells, the average gamma of each one being taken at its mid-point energy. The number of particles in each cell was then determined by the area of each cell and the percentage of particles per cell is shown in row 3 of Table 6.1.

TABLE 6.1

Average energy of cell (GeV)	4.4	28.2	63.5	90	158	264	425	795
Average γ of cell	42	268	600	850	1500	2500	4000	7500
Percentage of particles	14.7	50.2	12.3	10.1	7.8	2.9	1.4	0.6
Adjusted percentage of particles	14.4	48.3	11.4	9.7	9.3	4.0	1.9	1.0

Unfortunately these figures do not represent the true energy distribution of particles passing through the chamber in this particular experiment because of a large landmass lying due south of the laboratory in which measurements were taken. The experiment lay

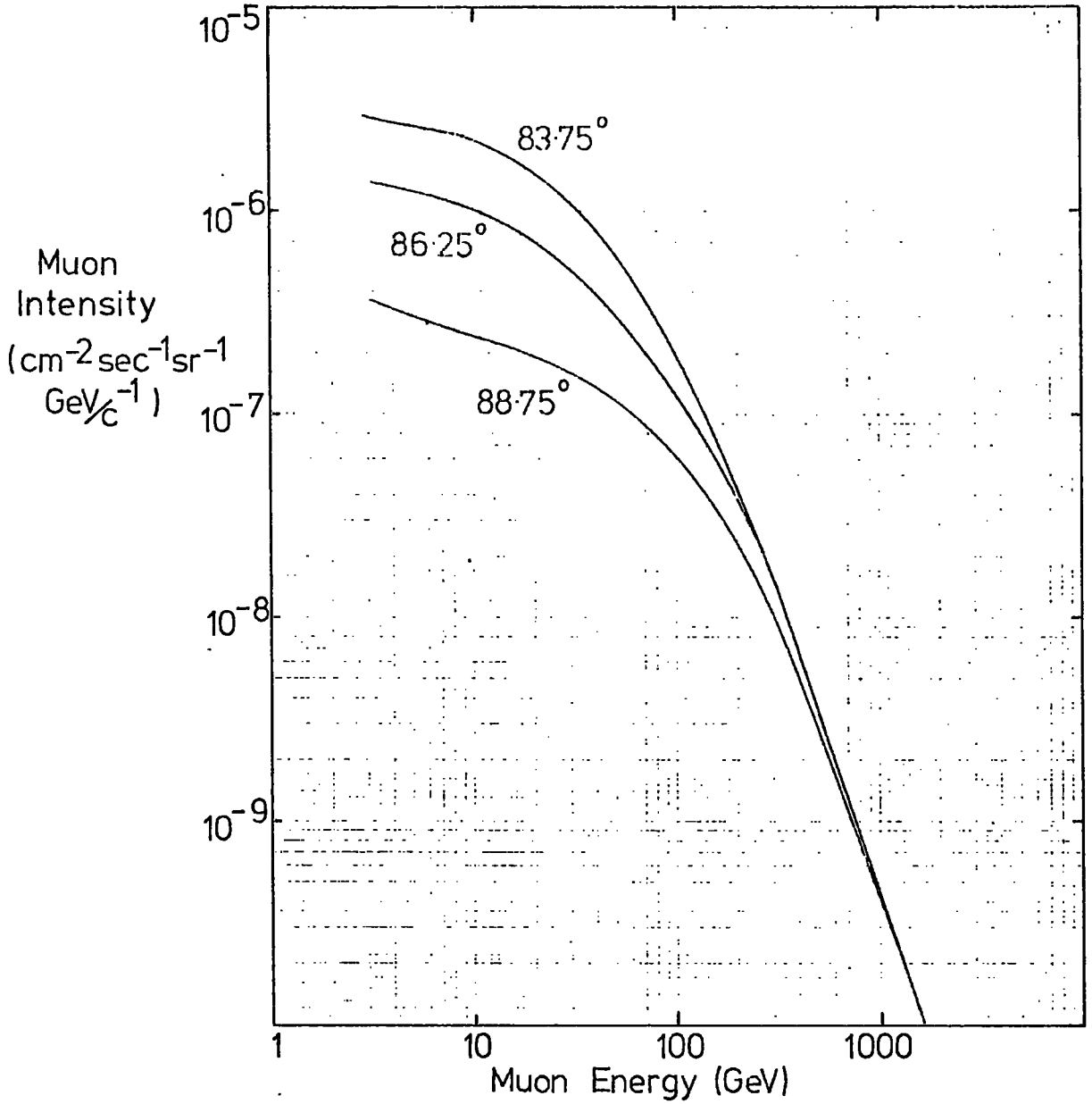

FIGURE 6.11 DIFFERENTIAL ENERGY SPECTRUM OF COSMIC RAY MUONS WITH ZENITH ANGLE > 82.5°

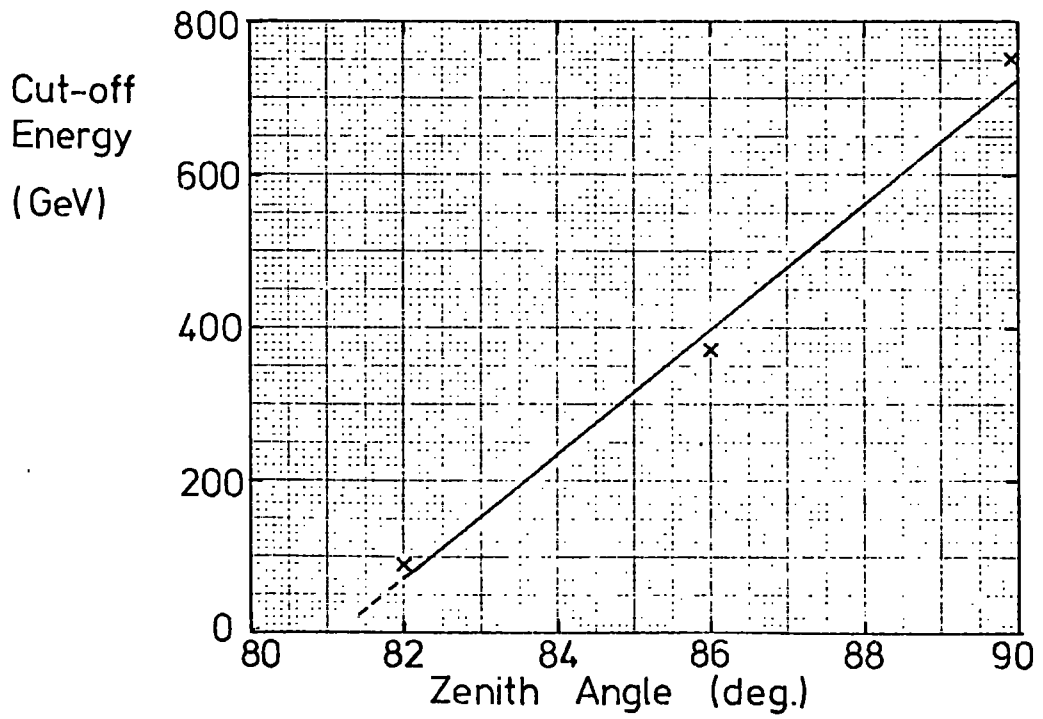

FIGURE 6.12 MUON CUT-OFF ENERGY AGAINST ANGLE OF INCIDENCE

in a north-south direction and only those muons coming from the north are represented by the above figures. The results of Mackeown et al. are corrected for the presence of the landmass but in his thesis (3) MacKeown calculates the cut-off energies for particles passing through the landmass: figure 6.12 shows a graph of cut-off energy against incident zenith angle. Even at 82^{o} the cut-off energy is 90 GeV so the great majority of particles from the south in the first four cells are entirely absorbed in the landmass. Taking account of the relative number of particles at each incident angle between 82.5^{o} and 90^{o}, the adjusted energy distribution of particles passing through the chamber from both directions is given in row 4 of Table 6.1.

This last row of figures was then computed in the same manner as for the 1.5 GeV electrons to determine the differential number spectrum of transition radiation photons they should produce when traversing a radiator stack, which in this case was assumed to consist of 1140 layers of polyurethane each 20 μm thick, the mass absorption coefficient being taken as the same as that of melinex (figure 3.4). The expected output was taken as half that given by the above computation for the reason given in Chapter 3, and experimentally verified in the last chapter, that a foam stack is roughly half as efficient as a regular one in producing transition radiation.

From the above analysis figure 6.13 shows the actual spectrum expected from the stack, and the spectrum which should be absorbed by the chamber, which was obtained by folding into the first distribution the absorption of X-rays in the 50 μm melinex window of the chamber and absorption in the chamber gas itself. Also shown on the diagram are the total number of photons involved and their total energy.

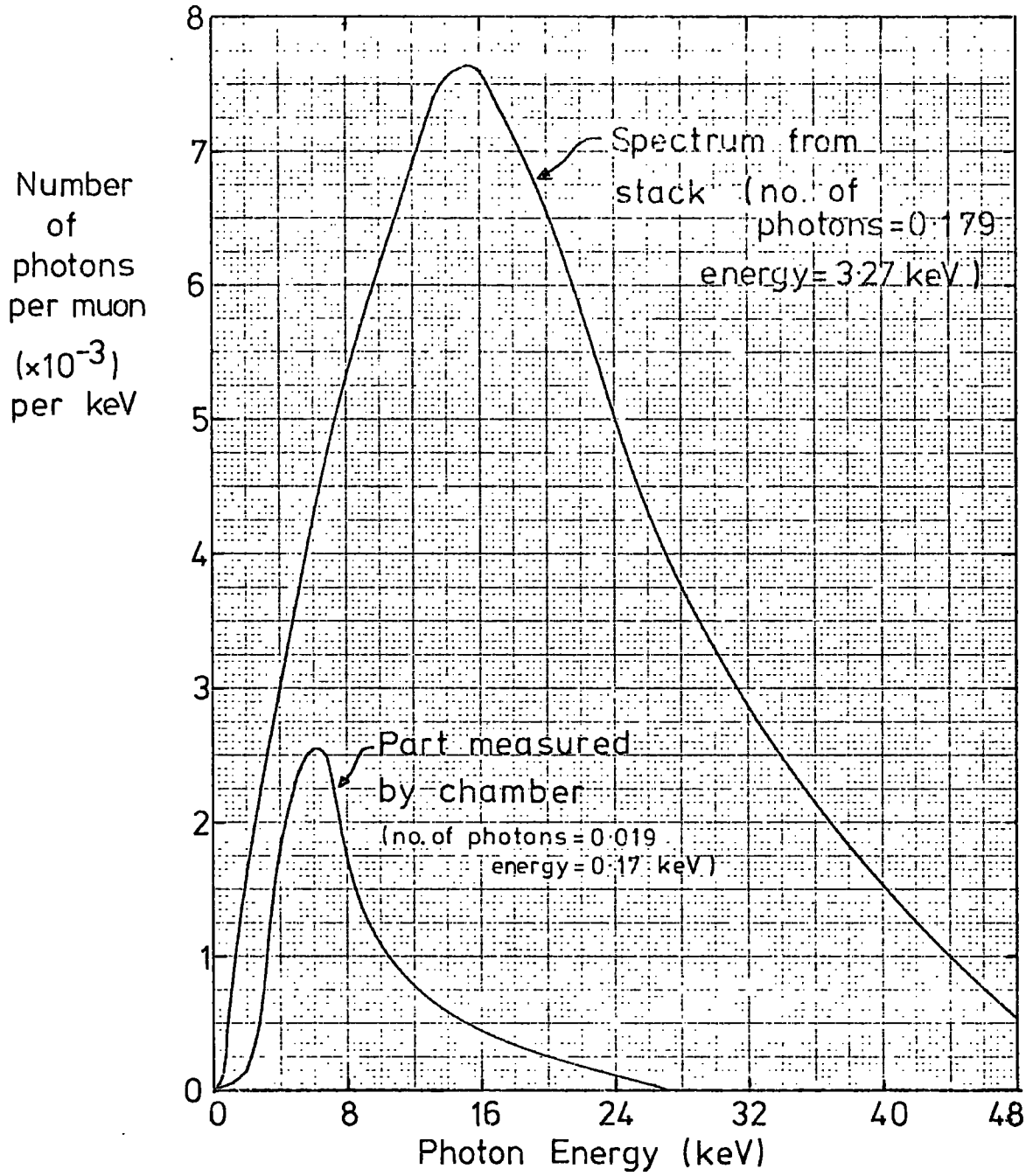

FIGURE 6.13 THEORETICAL DIFFERENTIAL XTR SPECTRA DIRECT FROM POLYURETHANE STACK, AND THAT MEASURED BY CHAMBER, WHICH ARE CREATED BY MUONS

It can be seen that the total spectrum emanating from the stack peaks at just below 16 keV and still contains a considerable photon flux at 30 keV. However, the very small absorption coefficient of the argon chamber above about 20 keV means the theoretically measured spectrum only peaks at 6 keV, contains only about 11% of the energy of the total spectrum, and consists of 0.019 photons per muon. It can be compared with the experimental one in two ways:

i) The equivalent experimentally measured differential photon spectrum is shown in figure 6.7(a) and (b) where (a) was obtained from the scaler readings at various threshold levels, and (b) is that from spectra recorded directly by the PHA. Mainly because of the poor statistics neither of these show a true peak but the energy range they encompass compares very well with that of the theoretical spectrum, about 2.5 keV to 18 keV.

ii) Integration of the theoretical spectrum yields the upper curve in figure 6.6, which also shows the experimental integral photon spectrum. From the latter it would seem that the majority of photons are of very low energy, around 2 - 4 keV, since below the cross over point at 2.95 keV, the theoretical spectrum levels off and the experimental one still rises quite steeply. At 2.8 keV, the lowest threshold setting attainable in the experiment, the experimental photon signal is 0.023 ± 0.010 per muon, and the theoretical one is 0.019, which agree to within one standard deviation. However, it should be borne in mind that the theoretical spectrum is quite sensitive to the value taken for the well thickness in the foam stack. Figure 6.14 shows the relation between the number of photons theoretically measured by the chamber from the same 1140 layer polyurethane foam against its wall thickness. Below 10 μm and above 30 μm the predicted number no longer agrees with the experimentally measured number.

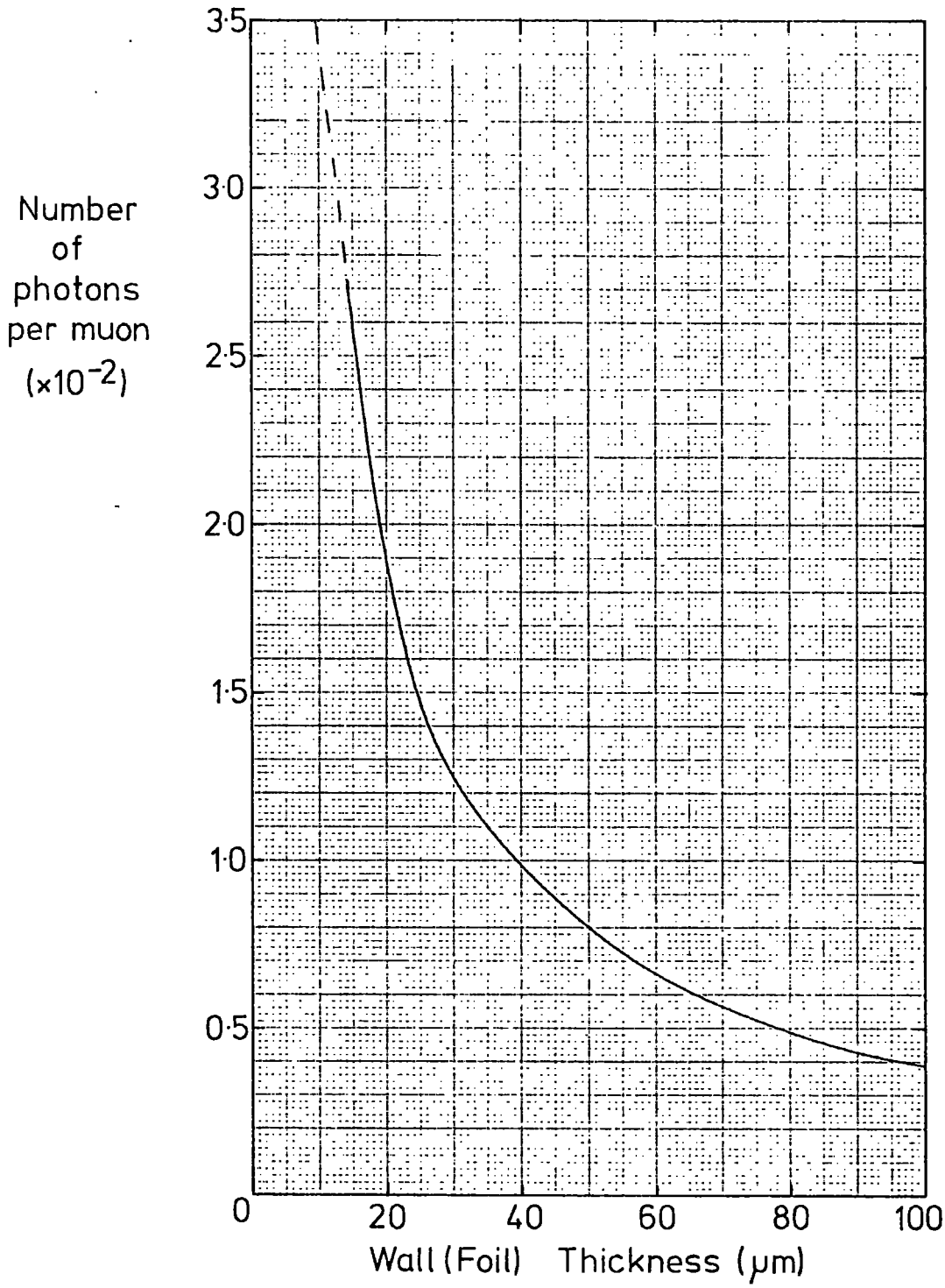

FIGURE 6.14 NUMBER OF XTR PHOTONS PER MUON AGAINST WALL THICKNESS OF POLYURETHANE STACK

Despite this reservation the results show that X-ray transition radiation has been detected from the horizontal component of cosmic ray muons and very good agreement is obtained with the theoretically derived photon spectrum.

6.7 Related work

The only other known work involving the detection of X-ray transition radiation from cosmic rays is that by a Russian group who used cosmic ray muons with zenith angles between 73^{o} and 90^{o}, the energy range being 700 - 6000 GeV (4). Their stack consisted of 300 layers of 200 μm thick paper, and X-rays were detected by a xenon gas scintillator detector, the absorption of X-rays being recorded by scintillation counters around the xenon detector. These allowed the number of photons per event to be measured, but not their energy. In addition the xenon scintillation detector only registered photons with energy greater than 35 keV, the electron binding energy in the xenon K shell and consequently only 77 events were recorded in a total running time of 5465 hours.

Therefore, comparison with the results of the cosmic ray experiment which has been the subject of this chapter is not really possible; nonetheless the latter has succeeded in detecting the soft component of X-ray transition radiation and suggestions for improvement will be made in the following, concluding chapter.

CHAPTER 6: References

1. G.Charpak, H.G.Fisher, C.R.Gruhn, A.Minten, F.Sauli and G.Pleh. Nuc. Inst. & Meth. 99, 279 (1972)

2. P.J.Mackeown, S.S.Said, J.Wolowezyk and A.W.Wolfendale. Proc. Int. Conf. Cosmic Rays, 964 (London 1965)

3. P.J.Mackeown, Ph.D. Thesis, University of Durham (1965)

4. F.R.Arutyunyan, K.A.Ispiryan and A.G.Oganesyan. Sov. Journ. of Nuc. Phys. 1, No. 5, 604 (1965)

CHAPTER 7

AN APPRAISAL OF THE DISCRIMINATION TECHNIQUE FOR TRANSITION RADIATION DETECTION

7.1 Proposed developments of present work

7.1.1 Introduction

It has been shown that there are basically two methods of detecting the X-ray transition radiation signal in MWPC's when high energy particles traverse a radiator stack:

i) The ionization deposited by the particle and the XTR it creates are integrated and an analysis of the ionization pulse height distributions with and without the stack shows there are more pulses at a higher energy with the stack, this being attributed to the absorption of XTR.

ii) The signal from the chamber is read out in current mode; in this way a particle pulse is a relatively low level one, whereas that of an X-ray of comparable energy to the particle ionization loss is quite large and narrow. A suitable threshold eliminates the majority of particle pulses but allows through the X-ray pulses.

In addition there has been a proposal (1) in which another pulse shape discrimination technique could be used with MWPC's for transition radiation detection, one which has been successfully used in reducing the particle background in X-ray astronomy with proportional counters (2, 3). It consists in measuring the baseline cross-over time after the output pulse from a charge sensitive amplifier attached to the counter has been doubly differentiated; this time is converted to a pulse height which gives rise time information, X-rays having short rise times and particles relatively

long ones. As yet, however, the technique has not been applied in this field but could no doubt be of benefit.

7.1.2 X-ray transition radiation from 1.5 GeV electrons

With the particular arrangement described in Chapter 5 it was possible, using an argon/methane filled MWPC, to obtain a maximum rejection ratio in separating transition radiation events from non-transition radiation ones of about 2.8, which occurred at a threshold setting of about 8 keV. The electron detection efficiency at this point was 2.8%. It is not easy to compare this directly with the integration technique since in that case one always gets a signal from the chamber after the passage of a particle, and because of the Landau distribution of ionization it is very difficult to say from this signal whetheran X-ray was detected or not. However, a very important method of substantially reducing the problem of the Landau tail will be described in § 7.2.

With the technique used in this work, if electrons are being separated from particles which don't produce radiation the registration of a pulse indicates a 2.8 greater probability that the particle was an electron than not. Clearly, though, ways of increasing the rejection ratio are needed:

i) The absorption of X-rays in the chamber obeys an inverse exponential law; thus halving the chamber thickness less than halves the number of X-rays absorbed but does reduce the breakthrough rate by a half. Therefore, reducing the chamber thickness should clearly improve the rejection ratio but will also reduce the detection efficiency.

ii) A gas filling is needed which has a greater overall X-ray absorption probability relative to particle ionization loss, a condition fulfilled by xenon and krypton. The photoelectric mass absorption coefficients of these two gases are shown in figure

7.1 (compiled from the same reference as that for argon, the coefficient of which is shown again here for comparison). Clearly xenon is better than krypton but the latter, although more dense than argon, does have the disadvantage that its coefficient between 3.5 and 14 keV is less than that of argon, because of the K absorption edge.

It was seen in Chapter 4 that the size of current pulse from an X-ray absorbed in an argon filled chamber was proportional to its energy up to about 15 keV, at which point non-proportionality began because the range of the photoelectron created by the X-ray was becoming comparable with the chamber width. The ranges of electrons in argon, krypton and xenon were given in figure 4.5; from this figure the corresponding X-ray energy in xenon at which the above non-proportionality should set in is about 30 keV. This also applies, of course, to delta-rays in xenon. Because of this it is possible to extend analysis in a xenon chamber to much higher energies than in argon, and consequently it is of value to predict the behaviour of a 1.6 cm thick xenon filled MWPC in the experiment with 1.5 GeV electrons.

Figure 7.2 shows such a chamber's detection efficiency, with due allowance made for X-ray absorption in the melinex window, calculated from equation 5.2, $I = I_o e^{-\mu dx}$, where μ and dx in this instance are the absorption coefficient of xenon and chamber thickness respectively. It shows clearly why xenon is a far better gas than argon for X-ray absorption, the maximum efficiency being over 90% and, apart from a small region from 35 to 42 keV, the efficiency remains above 10% even up to 60 keV, whereas in argon it drops quickly below 10% at 14 keV.

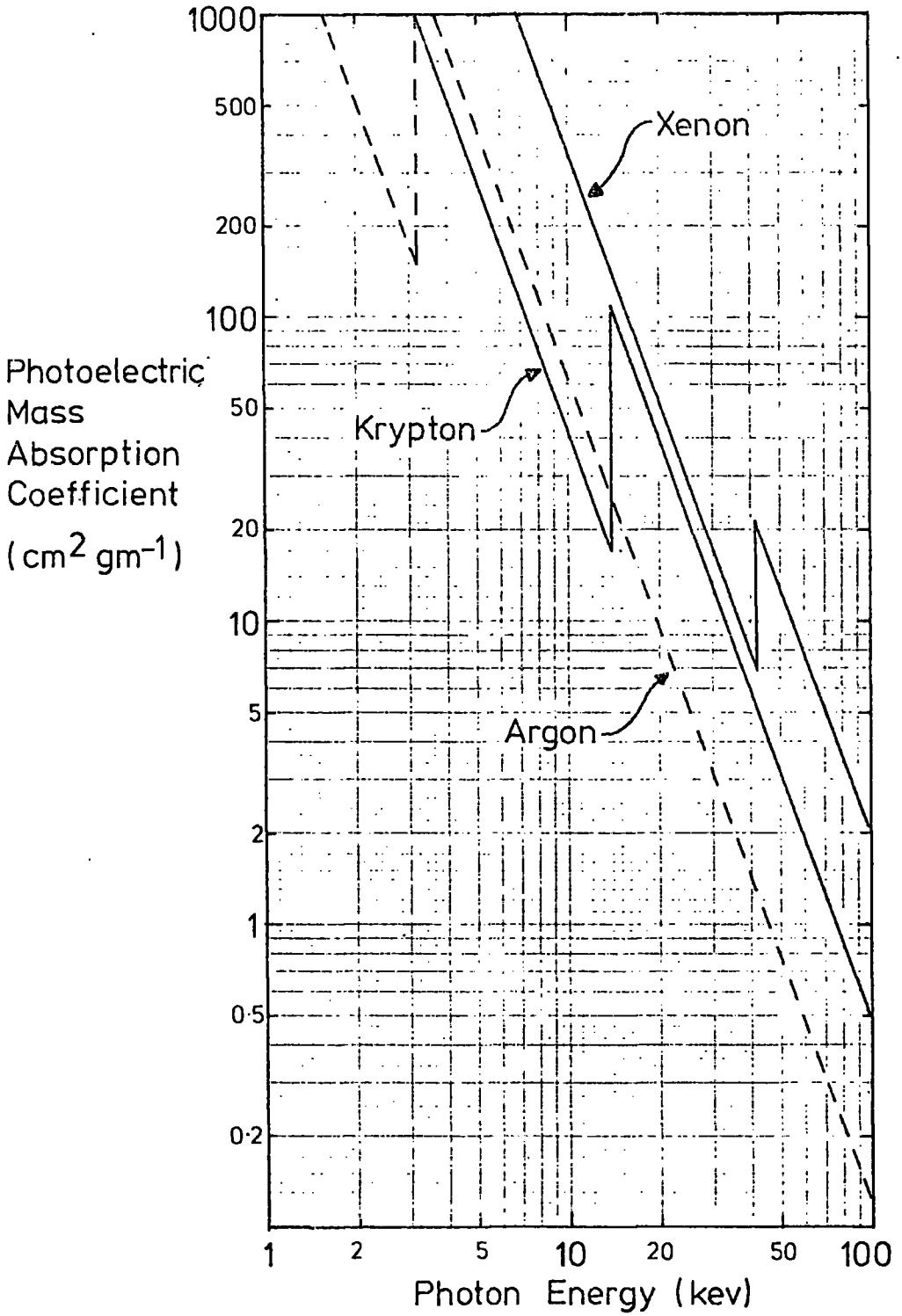

FIGURE 7.1 PHOTOELECTRIC MASS ABSORPTION COEFFICIENTS OF ARGON, KRYPTON AND XENON

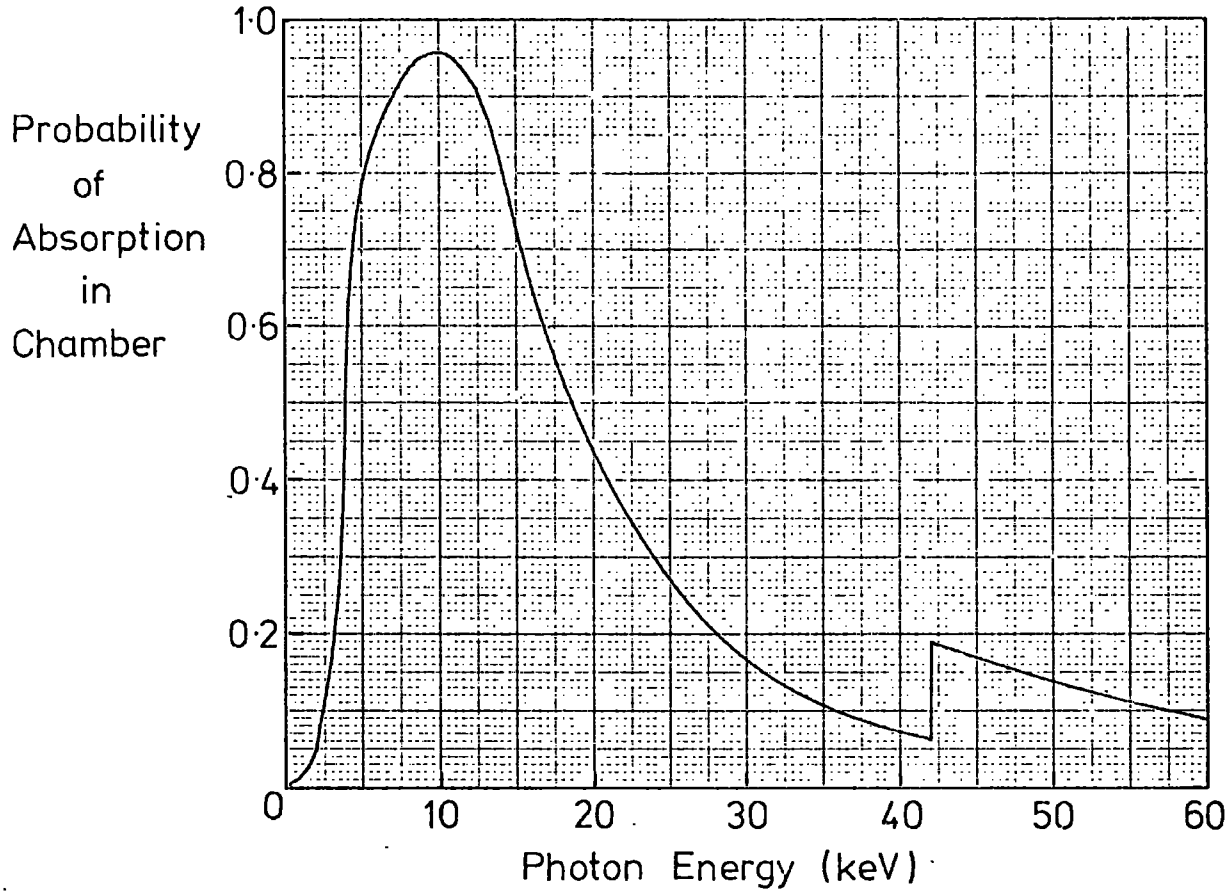

FIGURE 7.2 PHOTON DETECTION EFFICIENCY OF 1.6 cm THICK XENON PROPORTIONAL CHAMBER

The delta-ray breakthrough rate will increase by a factor over that obtained with argon of the ratio of the density of xenon to argon, i.e. 3.3, and is shown in figure 7.3. The integral XTR spectrum is obtained by folding the xenon chamber detection efficiency into the transition radiation spectrum emanating from the polythene stack, figure 5.2, and is also shown in figure 7.3 The analysis beyond 30 keV will be slightly in error because of the increasing photoelectron range above this energy. The absorption of all X-rays is dramatically increased, especially those above 10 keV, where the spectrum in argon falls away very rapidly. The rejection ratio now peaks at 20 keV (and also at about 40 keV because of the xenon absorption edge) but, more important, its magnitude is about 22, the overall electron detection efficiency at this point being 7.85%, of which only 0.32% is due to breakthrough. This is a big improvement on the 2.8% efficiency at the peak of the rejection ratio curve in argon, which occurred at 8 keV and was only 2.8.

It is possible to increase the detection efficiency with this technique by using more than one chamber in a chamber-radiator sandwich configuration, the chamber outputs being connected in parallel. Unfortunately the detection efficiency does not increase directly in proportion to the number of chambers because there is a probability that one chamber will register an output on the same event as another; if X = detection efficiency of one chamber for the desired particle, the efficiency, Y, of n chambers is given by

$$Y = 1 - (1 - X)^n \qquad 7.1$$

Therefore when X is small the detection efficiency does, in fact, approximate to n x X, the number of chambers times the single chamber detection efficiency.

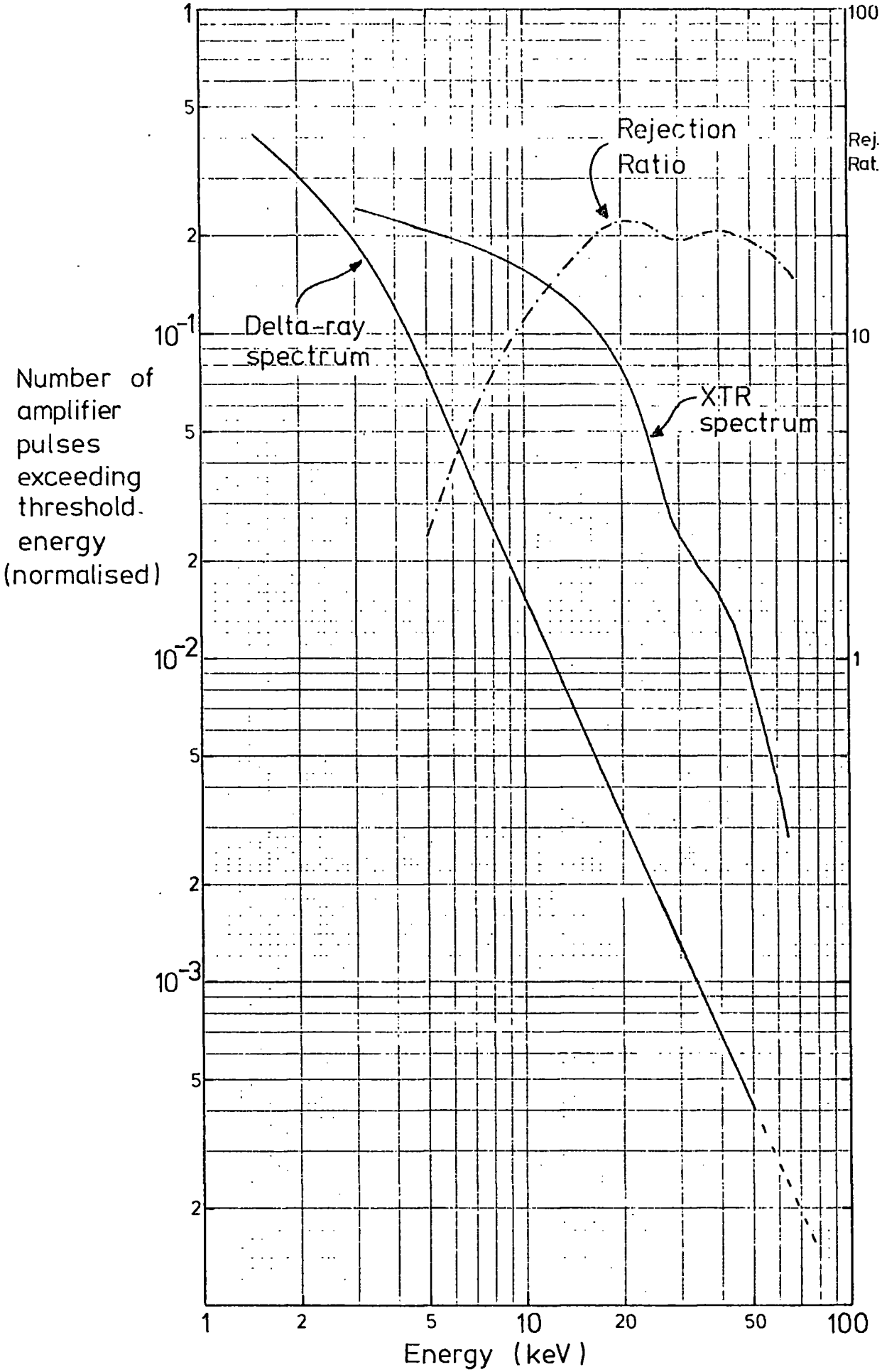

FIGURE 7.3 PREDICTED INTEGRAL DELTA-RAY AND XTR SPECTRA FROM FROM 1.5 GeV ELECTRONS DETECTED BY XENON CHAMBER

For comparison with a later section in this chapter an efficiency of 50% will be considered. For argon chambers the peak of the rejection ratio curve is at 8 keV, where X = 0.025. Thus substituting Y = 0.5 in equation 7.1, the number of chambers required becomes 27. The same equation can be used for breakthroughs, which increase to 20%, so that the rejection ratio remains the same. For xenon the number of chambers required is 10 and the overall breakthrough in this case is almost 3% so that the rejection ratio has dropped from 22 to about 17. Despite this these ten xenon chambers would provide an extremely efficient method of separating electrons from other (non-radiating) particles at 1.5 GeV. Particle separation can obviously be achieved at this energy simply by the use of magnets but the point of the above analysis is to show how useful this technique would be at higher particle energies where present-day magnets are of little use. In addition, however, more energetic electrons will produce a greater yield of XTR whereas breakthrough will remain relatively the same. The rejection ratio will therefore increase and the technique will become progressively easier since the number of chambers required to achieve 50% detection efficiency will be reduced.

7.1.3 XTR from Cosmic Rays

In the last chapter the lowest discriminator threshold setting of 2.8 keV gave a measured XTR photon signal of 0.023 ± 0.010 per particle, showing conclusively that transition radiation had been detected from cosmic ray muons. This figure, and the variation in the XTR rate as the threshold is increased, are too small to enable quantitative calculations on, say, the muon spectrum, but there are significant improvements which could be made.

Two alternatives of increasing the photon signal in the present cosmic-ray experiment are:

a) A series of argon/carbon dioxide chambers could be arranged to form an array of chamber-radiator sandwiches, as suggested for detection of 1.5 GeV electrons. If the outputs of the chambers were summed the absolute XTR signal would increase, e.g. a set of 10 chambers each with a threshold of 5 keV should, according to equation 7.1, produce an overall breakthrough signal of 0.45 per particle and a combined delta-ray and XTR photon signal of 0.50 per particle, thereby increasing the XTR signal to 0.05 per particle. At very low thresholds there would be a breakthrough for every particle so it would, of course, be necessary to investigate every threshold with different numbers of chambers. A suitable alternative to the latter would be to employ thinner chambers which, besides decreasing the breakthrough rate, would increase the ratio of photon rate to breakthrough rate since the absorption of X-rays varies exponentially, and energy loss of particles linearly, with gas thickness.

b) The use of xenon gas in only one chamber would also greatly improve the signal to noise ratio. In this respect it is thought that use could be made of the fact that when the interface thickness in a transition radiation stack becomes equal to the formation zone for a particle of particular gamma then the XTR output saturates and increases very little for particles of higher energy (4). Consider a stack of 1000 20 μm melinex sheets, each spaced 1 mm apart. Calculation of the photon flux from this stack for horizontal muons shows there would be 0.35 photons per particle, which are distributed among the energy bins selected in Chapter 6 as shown in Table 7.1.

TABLE 7.1

Average γ of bin	42	268	600	850	1500	2500	4000	7500
Total no. of photons from stack (0→30 keV)	0	0.006	0.012	0.024	0.080	0.082	0.074	0,072
Energy of these photons (keV)	0	0.06	0.14	0.34	1.32	1.56	1.54	1.60
No. of photons absorbed in xenon chamber (0→30 keV)	0	0.004	0.008	0.012	0.032	0.026	0.020	0.018
Energy of these photons (keV)	0	0.04	0.08	0.12	0.36	0.32	0.26	0.24

Also shown in this table are the number of these photons absorbed in a 1.9 cm thick xenon chamber placed directly behind the melinex stack (again only photons of energy up to 30 keV are considered in this analysis because of the increasing photoelectron range above this energy). The muon energy spectrum used still takes into account the effect of the landmass on the south side of the experiment.

If, for instance, the thickness of the foils in the stack were such that only half the photons for the bin with γ = 7500 were produced the photon number would be reduced by 0.009 to 0.111 per particle. A stack of even thinner foils with a formation zone below that for γ = 4000 would further reduce the photon signal by 0.010 to 0.101 per particle. Measurement of the photon signal loss in each case would allow an evaluation of the number of particles in each energy bin and, since the experiment in Chapter 6 was able to

detect a photon flux of 0.023 per particle with an absolute error of 0.010, the above calculated reductions in signal could be measured, though their errors would have to be reduced by longer run-times than used in Chapter 6; this procedure would therefore constitute an entirely different method of measuring the horizontal muon spectrum.

7.2 Related Work

When transition radiation is detected by collection of charge from a MWPC in integral mode a technique, first suggested in (1), has been developed which eliminates the troublesome Landau tail of the ionization loss distribution. This involves using the same chamber-radiator sandwich configuration used in § 7.1.2 but the outputs of the chambers, instead of being added, as described in Chapter 4, are fed into a device which measures their geometric mean. This has the effect of 'averaging out' the large energy transfer collisions in the Landau tail, the distribution approaching that of a Gaussian as the number of chambers is increased. The efficacy of this idea has been shown by Yuan et al. (5) and figure 7.4 shows the ionization distributions, one with and one without the 5.3" styrofoam transition radiators, from 10 GeV electrons traversing 10 chamber-radiator segments. The elimination of the Landau tail and consequent separation of the two distributions is just beginning.

Yuan et al., too, define a rejection ratio, which is the inverse of the fraction of the number of counts in the cross-hatched area of figure 7.4 by taking the detection efficiency of 50% for the desired particle. Figure 7.5 shows its dependence upon the number of chambers. Although this graph is for 10 GeV electrons and the

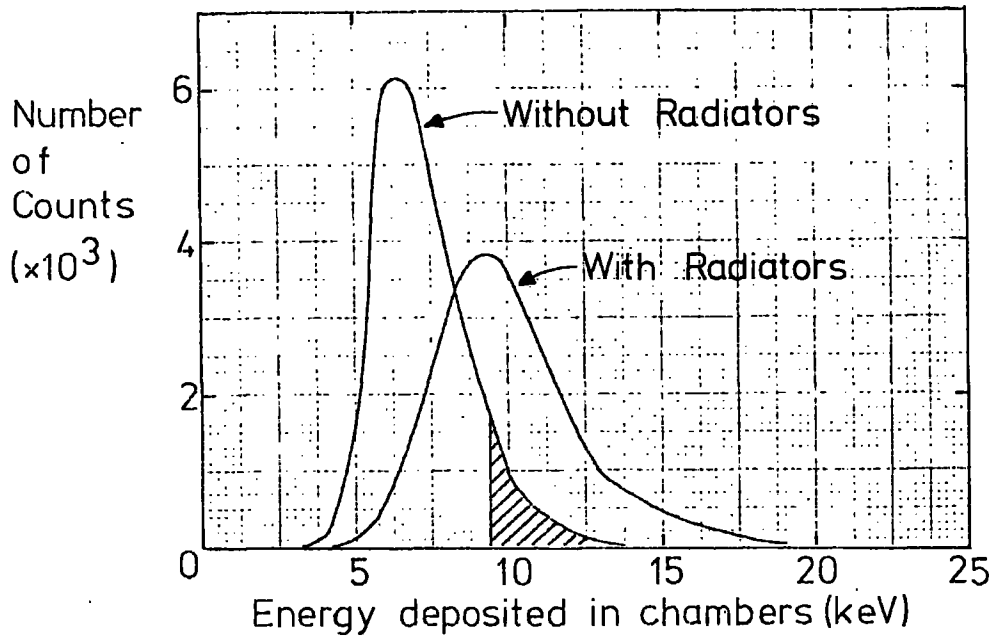

FIGURE 7.4 GEOMETRIC MEAN DISTRIBUTIONS OF IONIZATION FROM 10 GeV ELECTRONS USING TEN PROPORTIONAL CHAMBERS

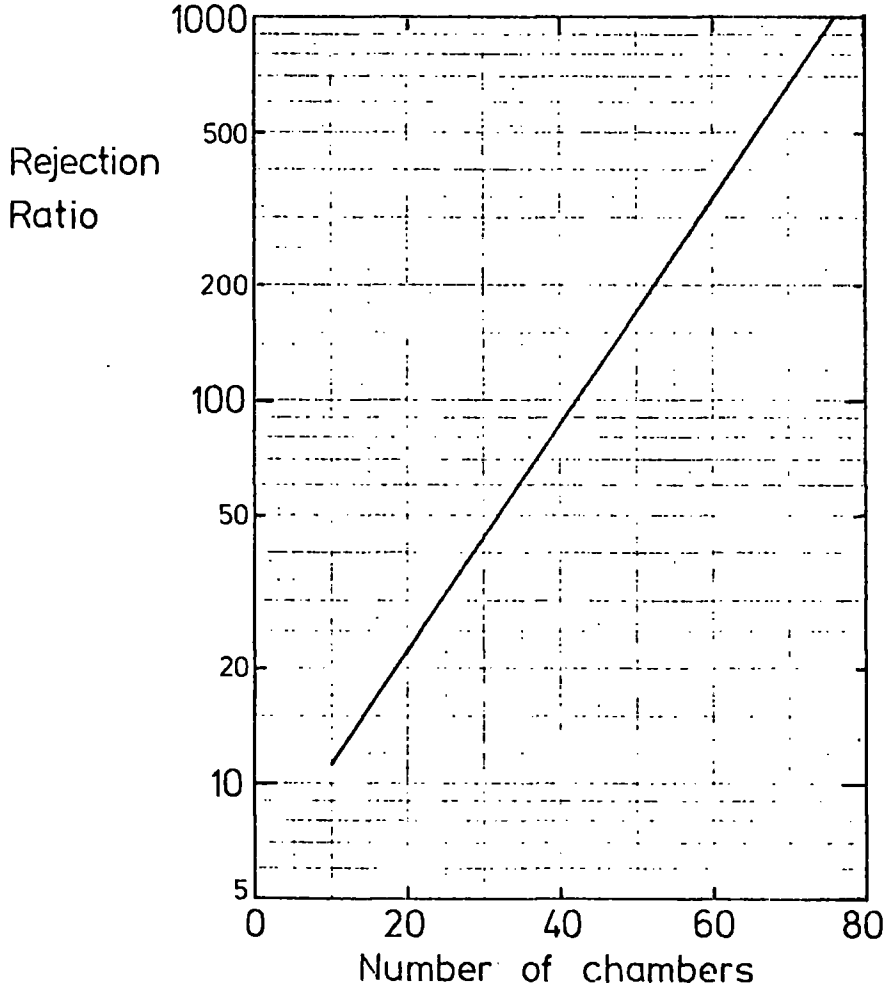

FIGURE 7.5 REJECTION RATIO AGAINST NUMBER OF CHAMBERS

work in this thesis involved 1.5 GeV electrons the difference in energy of the XTR they create in the photon range 0 to 20 keV (which is the only one of interest here since the chambers are filled with argon) is quite small: figure 3.6 and 3.7 show the XTR content of particles with γ = 1000 and 10,000 respectively, gamma values similar to those of the particles under discussion here. The photon energy from a 250 layer melinex stack in figure 3.6 is about 6 keV per particle. Yuan used 5.3" styrofoam radiators which, assuming an interface spacing of about 300 μm as for the polyurethane in Chapter 6, is equivalent to almost 450 interfaces, which should yield 12.5 keV per particle from a regular stack according to figure 3.7, or about 6.25 keV for the foam used in this case.

Therefore it is clear that Yuan's method produces a far greater rejection ratio than would be obtained by using a series of chambers with current amplifiers, e.g. for 27 chambers his rejection ratio is 35. This is simply because, with his technique, both detection efficiency and rejection ratio increase as the number of chambers increase, whereas the rejection ratio remains virtually constant in the other technique.

However the predicted results of a single xenon filled chamber attached to a current amplifier are very encouraging; at higher particle energies where the XTR increases in both flux and average photon energy, a single xenon chamber would give even larger rejection ratios at 50% electron detection efficiency.

Another technique, which utilizes the existence of the relativistic rise in the ionization loss of particles, has been investigated for separating relativistic particles of different masses (6) but this is somewhat restricted in that the relativistic rise eventually reaches saturation at very high energies because of the density effect.

7.3 Concluding Remarks

The technique of measuring transition radiation has been shown to have a great potential for separating relativistic charged particles. The detection process investigated in this thesis has produced useful and encouraging results, since not only has it been possible to experimentally differentiate between electrons and pions and to detect transition radiation from cosmic ray muons, but also the detected XTR rates are in good agreement with those predicted by theory. Emphasis has, of necessity, been placed on relatively low energy particles. However, chambers filled with a heavy gas such as xenon will undoubtedly play an important role in separating and identifying charged particles of a higher energy.

CHAPTER 7: References

1. H.Uto, L.C.L.Yuan, G.F.Dell and C.L. Wang. Nuc. Inst. & Meth. 97, 389 (1971)

2. E.Mathieson and P.W.Sanford. Proc. Int. Symp. on Nuc. Electronics, Paris 65 (1963)

3. P.Gorenstein and S.Mickiewicz. Rev. Sci. Inst. 39, No. 6, 816 (1968)

4. L.C.L.Yuan, C.L.Wang, H.Uto and S.Prunster. Phys. Rev. Lett. 25, No. 21, 1513 (1970)

5. L.C.L.Yuan, H.Uto, G.F.Dell and P.W.Alley. Phys. Lett. 40B, No. 6, 689 (1972)

6. Z.Dimcovski, J.Favier, G.Charpak and G.Amati. Nuc. Inst. & Meth. 94, 151 (1971).

APPENDIX I

a) Calculation of the electrostatic force between individual sense wires.

As shown in §2.3 the force between two wires which are a distance 'd' apart is:

$$F_1 = 2q^2/d$$

Figure A.1 shows a section along displaced sense wires. Consider the effect on wire 1 of the forces from all the wires to its right. The horizontal component of all the forces on it cancels with that from the corresponding wires on the left. The resultant force on wire 1 is therefore the vertical component of the forces from all the other wires.

Let u = sense wire displacement perpendicular to sense wire plane,

s = sense wire spacing,

and $d_{m,n}$ = distance from wire 'm' to wire 'n'

Then:

$$d_{12}^2 = 4u^2 + s^2 \approx s^2 \qquad (u \ll s)$$

$$d_{14}^2 = 4u^2 + 9s^2 \approx 9s^2$$

i.e. $$d_{1n}^2 = (n-1)^2 s^2$$

Thus, the vertical component of force of wire 2 on wire 1, for example, is

$$F_v = F_{12} \cos \theta_{12}$$

$$= \frac{2q^2}{d_{12}} \cdot \frac{2u}{d_{12}}$$

$$= \frac{2q^2}{s} \cdot \frac{2u}{s}$$

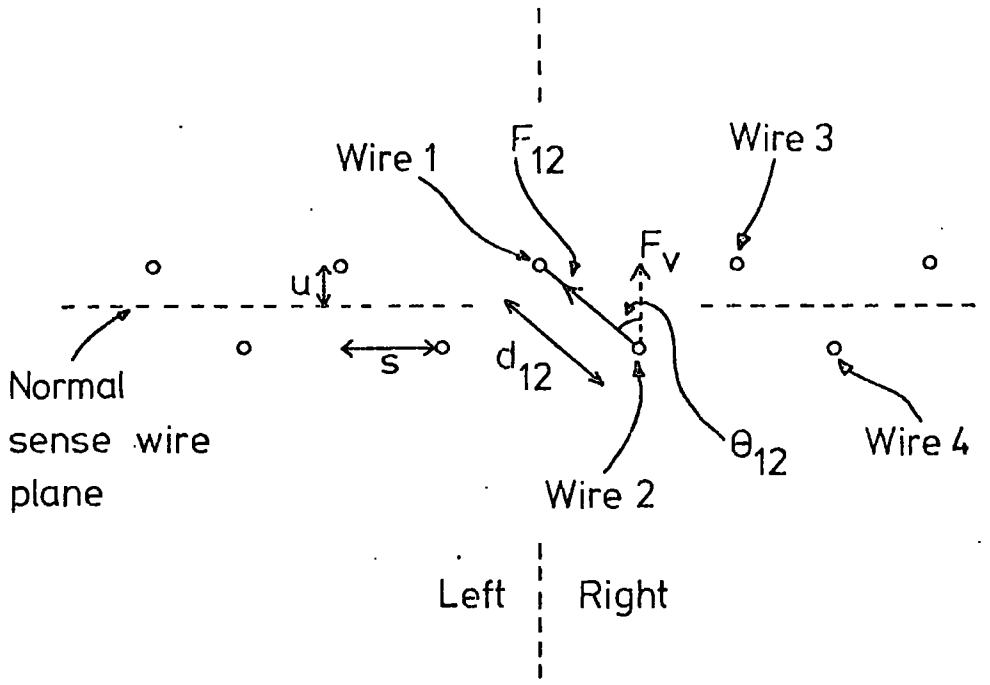

FIGURE A.1 SECTION ALONG DISPLACED SENSE (ANODE) WIRES

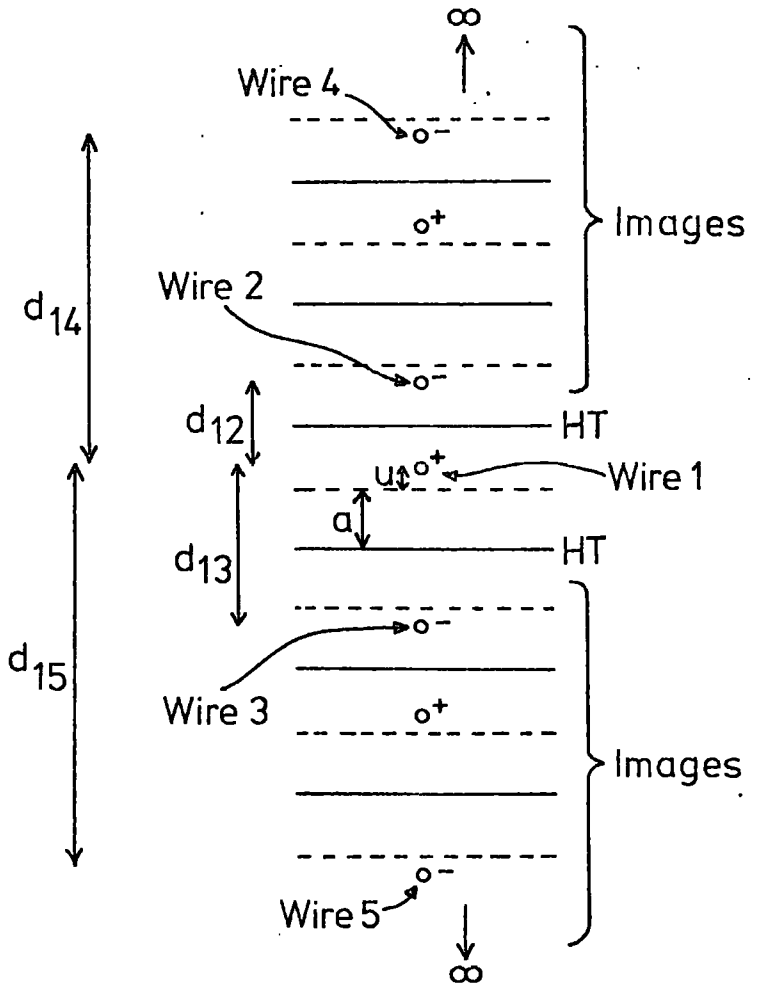

FIGURE A.2 IMAGE CHARGES CAUSED BY SENSE WIRE 1

Therefore the total force on wire 1 from all other wires to its left and right is:

$$F_2 = \sum_{n=2}^{\infty} F_{1n} \cos \theta_{1n} \cdot 2 \qquad \text{(n even only)}$$

$$= \sum_{n=2}^{\infty} \frac{2q^2}{(n-1)s} \cdot \frac{2u}{(n-1)s} \cdot 2 \qquad \text{(n even only)}$$

$$= \sum_{n=2}^{\infty} \frac{8q^2 u}{(n-1)^2 s^2} \qquad \text{(n even only)}$$

Now $\pi^2 = 8(1 + {}^1/_3{}^2 + {}^1/_5{}^2 \ldots)$

Therefore $F_2 = \dfrac{\pi^2 q^2 u}{s^2}$

b) Calculation of the electrostatic force between sense wires and the cathode plane

This calculation can be carried out by considering the infinite number of images of a particular sense wire which must exist to give a constant potential on both cathode planes.

Figure A.2 shows anode wire 1 with its corresponding image wires and charges in the two cathode planes. The forces on wire 1 from positive image wires cancel because corresponding wires on the left and right are equal distances away from it. However the negative image wires are asymmetrically placed with respect to wire 1 and therefore cause a resultant force on it.

Let u = displacement of wire 1 perpendicular to sense wire plane

and a = sense wire plane - cathode plane spacing

The distances from wire 1 to its two nearest negative image wires are:

$$d_{12} = 2a - 2u \,, \quad d_{13} = 2a + 2u$$

Thus the force on wire 1 from wires 2 and 3 is given by:

$$F_{23} = \frac{2q^2}{2a - 2u} - \frac{2q^2}{2a + 2u}$$

$$= \frac{2q^2 \cdot 4u}{4a^2 - 4u^2}$$

$$\approx \frac{2q^2 u}{a^2}$$

Similarly $d_{14} = 6a - 2u$, $d_{15} = 6a + 2u$, and

$$F_{45} = \frac{2q^2}{6a - 2u} - \frac{2q^2}{6a + 2u}$$

$$= \frac{2q^2 \cdot 4u}{36a^2 - 4u^2}$$

$$\approx \frac{2q^2 u}{9a^2}$$

and $F_{67} \approx \frac{2q^2}{25a^2} u$ etc.

Therefore total force on wire 1 is given by

$$F_3 = \frac{2q^2 u}{a^2} + \frac{2q^2 u}{9a^2} + \frac{2q^2 u}{25a^2} + \ldots$$

$$= \frac{2q^2 u}{a^2} \left(1 + \frac{1}{3^2} + \frac{1}{5^2} \ldots\right)$$

Therefore $F_3 = \frac{\pi^2 q^2}{4a^2} u$

APPENDIX II

Calculation of X-ray transition radiation flux from a radiator stack

Consider a charged particle of given γ traversing a stack of 'n' foils, each of thickness 't', figure A.3. Transition radiation will be created at each foil in the following manner. (For simplicity the medium around the foils will be assumed to be a vacuum).

1st foil: At the first interface a spectrum of photons, dN/dE, is produced, which undergoes absorption in the foil so that only a fraction $e^{-\mu t}$ are transmitted, where μ = linear absorption coefficient of the foil material. At the second interface a further spectrum dN/dE is produced so that the total X-ray flux emanating from the first foil is:

$$\frac{dN_1}{dE} = \frac{dN}{dE}\,(1 + e^{-\mu t})$$

2nd foil:

First interface : Spectrum of photons dN/dE is produced.

Second interface: This spectrum attenuated to $dN/dE\ e^{-\mu t}$

Further spectrum dN/dE is produced

$\frac{dN_1}{dE}$ attenuated to $\frac{dN}{dE}\,(1 + e^{-\mu t})\,e^{-\mu t}$

Thus the total XTR flux emanating from the second foil is:

$$\frac{dN_2}{dE} = \frac{dN}{dE}\,(1 + e^{-\mu t})\,e^{-\mu t} + \frac{dN}{dE}\,(1 + e^{-\mu t})$$

$$= \frac{dN}{dE}\,(1 + 2e^{-\mu t} + e^{-2\mu t})$$

3rd foil: Repeating the same procedure the flux emanating from this foil is:

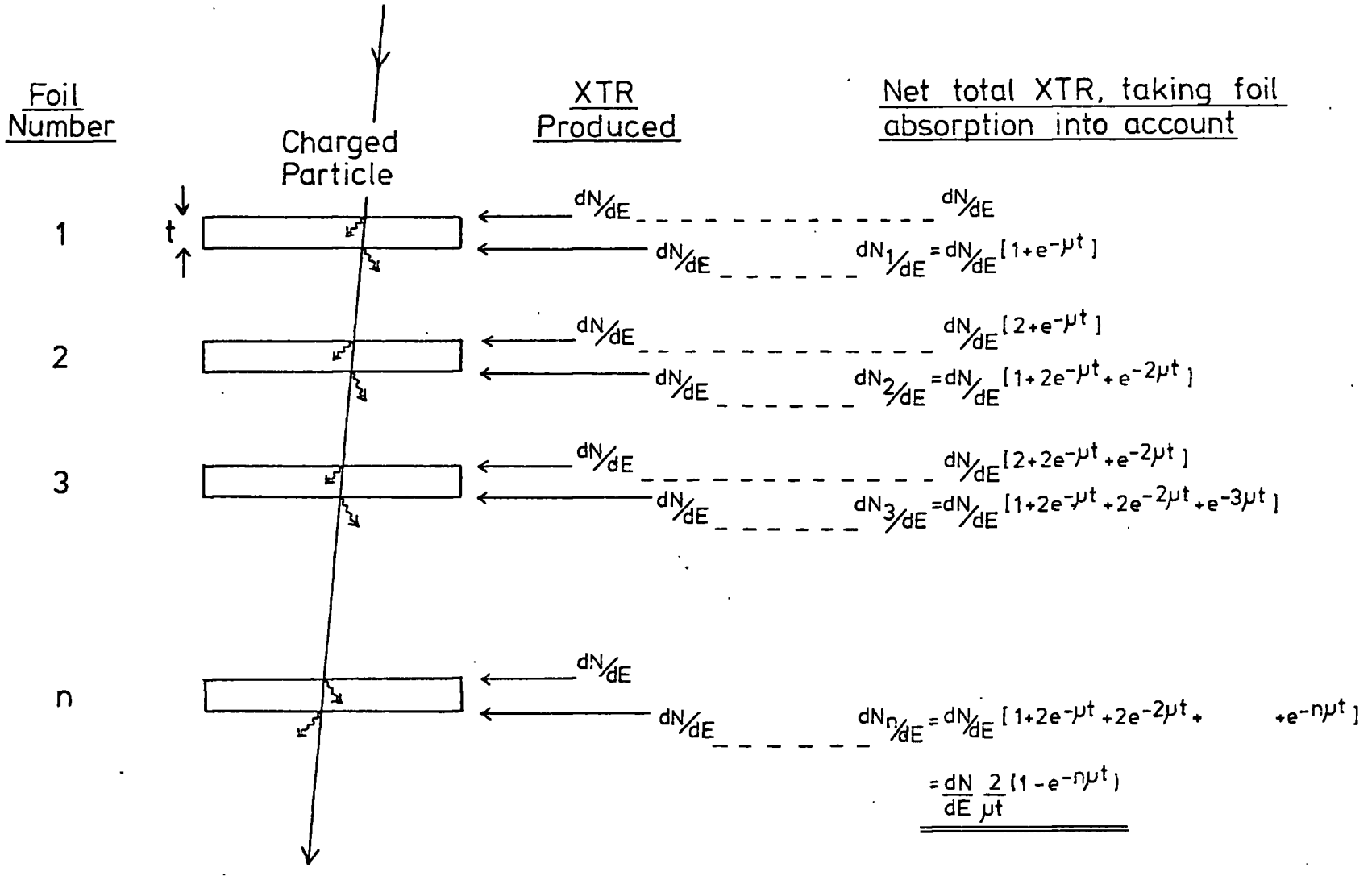

FIGURE A.3 CALCULATION OF TRANSITION RADIATION FLUX

$$\frac{dN_3}{dE} = \frac{dN}{dE}\left(1 + 2e^{-\mu t} + e^{-2\mu t}\right)e^{-\mu t} + \frac{dN}{dE}\left(1 + e^{-\mu t}\right)$$

$$= \frac{dN}{dE}\left(1 + 2e^{-\mu t} + 2e^{-2\mu t} + e^{-3\mu t}\right)$$

Thus for 'n' foils the output flux is:

$$\frac{dN_n}{dE} = \frac{dN}{dE}\left(1 + 2e^{-\mu t} + 2e^{-2\mu t} + \ldots + 2e^{-(n-1)\mu t} + e^{-n\mu t}\right)$$

Now $\dfrac{1}{1 - e^{-\mu t}} = 1 + e^{-\mu t} + e^{-2\mu t} + e^{-3\mu t} + \ldots$

$$\frac{dN_n}{dE} = \frac{dN}{dE}\left(1 + \frac{2e^{-\mu t} - 2e^{-n\mu t}}{1 - e^{-\mu t}} + e^{-n\mu t}\right)$$

$$= \frac{dN}{dE}\frac{\left(1 + e^{-\mu t} - e^{-n\mu t} - e^{-(n+1)\mu t}\right)}{\left(1 - e^{-\mu t}\right)}$$

$$= \frac{dN}{dE}\frac{\left(1 - e^{-n\mu t}\right)\left(1 + e^{-\mu t}\right)}{\left(1 - e^{-\mu t}\right)}$$

$$= \frac{dN}{dE}\frac{\left(1 - e^{-n\mu t}\right)\left(1 + 1 - \mu t + (\mu t)^2/2! - (\mu t)^3/3! \ldots\right)}{\left(1 - 1 + \mu t - (\mu t)^2/2! + (\mu t)^3/3! \ldots\right)}$$

$$= \frac{dN}{dE}\frac{\left(1 - e^{-n\mu t}\right)(2 - \mu t)}{\mu t} \qquad \text{for } \mu t \ll 1$$

$$= \underline{\underline{\frac{dN}{dE}\frac{2}{\mu t}\left(1 - e^{-n\mu t}\right)}} \qquad \text{for } \mu t \ll 1$$

ACKNOWLEDGEMENTS

The author would like to thank Professor G. D. Rochester (F.R.S.) for his interest and use of laboratory facilities; thanks are also due to Professor A. W. Wolfendale for useful comments.

He is indebted to his supervisor, Dr. J. M. Breare, for the helpful guidance and continual assistance he gave throughout the whole of the work. Members, both past and present, of the Nuclear Instrumentation Group are thanked for discussions and many hours of practical help, as also are the departmental technical staff, in particular Mr. J. Webster, Mr. H. Davidson and Mr. G. Whitfield. The International Research and Development Company of Newcastle-upon-Tyne, kindly provided chamber winding facilities.

The Science Research Council are thanked for the award of a maintenance grant, and for use of their High Energy Laboratories at Daresbury and Rutherford. Dr. J. E. Bateman of Rutherford was of great assistance in suggesting the pulse shape discrimination technique.

Lastly, but by no means least, Mrs. M. Garner is highly praised for a most careful and efficient transcription of the handwritten text.